

8-2014

Zinc Oxide Nanostructures for Flexible and Transparent Electronics

Do Yeob Kim

Follow this and additional works at: https://tigerprints.clemson.edu/all_dissertations

Recommended Citation

Kim, Do Yeob, "Zinc Oxide Nanostructures for Flexible and Transparent Electronics" (2014). *All Dissertations*. 1470.
https://tigerprints.clemson.edu/all_dissertations/1470

This Dissertation is brought to you for free and open access by the Dissertations at TigerPrints. It has been accepted for inclusion in All Dissertations by an authorized administrator of TigerPrints. For more information, please contact kokeefe@clemson.edu.

ZINC OXIDE NANOSTRUCTURES FOR FLEXIBLE
AND TRANSPARENT ELECTRONICS

A Dissertation
Presented to
the Graduate School of
Clemson University

In Partial Fulfillment
of the Requirements for the Degree
Doctor of Philosophy
Electrical Engineering

by
Do Yeob Kim
August 2014

Accepted by:
Dr. Sung-O Kim, Committee Chair
Dr. Eric Johnson
Dr. John Ballato
Dr. William Harrell

ABSTRACT

As a multifunctional material, ZnO possesses remarkable and unique properties and has attracted much research interest for use in a variety of applications. Especially, it has been regarded as a leading material for flexible and transparent electronics, which is a promising emerging technology in electronics. This dissertation studies doping behavior of Ga in ZnO for transparent electrode applications and presents new approaches to ZnO nanostructures for next-generation flexible and transparent electronics. These approaches include developing techniques that enable multiple stacked ZnO nanoflowers and thermal treatment processes at high temperature.

Transparent conductive oxides have been extensively studied for the use as a transparent electrode, which is one of the most fundamental and essential parts in transparent electronic devices. In this study, Ga-doped ZnO nanorods were grown on glass substrates, and the effects of Ga doping concentration on the physical properties of ZnO nanorods were investigated using various characterization tools.

ZnO nanoflower is a highly preferred nanostructure for solar cells, sensors, and photodetectors due to its high surface area to volume ratio. To-date, ZnO nanoflowers have mostly been synthesized in the form of nanopowders without a substrate, and ZnO nanoflowers grown on substrates have only been single-stacks. Atmospheric pressure plasma jet treatment was used to increase the surface area to volume ratio of ZnO nanoflowers. The plasma treatment induced a significant increase in the height and density of the ZnO nanoflowers/nanorods because the plasma effectively increased the

surface energy and roughness of the seed layers while barely affecting the crystal shape and phase of the ZnO nanoflowers/nanorods.

Flexible and transparent mica substrates were used for the growth of vertically well-aligned ZnO nanorods. The adoption of mica as a substrate material permitted high temperature annealing processes, which improved the structural and optical properties of ZnO nanorods with uniform surface coverage and excellent adhesion. A practical application for the synthesized ZnO nanorods is also presented in this dissertation. ZnO nanorod-based flexible and transparent dye-sensitized solar cells (DSSCs) and piezoelectric nanogenerators (NGs) were fabricated and the device performances were investigated. Although only two kinds of energy-harvesting devices (DSSCs and NGs) are presented as examples of applications in this dissertation, it is expected that this new approach will provide a breakthrough for overcoming the limited process temperature on plastic and cellulose nanopaper substrates because mica can be extensively used as a flexible and transparent substrate material for electronics, optoelectronics, energy/environmental, and biomedical applications where high temperature processes are required.

ACKNOWLEDGMENTS

I would like to express my deepest gratitude to Dr. Sung-O Kim. I am extremely fortunate to have such a great man as my advisor and mentor. The time, support, and guidance that he provided me throughout the years are immeasurable.

I would like to thank the members of my committee, Dr. Eric Johnson, Dr. John Ballato, and Dr. William Harrell, for their time and reviewing in this work.

I would like to thank those associated with the Center for Optical Materials Science and Engineering Technologies for their help and support. Special thanks go to those associated with Electron Microscopy Laboratory.

I wish to express my sincere thanks to my past and present group members, Dr. Jae Young Kim, Dr. Choon-Sang Park, Daniel Cutshall, and Travis Parsons, for contributing to the great atmosphere within this group through valuable assistance and lots of fun.

I am deeply indebted to my previous advisor for my M.S. degree at Inje University, Dr. Jae-Young Leem, for his ongoing support, advice, and encouragement through the years. I am also very grateful to the alumni and present members of Nano Physics and Devices Lab at Inje University.

Finally, I would like to thank my parents, as well as all of my family and friends for their love, support, and encouragement they have done for me.

TABLE OF CONTENTS

	Page
TITLE PAGE	i
ABSTRACT.....	ii
ACKNOWLEDGMENTS	iv
LIST OF TABLES	vii
LIST OF FIGURES	viii
 CHAPTER	
I. INTRODUCTION	1
Motivation.....	1
Research Objectives.....	2
Dissertation Overview	3
II. FUNDAMENTALS OF ZINC OXIDE	7
Physical Properties.....	7
Growth Techniques.....	12
Applications	15
III. GALLIUM-DOPED ZINC OXIDE NANORODS GROWN ON GLASS	41
Introduction.....	41
Experimental Details.....	43
Effects of Gallium Doping Concentration	44
Conclusions.....	64
IV. MULTIPLE STACKED ZINC OXIDE NANOFLOWERS GROWN ON PLASTIC	72
Introduction.....	72
Experimental Details.....	74
Plasma-Treated ZnO Seed Layers	78
Multiple Stacked ZnO Nanoflowers/Nanorods	81

Table of Contents (Continued)

	Page
Conclusions.....	91
V. HIGH TEMPERATURE PROCESSED ZINC OXIDE NANORODS GROWN ON MICA	97
Introduction.....	97
Experimental Details.....	100
Growth Parameters.....	103
Effects of Thermal Annealing Processes	115
ZnO Nanorod-Based Dye-Sensitized Solar Cells	125
ZnO Nanorod-Based Piezoelectric Nanogenerators	127
Conclusions.....	129
VI. CONCLUSIONS.....	136
Research Summary	136
Future Work	137

LIST OF TABLES

Table	Page
2.1 Properties of bulk wurtzite ZnO	11
3.1 Calculated values of texture coefficients of the ZnO nanorods with different Ga doping concentrations	50
4.1 Contact angle and surface energy of the ZnO seed layers	81
5.1 Comparison of substrate materials for flexible and/or transparent electronics	99
5.2 Comparison of transmittance and sheet resistance of the ITO/PET and ITO/mica substrates.....	122
5.3 Comparison of the thermal treatment processes for PET and mica substrates	124

LIST OF FIGURES

Figure	Page
2.1 Schematic diagrams of piezoelectric effect in ZnO crystal: (a) tetrahedral coordination between zinc and oxygen and (b) distortion of the tetrahedral unit under compressive force	10
2.2 Schematic diagram of typical nanorod-based DSSCs	17
2.3 Schematic diagram of operation principle of DSSCs. S: dye sensitizer, S^+ : oxidized dye sensitizer, S^* : electronically excited dye sensitizer, O/R: redox couple (I^-/I_3^-), E_v : valence band of semiconductor, and E_c : conduction band of semiconductor.....	19
2.4 Typical photocurrent-voltage curve of DSSCs	20
2.5 Physical principle of nanorod-based piezoelectric NGs: (a) schematic definition of a nanorod, (b) longitudinal strain distribution in the nanorod, (c) corresponding longitudinal piezoelectric-induced electric field, and (d) potential distribution in the nanorod as a result of the piezoelectric effect	23
2.6 Schematic diagram of typical nanorod-based NGs.....	24
3.1 SEM images of the ZnO nanorods with different Ga doping concentrations: (a and b) as-grown, (c and d) 0.5 at.%, (e and f) 1.0 at.%, and (g and h) 3.0 at.%	46
3.2 Contact angle measurement of the ZnO nanorods with different Ga doping concentrations: (a) as-grown, (b) 0.5 at.%, (c) 1.0 at.%, and (d) 3.0 at.%	47
3.3 XRD patterns of the ZnO nanorods with different Ga doping concentrations	49

List of Figures (Continued)

Figure	Page
3.4 Texture coefficient of the ZnO nanorods with different Ga doping concentrations	50
3.5 Peak position of the ZnO(002) diffraction with different Ga doping concentrations.....	53
3.6 Lattice constants of the ZnO nanorods with different Ga doping concentrations: (a) <i>a</i> -axis lattice constant and (b) <i>c</i> -axis lattice constant	54
3.7 Biaxial stress and bond length of the ZnO nanorods with different Ga doping concentrations.....	55
3.8 Optical transmittance spectra of the ZnO nanorods with different Ga doping concentrations. Inset shows optical reflectance for the same ZnO nanorods	59
3.9 Absorption coefficient of the ZnO nanorods with different Ga doping concentrations.....	60
3.10 $(\alpha h\nu)^2$ plotted as a function of photon energy for the ZnO nanorods with different Ga doping concentrations	61
3.11 Optical band gap energy of the ZnO nanorods with different Ga doping concentrations.....	62
3.12 Resistivity of the ZnO nanorods with different Ga doping concentrations	63
4.1 (a) Schematic diagram of the APPJ system. (b) Photograph of seven well-collimated plasma plumes between the plasma array and the PEN substrate.....	76
4.2 Optical emission spectrum of the APPJ array, which was monitored using a fiber-optic spectrometer	79

List of Figures (Continued)

Figure	Page
4.3	Contact angle measurement of the (a) as-grown ZnO seed layers and the (b) plasma-treated ZnO seed layers. Insets show a photograph of a water droplet on each seed layer 80
4.4	AFM images of the (a) as-grown ZnO seed layers with RMS roughness of 2.783 nm and the (b) plasma-treated ZnO seed layers with RMS roughness of 3.063 nm. Top-view FE-SEM images of the (c) as-grown ZnO seed layers and the (d) plasma-treated ZnO seed layers 82
4.5	Top-view FE-SEM images of the ZnO nanoflower/nanorod structures grown on the (a) as-grown ZnO seed layers and the (b) plasma-treated ZnO seed layers. Insets show high-magnified images of the nanorods on the bottom layer (red rectangles) and nanoflowers on the top layer (blue rectangles) 83
4.6	Cross-sectional FE-SEM images of ZnO nanoflowers/nanorods grown on the (a and c) as-grown ZnO seed layers and the (b and d) plasma-treated ZnO seed layers. Histograms of the (e) length and (f) diameter distribution of the nanorods 85
4.7	XRD patterns of the ZnO nanoflower/nanorod structures grown on the (a) as-grown ZnO seed layers and the (b) plasma-treated ZnO seed layers. The peaks denoted with an asterisk are attributed to the PEN substrates 87
4.8	Low-magnification TEM images of the ZnO nanoflower/nanorod structures grown on the (a) as-grown ZnO seed layers and the (b) plasma-treated ZnO seed layers. HRTEM images of the ZnO nanoflower/nanorod structures grown on the (c) as-grown ZnO seed layers and the (d) plasma-treated ZnO seed layers with their corresponding FFT patterns (inset) 88
4.9	Raman scattering spectra of the (a) bare PEN substrate and the ZnO nanoflowers/nanorods grown on the (b) as-grown ZnO seed layers and the (c) plasma-treated ZnO seed layers 90

List of Figures (Continued)

Figure	Page
5.1 Schematic diagrams of the fabricated ZnO nanorod-based devices in this work: (a) DSSCs and (b) piezoelectric NGs	102
5.2 FE-SEM images of the ZnO nanorods grown at different PEI concentrations: (a and b) 0 M, (c and d) 0.005 M, (e and f) 0.0075 M, and (g and h) 0.01 M. The growth temperature and time are 90 °C and 9 h, respectively	105
5.3 FE-SEM image of the ZnO nanorods grown at 0.015 M PEI concentration. The growth temperature and time are 90 °C and 9 h, respectively	106
5.4 FE-SEM images of the ZnO nanorods grown at different temperatures: (a and b) 75 °C, (c and d) 85 °C, and (e and f) 95 °C. The growth time and PEI concentration are 9 h and 0.005 M, respectively	107
5.5 FE-SEM images of the ZnO nanorods grown at different ammonium hydroxide concentrations: (a) 0.1 M, (b) 0.15 M, (c) 0.2 M, and (d) 0.25 M. The growth temperature and concentration of PEI are 85 °C and 0.005 M, respectively	110
5.6 Cross-sectional FE-SEM images of the ZnO nanorods grown at different ammonium hydroxide concentrations: (a) 0.1 M, (b) 0.15 M, (c) 0.2 M, and (d) 0.25 M. The growth temperature and PEI concentration are 85 °C and 0.005 M, respectively. (e) Average length of the nanorods as a function of ammonium hydroxide concentration	111
5.7 FE-SEM images of the ZnO nanorods grown in the solution containing 0.01 M PEI and 0.4 M ammonium hydroxide at 85 °C: (a) cross-sectional view and (b) tilted view. (c) Low-magnification TEM image of the ZnO nanorod. (d) HRTEM image of the ZnO nanorod with its corresponding FFT pattern (inset)	113

List of Figures (Continued)

Figure	Page
5.8	Cross-sectional FE-SEM images of the ZnO nanorods grown with different growth times: (a) 3 h, (b) 6 h, (c) 9 h, (d) 12 h, (e) 15 h, (f) 18 h, (g) 21 h, and (h) 24 h 114
5.9	XRD patterns of the as-grown and annealed ZnO nanorods. The peaks denoted with an asterisk are attributed to the mica 118
5.10	Raman scattering spectra of the as-grown and annealed ZnO nanorods..... 119
5.11	Transmittance spectra and top view photographs of PET (black), mica (orange), ITO/PET (red), ITO/mica (green), and annealed ITO/mica (blue) 120
5.12	Sheet resistance of the ITO/PET (red), ITO/mica (green), and annealed ITO/mica (blue) 121
5.13	Photographs of ZnO nanorods grown on PET and mica substrates: (e) before a bending and (f) after a bending of 1000 cycles with a bending radius of 5 mm 123
5.14	XRD patterns of the ZnO nanorods grown on PET and mica substrates. The peaks denoted with an asterisk are attributed to the mica and PET substrates. The signals from the ZnO nanorods grown on PET were multiplied by 10 times of their original values 124
5.15	Photocurrent density-voltage characteristics of DSSCs with photoanodes made from ZnO nanorods grown on mica under AM 1.5 illumination: (a) sample A (9 h-growth) vs. sample B (18 h-growth), (b) sample A (9 h-growth) vs. sample C (9 h-growth and post-growth annealing) and (c) sample A (9 h-growth) vs. sample D (18 h-growth and post-growth annealing)..... 126
5.16	Measured output performance of the NG based on as-grown ZnO nanorods (black) and post-growth annealed ZnO nanorods (red): (a) output voltage and (b) output current density 128

CHAPTER ONE

INTRODUCTION

Motivation

Substantial advances in nanometer-scale science and technology for the past few decades have been achieved, which has paved the path for new ideas and directions of future electronics. Smartphones and tablet personal computers are notable examples of state-of-the-art technologies in electronics, and the most recent research interests have been focused on realizing fully stretchable, flexible, wearable, and transparent electronic devices, which definitely would widen their potential and practical applications in a variety of industries. Together with the research interests, the market for flexible and transparent electronics would rapidly grow. The demand for the flexible and transparent electronic products at present may not be noticed but in the near future there would be huge demand and considerable preference will be given to the flexible and transparent products on the market. For example, a recent report on the transparent electronics market forecasts that it will increase at a compound annual growth rate of 52.91% over the period 2013–2018 [1]. Despite the considerable research interests and increasing market demand in flexible and transparent electronic devices, there still remain some challenges that must be overcome in order to improve the overall device performances [2–7].

ZnO is a highly multifunctional and promising material for next-generation flexible and transparent applications due to its useful and unique properties, including piezoelectricity, UV luminescence (transparency to visible light), large exciton binding

energy, high electron mobility, and chemical/thermal stability [8–10]. ZnO can be synthesized readily at low temperature with various morphologies of nanostructures, which is a crucial advantage over other semiconductor materials for flexible and transparent nanometer-scale electronic devices. Its biocompatibility also makes it a leading material for biological applications, such as wearable health monitoring and drug delivery devices. Therefore, ZnO has been extensively explored, serving for various purposes, such as active layers, buffer layers, and transparent conductive oxides in device applications [11–15].

Research Objectives

The research on ZnO has a long history and understanding the properties of ZnO bulk material is well established, but there has been a considerable renewed interest in ZnO nanostructures in nanoscience and nanotechnology related fields because these nanostructures exhibit several distinctive properties in accordance with their nanometer-scale dimensions as well as share the common properties of ZnO bulk.

The general aim of this dissertation is to investigate and utilize the unique properties of ZnO nanostructures and apply them to flexible and transparent applications. Specifically, the key issues to be investigated include: (i) controlling the physical properties of ZnO (Chapter III), (ii) synthesizing ZnO nanostructures with a high surface area to volume ratio (Chapter IV), (iii) developing a technique for high-temperature ZnO processing for flexible and transparent electronic devices (Chapter V), and (iv) fabricating and characterizing flexible and transparent ZnO-based dye-sensitized solar cells and piezoelectric nanogenerators (Chapter V).

Dissertation Overview

Following the general introduction above, Chapter II presents fundamentals of ZnO with regard to this dissertation, including its physical properties, growth techniques, and applications. Some contents related to this study are discussed in more detail. Chapter III focuses on the doping behavior of Ga in ZnO nanorods for transparent electrodes. Effects of Ga doping concentration on structural, optical, and electrical properties of ZnO nanorods are discussed. Chapter IV presents low-temperature growth of multiple stacked ZnO nanoflowers on plastic substrates. An atmospheric pressure plasma jet system is introduced for the surface modification of ZnO seed layers. Advantages and roles of the plasma treatment for the synthesis of multiple stacked ZnO nanoflowers are discussed. Chapter V presents a new approach that enables high temperature thermal treatment over the entire processes from synthesis of ZnO nanostructures to fabrication of flexible and transparent ZnO-based electronic devices. Finally, Chapter VI summarizes the entire dissertation.

References

- [1] TechNavio, Global transparent electronics market 2014–2018, May 2014, <www.technavio.com>.
- [2] X. Liu, Y.-Z. Long, L. Liao, X. Duan, and Z. Fan, Large-scale integration of semiconductor nanowires for high-performance flexible electronics, *ACS Nano*, **6**, 1888–1900, 2012.
- [3] A.J. Baca, J.-H. Ahn, Y. Sun, M.A. Meitl, E. Menard, H.-S. Kim, W.M. Choi, D.-H. Kim, Y. Huang, and J.A. Rogers, Semiconductor wires and ribbons for high-performance flexible electronics, *Angew. Chem. Int. Ed.*, **47**, 5524–5542, 2008.
- [4] Y. Sun and J.A. Rogers, Inorganic semiconductors for flexible electronics, *Adv. Mater.*, **19**, 1897–1916, 2007.
- [5] H. Frenzel, A. Lajn, and M. Grundmann, One decade of fully transparent oxide thin-film transistors: Fabrication, performance and stability, *Phys. Status Solidi Rapid Res. Lett.*, **7**, 605–615, 2013.
- [6] H. Zhu, Z. Fang, C. Preston, Y. Li, and L. Hu, Transparent paper: Fabrications, properties, and device applications, *Energy Environ. Sci.*, **7**, 269–287, 2014.
- [7] A. Stadler, Transparent conducting oxides—an up-to-date overview, *Materials*, **5**, 661–683, 2012.

- [8] U. Ozgur, Y.I. Alivov, C. Liu, A. Teke, M.A. Reshchikov, S. Dogan, V. Avrutin, S.-J. Cho, and H. Morkoc, A comprehensive review of ZnO materials and devices, *J. Appl. Phys.*, **98**, 041301, 2005.
- [9] S. Baruah and J. Dutta, Hydrothermal growth of ZnO nanostructures, *Sci. Technol. Adv. Mater.*, **10**, 013001, 2009.
- [10] D.P. Norton, Y.W. Heo, M.P. Ivill, K. Ip, S.J. Pearton, M.F. Chisholm, and T. Steiner, ZnO: Growth, doping & processing, *Mater. Today*, **7**, 34–40, 2004.
- [11] S.H. Lee, J.S. Lee, W.B. Ko, S.N. Cha, J.I. Sohn, J.M. Kim, J.G. Park, Y. Park, and J.P. Hong, Solution-processed Ag-doped ZnO nanowires grown on flexible polyester for nanogenerator applications, *Nanoscale*, **5**, 9609–9614, 2013.
- [12] S. Niu, Y. Hu, X. Wen, Y. Zhou, F. Zhang, L. Lin, S. Wang, and Z.L. Wang, Enhanced performance of flexible ZnO nanowire based room-temperature oxygen sensors by piezotronic effect, *Adv. Mater.*, **25**, 3701–3706, 2013.
- [13] M. Thambidurai, J.Y. Kim, J. Song, Y. Ko, H.-J. Song, C.-M. Kang, N. Muthukumarasamy, D. Velauthapillai, and C. Lee, High performance inverted organic solar cells with solution processed Ga-doped ZnO as an interfacial electron transport layer, *J. Mater. Chem. C*, **1**, 8161–8166, 2013.
- [14] R.-H. Horng, K.-C. Shen, C.-Y. Yin, C.-Y. Huang, and D.-S. Wu, High performance of Ga-doped ZnO transparent conductive layers using MOCVD for GaN LED applications, *Opt. Express*, **21**, 14452–14457, 2013.

- [15] F. Jiang, S. Ikeda, T. Harada, A. Ide, A. Mochihara, K. Yoshino, and M. Matsumura, Fabrication of an efficient electrodeposited $\text{Cu}_2\text{ZnSnS}_4$ -based solar cells with more than 6% conversion efficiency using a sprayed Ga-doped ZnO window layer, *RSC Adv.*, **4**, 24351–24355, 2014.

CHAPTER TWO

FUNDAMENTALS OF ZINC OXIDE

Physical Properties

ZnO is known to exist in three different crystalline forms depending on the crystallization conditions: cubic zinc blende, cubic rock-salt (or Rochelle salt), and hexagonal wurtzite. The ZnO with zinc blende and rock-salt crystal structures can be crystallized under particular conditions or special processing [1–4]. Under ambient conditions, ZnO crystallizes preferentially in a thermodynamically stable hexagonal wurtzite crystal structure where each oxygen anion is surrounded by four zinc cations at the corners of a tetrahedron. In other words, the ZnO crystal structure is composed of alternating planes of Zn^{2+} and O^{2-} ions stacking along the c -axis direction. The lattice constants of bulk ZnO along the a -axis and c -axis are 3.2495 and 5.2069 Å, respectively. ZnO shows a highly ionic character due to the large difference in electronegativity between Zn and O atoms. Non-central symmetric tetrahedral coordination in ZnO results in piezoelectric properties and crystallographic polarity. Another appreciable characteristic of the ZnO crystal structure is the presence of polar surfaces, with the basal plane as the most common polar surface. The oppositely charged zinc-terminated (0001) Zn-face and oxygen-terminated (000 $\bar{1}$) O-face produce spontaneous polarization along the c -axis direction as well as a divergence in surface energy [5]. The polar surfaces of ZnO are highly metastable in nature, and each polar surface possesses different physical and chemical properties.


ZnO is a group II-VI oxide semiconductor with direct and wide band gap energy of 3.37 eV at room temperature. Direct band gap semiconductors have intrinsically higher luminescence efficiency than indirect band gap semiconductors, and higher band gap ensures that devices operate more stably at higher temperature. The exciton emission in semiconductors is a more efficient radiative process because the oscillator strength of excitons is typically very large compared to direct electron-hole transitions [6]. ZnO has large free-exciton binding energy of 60 meV, which is much higher than the thermal energy at room temperature (26 meV), ensuring a persistent and efficient exciton emission under low excitation energy [7–9]. The band gap energy of ZnO can be further tuned by alloying ZnO with CdO ($E_g = 2.3$ eV) and/or MgO ($E_g = 7.8$ eV). $\text{Cd}_x\text{Zn}_{1-x}\text{O}$ alloy leads to a reduction in the band gap to ~ 3.0 eV, and $\text{Mg}_x\text{Zn}_{1-x}\text{O}$ can increase the band gap up to ~ 4.0 eV [10–15].

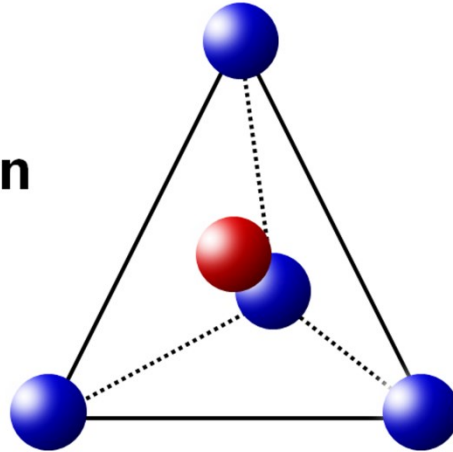
In photoluminescence spectrum at room temperature, ZnO exhibits the two main emissions, the sharp and strong ultraviolet emission centered at around 386 nm, and the very weak broad band emission which includes the blue band (440–480 nm) and green band (510–580 nm) [16–19]. The ultraviolet emission arises from the near band edge emission of the wide band gap ZnO. The weak broad band is due to a number of intrinsic and extrinsic radiative defect levels. It is known that the visible deep center emission depends strongly on the growth conditions and the growth method used [20–23]. The optical quality of ZnO can be determined from the relative intensity between the ultraviolet and broad band emissions. A large ratio of the intensity of the ultraviolet emission to the intensity of the broad band emission indicates a lower concentration of

the deep level defects, such as oxygen vacancies, zinc vacancies, oxygen interstitials, and zinc interstitials.



The piezoelectric effect is also one of the unique properties of ZnO. Piezoelectricity arises from atomic scale polarization of the non-centrosymmetric wurtzite crystal structure of ZnO. The ZnO unit cell has a Zn^{2+} cation surrounded tetrahedrally by O^{2-} anions (Figure 2.1a). There are no dipoles under non-stress conditions because the positive and negative centers of mass correspond with each other. However, when the crystal is subjected to a mechanical force, the tetrahedron experiences a distortion and the positive center of mass no longer coincides with the negative center of mass, leading to an electric dipole (Figure 2.1b). In single crystal ZnO, electric dipoles in all the tetrahedrons are lined up in the same orientation, resulting in a macroscopic dipole. The common physical properties of the bulk ZnO materials are summarized in Table 2.1.

(a)

 Zinc
 Oxygen



(b)

 Zinc
 Oxygen

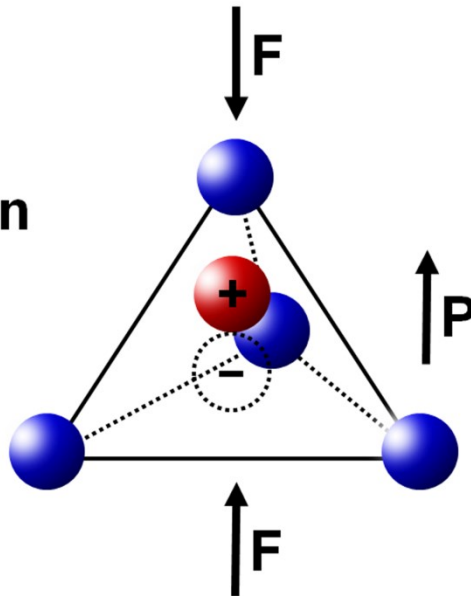


Figure 2.1: Schematic diagrams of piezoelectric effect in ZnO crystal: (a) tetrahedral coordination between zinc and oxygen and (b) distortion of the tetrahedral unit under compressive force.

Table. 2.1: Properties of bulk wurtzite ZnO.

Property	Value
Density	5.606 g/cm ³
Dielectric constant	8.66
Refractive index	2.008
Lattice parameters	a_0 : 3.2495 Å c_0 : 5.2069 Å u : 0.348 c/a : 1.593–1.6035
Thermal expansion coefficient	a_0 : $6.51 \times 10^{-6}/\text{K}$ c_0 : $3.02 \times 10^{-6}/\text{K}$
Direct band gap energy	3.37 eV
Electron mobility (300 K)	100–200 cm ² /V·s
Hole mobility (300 K)	5–50 cm ² /V·s
Electron effective mass	$0.24m_0$
Hole effective mass	$0.59m_0$
Exciton binding energy	60 meV

Growth Techniques

ZnO possesses the richest family of nanostructures among all known materials due to its polar surfaces and a tendency for different fast growth directions. Structurally, ZnO has three types and a total of 13 fast growth directions: $\langle 2\bar{1}\bar{1}0 \rangle$ ($\pm[2\bar{1}\bar{1}0]$, $\pm[\bar{1}2\bar{1}0]$, $\pm[\bar{1}\bar{1}20]$); $\langle 01\bar{1}0 \rangle$ ($\pm[01\bar{1}0]$, $\pm[1\bar{1}00]$, $\pm[10\bar{1}0]$); and $\pm[0001]$. In thermodynamic equilibrium, the facet with low surface energy tends to form a larger area compared to that with high surface energy. In the ZnO growth, the $\{2\bar{1}\bar{1}0\}$ and $\{01\bar{1}0\}$ facets comprise large areas because of the lower energy, and the fastest growth occurs along the *c*-axis [5,24–26]. Such anisotropic growth results in a wide range of structural morphologies of ZnO such as nanorods, nanotubes, nanobelts, nanosprings, nanorings, nanowalls, nanocombs, nanotetrapods, nanoflowers, nanohelices, and branched hierarchical structures [27–44]. Most of the uniquely structured ZnO nanomaterials were initially synthesized using high-temperature processes from the vapor phase in a closed chamber with a gaseous environment [45–53]. Another route for the growth of ZnO nanostructures is the liquid phase method using an aqueous and/or organic solution. The liquid phase approach enables low-temperature and cost-effective processes and thus allows the use of organic substrates for future flexible and portable electronics. This explains why the liquid phase method has been demonstrated as a powerful and versatile growth technique. In this study, ZnO nanostructures were synthesized using liquid phase methods, such as the sol-gel spin-coating and hydrothermal methods.

Sol-Gel Method

ZnO seeds in the form of thin films or nanoparticles are generally coated on arbitrary substrates before the growth of ZnO nanostructures, which promotes high-density nucleation process through reduction of thermodynamic barrier [54–56]. In this study, ZnO seed layers were prepared using the sol-gel spin-coating method.

In sol-gel methods, ZnO seed layers are formed through pre-heat and post-heat treatments. The pre-heat treatment is conducted after each spin-coating process. It governs the orientation of the crystallites during solvent evaporation and removal of the organic compounds. The temperature of pre-heat treatment varies from case to case, but a clear rule can be deduced from the used solvent and additives. It should be higher than the boiling point of the solvent and the additives, and near the crystallization temperature of ZnO. After several times of spin-coating and pre-heat treatment of the seed layers, post-heat treatment is necessary for promoting crystallinity of the seed layers. The resultant properties of the seed layers largely depend on various parameters such as precursor concentration, additives, aging time, temperature of heat treatment, and thickness [57–62].

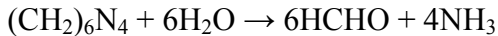
Hydrothermal Method

Since both homogeneous and heterogeneous nucleation can occur simultaneously in solution during hydrothermal reaction, ZnO is also obtained in the form of white precipitates, which are undesirable by-products in the aspect of ZnO nanostructures formed on seed layers. However, heterogeneous nucleation is more dominant because it generally has a lower activation energy barrier compared with homogeneous nucleation.

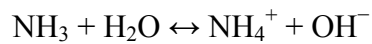
In addition, the interfacial energy between the crystal and substrate is lower than the energy between the crystal and solution [63]. Therefore, growth of ZnO nanostructures on the existing seed layers is more favorable than the formation of precipitates resulted from homogeneous nucleation.

Zinc nitrate $[\text{Zn}(\text{NO}_3)_2]$ and hexamethylenetetramine [HMTA, $(\text{CH}_2)_6\text{N}_4$] are the most commonly used reagents in the hydrothermal method. Zn^{2+} ions and O^{2-} ions are originated from $\text{Zn}(\text{NO}_3)_2$ and H_2O molecules in solution, respectively. HMTA is a nonionic tertiary amine that hydrolyzes under acidic conditions to yield ammonia and formaldehyde [64]. Although its detailed function is still not fully understood, it is generally accepted that HMTA acts as a pH buffer and a slow, steady source of hydroxide ions. HMTA also acts as a bidentate Lewis base that coordinates and bridges two Zn^{2+} ions [29,65,66]. Therefore, HMTA attached onto the nonpolar side facets also contributes to the anisotropic growth along the *c*-axis together with the inherent fast growth in the [0001] direction. The chemical reactions of the hydrothermal method using $\text{Zn}(\text{NO}_3)_2$ and HMTA can be summarized as follows [67,68]:

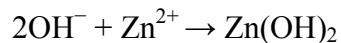
Decomposition reaction:



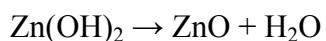
Hydroxyl supply reaction:



Supersaturation reaction:



ZnO growth reaction:



A degree of supersaturation is an important parameter for the growth of ZnO nanostructures. It is generally believed that the high degree of supersaturation favors homogeneous nucleation while the low degree of supersaturation favors heterogeneous nucleation. If a large amount of OH^- is produced in a short period of time because of the quick hydrolysis of HMTA, the Zn^{2+} ions in solution would precipitate out quickly due to the high pH environment. This quick hydrolysis of HMTA would lead to fast consumption of the nutrient and eventually contribute less to the growth of ZnO nanostructures [65,69–72]. Therefore, the hydrolysis rate of HMTA should be deliberately controlled to ensure the low degree of supersaturation environment during the whole growth process. The hydrothermal reaction can be controlled by adjusting the reaction parameters such as seed layer, reagents, additives, precursor concentration, solution pH, growth time, growth temperature, and heat source [33,65,73–90].

Applications

ZnO is an attractive candidate for a wide range of applications, such as electronic devices, optoelectronic devices, piezoelectric devices, energy harvesting devices, and sensing devices, due to their unique and remarkable properties as mentioned above [91–111]. Presented here are some fundamentals of dye-sensitized solar cells (DSSCs) and piezoelectric nanogenerators (NGs) for the help of understanding characterization data of ZnO nanorod-based DSSCs and NGs provided in Chapter V.

Dye-Sensitized Solar Cells

The typical structure of DSSCs is shown in Figure 2.2. DSSCs consist of two transparent conducting electrodes in a sandwich configuration. A few micrometer-thick layer of a wide band gap semiconductor (ZnO nanorods in this study) is deposited on one of the electrodes and it acts as a photoanode in DSSCs. The photoanode should have a high surface area to volume ratio for high energy conversion efficiency. Dye molecules are attached onto the surface of the photoanode and an electrolyte is filled between the two electrodes. On the other electrode, a thin layer of platinum is generally deposited for high catalytic activity.

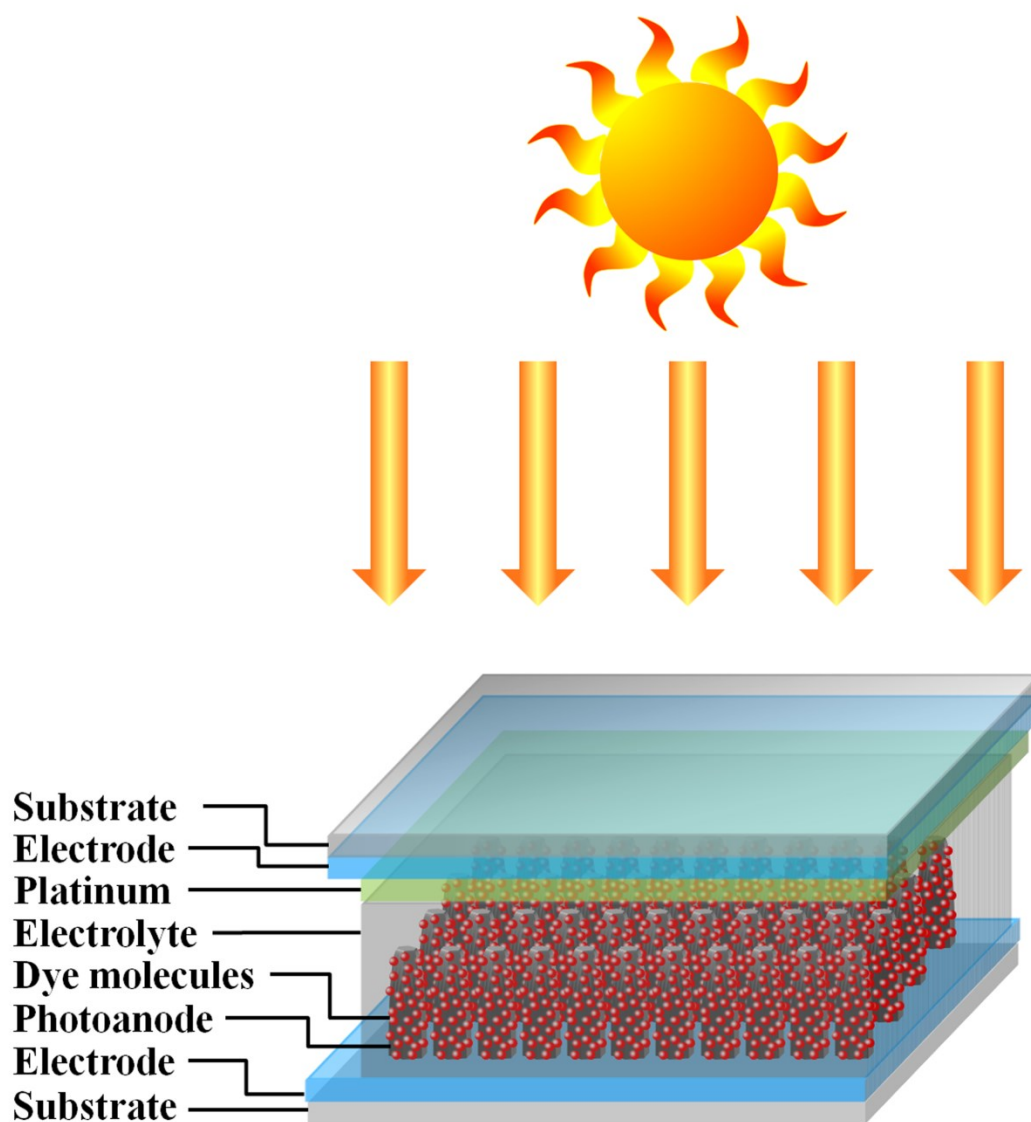
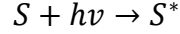


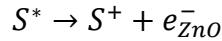
Figure 2.2: Schematic diagram of typical nanorod-based DSSCs.

The light-driven electrochemical process in DSSCs is shown in Figure 2.3. The operating cycle can be expressed in chemical reaction terminology as [112]:

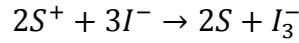
Excitation process:



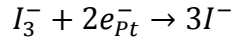
Injection process:



Regeneration of dye:



Reduction of iodide:



The light-to-electricity conversion in DSSCs is based on the injection of photoexcited electrons from the lowest unoccupied molecular orbital (LUMO) state of the dye to the conduction band of the semiconductor. Upon light absorption, electrons in the highest occupied molecular orbital (HOMO) state of the dye are electronically excited to the LUMO (S^*). The electrons excited to the LUMO levels are injected into the conduction band of the semiconductor and transported through the semiconductor by diffusion before reaching the photoanode of the cell. The oxidized dye molecule (S^+) is subsequently regenerated back to its original state by accepting an electron from the iodide in an electrolyte. The iodide is restored, in turn, by the reduction of triiodide at the counter electrode. The voltage produced from the cell is given by the difference between the chemical potential of the semiconductor (Fermi level) and the redox potential of the mediator I^-/I_3^- .

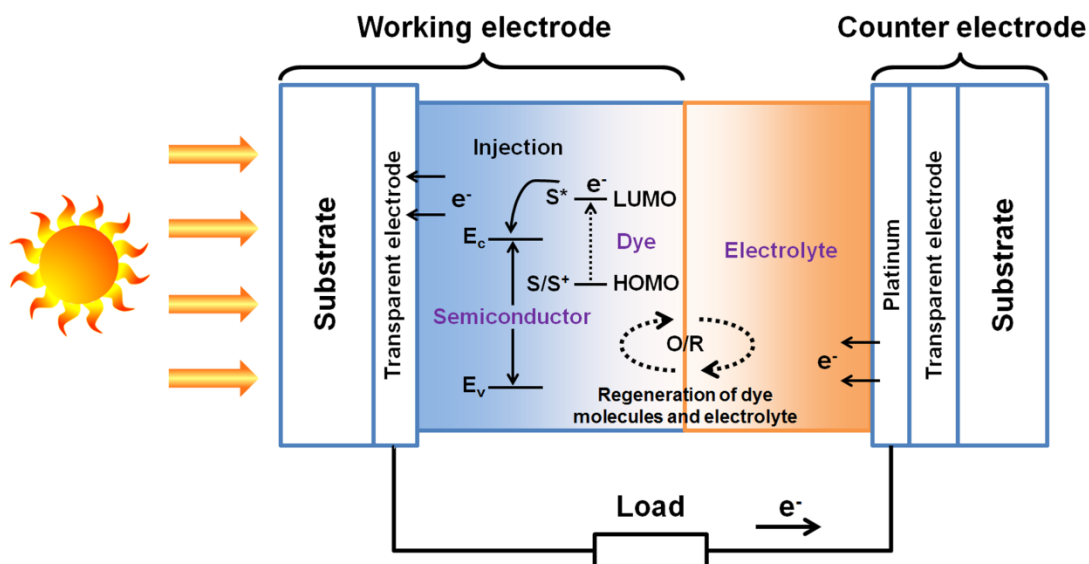


Figure 2.3: Schematic diagram of operation principle of DSSCs. S: dye sensitizer, S^+ : oxidized dye sensitizer, S^* : electronically excited dye sensitizer, O/R: redox couple (I^-/I_3^-), E_v : valence band of semiconductor, and E_c : conduction band of semiconductor.

Figure 2.4 shows a qualitative photocurrent-voltage curve of typical DSSCs. As the resistive load on an illuminated cell increases continuously from zero (a short circuit) to a very high value (an open circuit), the power delivered to the load first increases, reaches a maximum (P_{max}), and then decreases to zero. Some important photovoltaic parameters can be obtained from the photocurrent-voltage curve: short circuit current (I_{sc}), open circuit voltage (V_{oc}), energy conversion efficiency (η), and fill factor (FF). The short circuit current is the current value when a voltage is zero and the open circuit voltage is the voltage value when a current is zero in the obtained I - V curve. The energy conversion efficiency is defined as:

$$\eta = \frac{P_{max}}{P_{light}} = \frac{FF \times V_{oc} \times I_{sc}}{P_{light}}$$

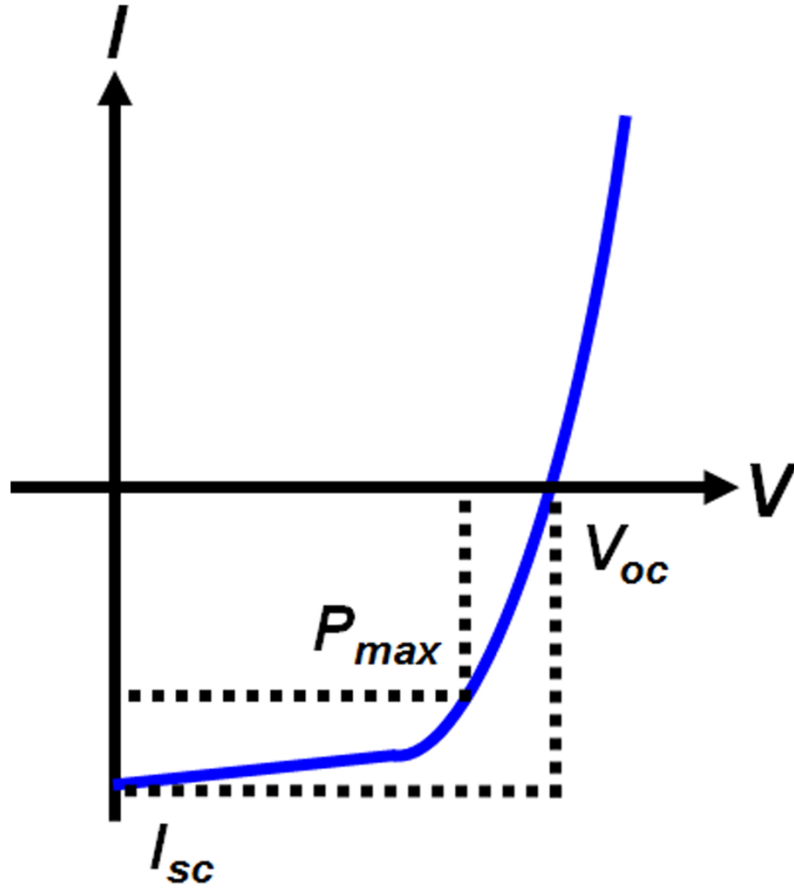


Figure 2.4: Typical photocurrent-voltage curve of DSSCs.

The fill factor can be obtained from above equation and is expressed as:

$$FF = \frac{\eta \times P_{light}}{V_{oc} \times I_{sc}} = \frac{P_{max}}{V_{oc} \times I_{sc}}$$

The fill factor compares the actual maximum electric power delivered by a cell (the area of the smaller rectangle in Figure 2.4) with the hypothetical maximum power (the area of the larger rectangle in Figure 2.4) and it is the ratio of the area of smaller rectangle to the area of larger rectangle. The fill factor is a measure of how steeply the current rises in DSSCs [113,114].

Piezoelectric Nanogenerators

The piezoelectric properties of ZnO resulting from the non-centrosymmetry of the wurzite crystal structure can be used for wireless and mobile energy harvesting devices that convert various forms of energy into electricity. The source of energy includes mechanical energy (air flow, body movement, muscle stretching, and heart beating), vibration energy (acoustic/ultrasonic wave), and hydraulic energy (body fluid and blood flow).

The idea of piezoelectric nanogenerators (NGs) was first presented by Wang's group [115]. They synthesized ZnO nanorods on conductive solid substrates, and the measurements were performed by an atomic force microscopy (AFM) using a platinum-coated tip. The working principle is explained by the coupling between the piezoelectric and semiconductor properties of the ZnO nanorods. When the AFM tip scans over the top of the nanorod, the nanorod is deformed (Figure 2.5a). This creates a strain field (ε_z), with the outer surface being tensile (positive strain) and inner surface compressive (negative strain) (Figure 2.5b). A piezoelectric field (E_z) along the nanorod (z direction) is then created inside the nanorod by the piezoelectric effect, $E_z = \varepsilon_z/d$, where d is the piezoelectric constant along the nanorod direction [116]. The piezoelectric field is closely parallel to the nanorod at the outer surface and anti-parallel to the z -axis at the inner surface (Figure 2.5c). As a result, across the width of the nanorod at the top end, the piezoelectric potential makes the stretched side positive (V_S^+) and the compressed side negative (V_S^-) (Figure 2.5d). The relative displacement of the Zn^{2+} cations with respect to the O^{2-} anions creates this potential. These ionic charges cannot freely move or

recombine without releasing the strain. The potential difference is kept as long as the deformation is in place, and no foreign free charges are injected.

The structure of typical nanorod-based NGs is shown in Figure 2.6. Vertically aligned ZnO nanorods are sandwiched between two layers of electrodes. Solidified poly(methyl methacrylate) (PMMA) encapsulates the nanorods and provides an infinitely high potential barrier, which prevents electrons from transporting through the ZnO/electrode interface. Due to the infiltration of PMMA into the gap between the nanorods, when the NGs are subject to a compressive stress, the stress can be transmitted through the PMMA to all nanorods.

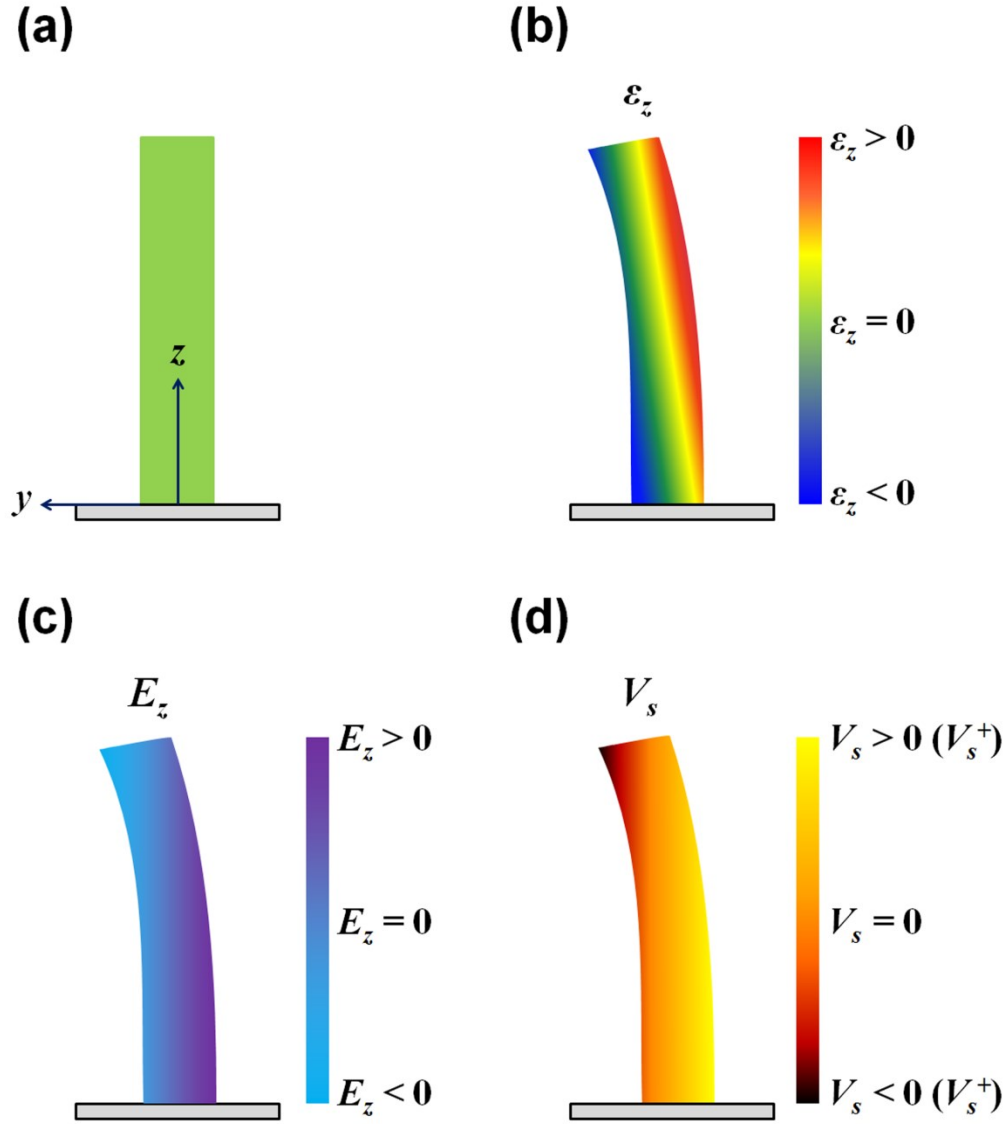


Figure 2.5: Physical principle of nanorod-based piezoelectric NGs: (a) schematic definition of a nanorod, (b) longitudinal strain distribution in the nanorod, (c) corresponding longitudinal piezoelectric-induced electric field, and (d) potential distribution in the nanorod as a result of the piezoelectric effect.

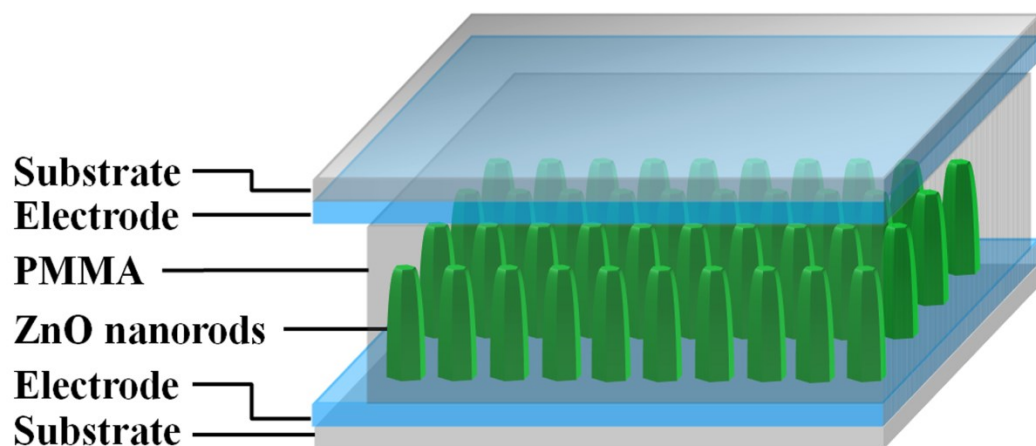


Figure 2.6: Schematic diagram of typical nanorod-based NGs.

References

- [1] A.B.M.A. Ashrafi, A. Ueta, A. Avramescu, H. Kumano, I. Suemune, Y.-W. Ok, and T.-Y. Seong, Growth and characterization of hypothetical zinc-blende ZnO films on GaAs(001) substrates with ZnS buffer layers, *Appl. Phys. Lett.*, **76**, 550–552, 2000.
- [2] S.-K. Kim, S.-Y. Jeong, and C.-R. Cho, Structural reconstruction of hexagonal to cubic ZnO films on Pt/Ti/SiO₂/Si substrate by annealing, *Appl. Phys. Lett.*, **82**, 562–564, 2003.
- [3] T. Tanigaki, S. Kimura, N. Tamura, and C. Kaito, A new preparation method of ZnO cubic phase particle and its IR spectrum, *Jpn. J. Appl. Phys.*, **41**, 5529–5532, 2002.
- [4] F. Decremps, J.Z. Jiang, and R.C. Liebermann, New phase boundary and high-pressure thermoelasticity of ZnO, *Europhys. Lett.*, **51**, 268–274, 2000.
- [5] Z.L. Wang, Zinc oxide nanostructures: Growth, properties and applications, *J. Phys.: Condens. Matter*, **16**, R829–R858, 2004.
- [6] D.C. Reynolds, D.C. Look, and B. Jogai, Optically pumped ultraviolet lasing from ZnO, *Solid State Commun.*, **99**, 873–875, 1996.
- [7] D.M. Bagnall, Y.F. Chen, Z. Zhu, T. Yao, S. Koyama, M.Y. Shen, and T. Goto, Optically pumped lasing of ZnO at room temperature, *Appl. Phys. Lett.*, **70**, 2230–2232, 1997.
- [8] C. Klingshirn, R. Hauschild, J. Fallert, and H. Kalt, Room-temperature stimulated emission of ZnO: Alternatives to excitonic lasing, *Phys. Rev. B*, **75**, 115203, 2007.

- [9] Y. Chen, N.T. Tuan, Y. Segawa, H. Ko, S. Hong, and T. Yao, Stimulated emission and optical gain in ZnO epilayers grown by plasma-assisted molecular-beam epitaxy with buffers, *Appl. Phys. Lett.*, **78**, 1469–1471, 2001.
- [10] T. Makino, Y. Segawa, A. Ohtomo, K. Tamura, and H. Koinuma, Band gap engineering based on $\text{Mg}_x\text{Zn}_{1-x}\text{O}$ and $\text{Cd}_y\text{Zn}_{1-y}\text{O}$ ternary alloy films, *Appl. Phys. Lett.*, **78**, 1237–1239, 2001.
- [11] Th. Gruber, C. Kirchner, R. Kling, F. Reuss, and A. Waag, ZnMgO epilayers and ZnO-ZnMgO quantum wells for optoelectronic applications in the blue and UV spectral region, *Appl. Phys. Lett.*, **84**, 5359–5361, 2004.
- [12] Th. Gruber, C. Kirchner, R. Kling, F. Reuss, A. Waag, F. Bertram, D. Forster, J. Christen, and M. Schreck, Optical and structural analysis of ZnCdO layers grown by metalorganic vapor-phase epitaxy, *Appl. Phys. Lett.*, **83**, 3290–3292, 2003.
- [13] A. Ohtomo, K. Tamura, M. Kawasaki, T. Makino, Y. Segawa, Z.K. Tang, G.K.L. Wong, Y. Matsumoto, and H. Koinuma, Room-temperature stimulated emission of excitons in ZnO/(Mg,Zn)O superlattices, *Appl. Phys. Lett.*, **77**, 2204–2206, 2000.
- [14] S. Fujita, H. Tanaka, and S. Fujita, MBE growth of wide band gap wurtzite MgZnO quasi-alloys with MgO/ZnO superlattices for deep ultraviolet optical functions, *J. Cryst. Growth*, **278**, 264–267, 2005.
- [15] A.V. Thompson, C. Boutwell, J.W. Mares, W.V. Schoenfeld, A. Osinsky, B. Hertog, J.Q. Xie, S.J. Pearton, and D.P. Norton, Thermal stability of CdZnO/ZnO multi-quantum-wells, *Appl. Phys. Lett.*, **91**, 201921, 2007.

- [16] K. Vanheusden, W.L. Warren, C.H. Seager, D.R. Tallant, J.A. Voigt, and B.E. Gnade, Mechanisms behind green photoluminescence in ZnO phosphor powders, *J. Appl. Phys.*, **79**, 7983–7990, 1996.
- [17] W. Shan, W. Walukiewicz, J.W. Ager III, K.M. Yu, H.B. Yuan, H.P. Xin, G. Cantwell, and J.J. Song, Nature of room-temperature photoluminescence in ZnO, *Appl. Phys. Lett.*, **86**, 191911, 2005.
- [18] A.B. Djurisi, Y.H. Leung, W.C.H. Choy, K.W. Cheah, and W.K. Chan, Visible photoluminescence in ZnO tetrapod and multipod structures, *Appl. Phys. Lett.*, **84**, 2635–2637, 2004.
- [19] D.H. Zhang, Q.P. Wang, and Z.Y. Xue, Photoluminescence of ZnO films excited with light of different wavelength, *Appl. Surf. Sci.*, **207**, 20–25, 2003.
- [20] H. Usui, Y. Shimizu, T. Sasaki, and N. Koshizaki, Photoluminescence of ZnO nanoparticles prepared by laser ablation in different surfactant solutions, *J. Phys. Chem. B*, **109**, 120–124, 2005.
- [21] S. Fujihara, Y. Ogawa, and A. Kasai, Tunable visible photoluminescence from ZnO thin films through Mg-doping and annealing, *Chem. Mater.*, **16**, 2965–2968, 2004.
- [22] T. Chen, G.Z. Xing, Z. Zhang, H.Y. Chen, and T. Wu, Tailoring the photoluminescence of ZnO nanowires using Au nanoparticles, *Nanotechnology*, **19**, 435711, 2008.
- [23] Y. Zhang, Z. Zhang, B. Lin, Z. Fu, and J. Xu, Effects of Ag doping on the photoluminescence of ZnO films grown on Si substrates, *J. Phys. Chem. B*, **109**, 19200–19203, 2005.

- [24] S. Baruah and J. Dutta, pH-dependent growth of zinc oxide nanorods, *J. Cryst. Growth*, **311**, 2549–2554, 2009.
- [25] P.X. Gao and Z.L. Wang, Nanoarchitectures of semiconducting and piezoelectric zinc oxide, *J. Appl. Phys.*, **97**, 044304, 2005.
- [26] M. Willander, O. Nur, Q.X. Zhao, L.L. Yang, M. Lorenz, B.Q. Cao, J.Z. Perez, C. Czekalla, G. Zimmermann, M. Grundmann, A. Bakin, A. Behrends, M. Al-Suleiman, A. El-Shaer, A.C. Mofor, B. Postels, A. Waag, N. Boukos, A. Travlos, H.S. Kwack, J. Guinard, and D.L.S. Dang, Zinc oxide nanorod based photonic devices: Recent progress in growth, light emitting diodes and lasers, *Nanotechnology*, **20**, 332001, 2009.
- [27] B. Weintraub, Z. Zhou, Y. Li, and Y. Deng, Solution synthesis of one-dimensional ZnO nanomaterials and their applications, *Nanoscale*, **2**, 1573–1587, 2010.
- [28] L. Zhang and Y.J. Zhu, ZnO micro- and nano-structures: Microwave-assisted solvothermal synthesis, morphology control and photocatalytic properties, *Appl. Phys. A*, **97**, 847–852, 2009.
- [29] S. Baruah and J. Dutta, Hydrothermal growth of ZnO nanostructures, *Sci. Technol. Adv. Mat.*, **10**, 013001, 2009.
- [30] K. Kitamura, T. Yatsui, M. Ohtsu, and G.C. Yi, Fabrication of vertically aligned ultrafine ZnO nanorods using metalorganic vapor phase epitaxy with a two-temperature growth method, *Nanotechnology*, **19**, 175305, 2008.

- [31] P. Sudhagar, R.S. Kumar, J.H. Jung, W. Cho, R. Sathyamoorthy, J. Won, and Y.S. Kang, Facile synthesis of highly branched jacks-like ZnO nanorods and their applications in dye-sensitized solar cells, *Mater. Res. Bull.*, **46**, 1473–1479, 2011.
- [32] Y.J. Xing, Z.H. Xi, Z.Q. Xue, X.D. Zhang, J.H. Song, R.M. Wang, J. Xu, Y. Song, S.L. Zhang, and D.P. Yu, Optical properties of the ZnO nanotubes synthesized via vapor phase growth, *Appl. Phys. Lett.*, **83**, 1689–1691, 2003.
- [33] H. Hu, X. Huang, C. Deng, X. Chen, and Y. Qian, Hydrothermal synthesis of ZnO nanowires and nanobelts on a large scale, *Mater. Chem. Phys.*, **106**, 58–62, 2007.
- [34] P.X. Gao and Z.L. Wang, High-yield synthesis of single-crystal nanosprings of ZnO, *Small*, **1**, 945–949, 2005.
- [35] W.L. Hughes and Z.L. Wang, Controlled synthesis and manipulation of ZnO nanorings and nanobows, *Appl. Phys. Lett.*, **86**, 043106, 2005.
- [36] M.M. Brewster, M.-Y. Lu, S.K. Lim, M.J. Smith, X. Zhou, and S. Gradecak, The growth and optical properties of ZnO nanowalls, *J. Phys. Chem. Lett.*, **2**, 1940–1945, 2011.
- [37] K. Yu, Q. Zhang, J. Wu, L. Li, Y. Xu, S. Huang, and Z. Zhu, Growth and optical applications of centimeter-long ZnO nanocombs, *Nano Res.*, **1**, 221–228, 2008.
- [38] Q. Wan, T.H. Wang, and J.C. Zhao, Enhanced photocatalytic activity of ZnO nanotetrapods, *Appl. Phys. Lett.*, **87**, 1–3, 2005.
- [39] F. Barka-Bouaifel, B. Sieber, N. Bezzi, J. Benner, P. Roussel, L. Boussekey, S. Szunerits, and R. Boukherrou, Synthesis and photocatalytic activity of iodine-doped ZnO nanoflowers, *J. Mater. Chem.*, **21**, 10982–10989, 2011.

- [40] P.X. Gao, W. Mai, and Z.L. Wang, Superelasticity and nanofracture mechanics of ZnO nanohelices, *Nano Lett.*, **6**, 2536–2543, 2006.
- [41] J.Y. Lao, J.G. Wen, and Z.F. Ren, Hierarchical ZnO nanostructures, *Nano Lett.*, **2**, 1287–1291, 2002.
- [42] T. Zhang, W. Dong, M. Keeter-Brewer, S. Konar, R.N. Njabon, and Z.R. Tian, Site-specific nucleation and growth kinetics in hierarchical nanosyntheses of branched ZnO crystallites, *J. Am. Chem. Soc.*, **128**, 10960–10968, 2006.
- [43] C. Cheng, B. Liu, H. Yang, W. Zhou, L. Sun, R. Chen, S.F. Yu, J. Zhang, H. Gong, H. Sun, and H.J. Fan, Hierarchical assembly of ZnO nanostructures on SnO₂ backbone nanowires: Low-temperature hydrothermal preparation and optical properties, *ACS Nano*, **3**, 3069–3076, 2009.
- [44] F. Lu, W. Cai, and Y. Zhang, ZnO hierarchical micro/nanoarchitectures: Solvothermal synthesis and structurally enhanced photocatalytic performance, *Adv. Funct. Mater.*, **18**, 1047–1056, 2008.
- [45] Z.W. Pan, Z.R. Dai, and Z.L. Wang, Nanobelts of semiconducting oxides, *Science*, **291**, 1947–1949, 2001.
- [46] M.H. Huang, Y.Y. Wu, H. Feick, N. Tran, E. Weber, and P.D. Yang, Catalytic growth of zinc oxide nanowires by vapor transport, *Adv. Mater.*, **13**, 113–116, 2001.
- [47] B.D. Yao, Y.F. Chan, and N. Wang, Formation of ZnO nanostructures by a simple way of thermal evaporation, *Appl. Phys. Lett.*, **81**, 757–759, 2002.

- [48] W.I. Park, G.C. Yi, M.Y. Kim, and S.J. Pennycook, ZnO Nanoneedles grown vertically on Si substrates by non-catalytic vapor-phase epitaxy, *Adv. Mater.*, **14**, 1841–1843, 2002.
- [49] W.I. Park, D.H. Kim, S.W. Jung, and G.C. Yi, Metalorganic vapor-phase epitaxial growth of vertically well-aligned ZnO nanorods, *Appl. Phys. Lett.*, **80**, 4232–4234, 2002.
- [50] H. Yuan and Y. Zhang, Preparation of well-aligned ZnO whiskers on glass substrate by atmospheric MOCVD, *J. Cryst. Growth*, **263**, 119–124, 2004.
- [51] Y.W. Heo, V. Varadarajan, M. Kaufman, K. Kim, D.P. Norton, F. Ren, and P.H. Fleming, Site-specific growth of ZnO nanorods using catalysis-driven molecular-beam epitaxy, *Appl. Phys. Lett.*, **81**, 3046–3048, 2002.
- [52] Y. Sun, G.M. Fuge, and M.N.R. Ashfold, Growth of aligned ZnO nanorod arrays by catalyst-free pulsed laser deposition methods, *Chem. Phys. Lett.*, **396**, 21–26, 2004.
- [53] J.I. Hong, J. Bae, Z.L. Wang, and R.L. Snyder, Room-temperature, texture-controlled growth of ZnO thin films and their application for growing aligned ZnO nanowire arrays, *Nanotechnology*, **20**, 085609, 2009.
- [54] L. Vayssieres, Growth of arrayed nanorods and nanowires of ZnO from aqueous solutions, *Adv. Mater.*, **15**, 464–466, 2003.
- [55] A. Sugunan, H.C. Warad, M. Boman, and J. Dutta, Zinc oxide nanowires in chemical bath on seeded substrates: Role of hexamine, *J. Sol-Gel Sci. Technol.*, **39**, 49–56, 2006.

- [56] S. Bang, S. Lee, Y. Ko, J. Park, S. Shin, H. Seo, and H. Jeon, Photocurrent detection of chemically tuned hierarchical ZnO nanostructures grown on seed layers formed by atomic layer deposition, *Nanoscale Res. Lett.*, **7**, 290, 2012.
- [57] M. Ohyama, H. Kozuka, and T. Yoko, Sol-gel preparation of ZnO films with extremely preferred orientation along (002) plane from zinc acetate solution, *Thin Solid Films*, **306**, 78–85, 1997.
- [58] J.H. Lee, K.-H. Ko, and B.-O. Park, Electrical and optical properties of ZnO transparent conducting films by the sol-gel method, *J. Cryst. Growth*, **247**, 119–125, 2003.
- [59] G. Srinivasan, N. Gopalakrishnan, Y.S. Yu, R. Kesavamoorthy, and J. Kumar, Influence of post-deposition annealing on the structural and optical properties of ZnO thin films prepared by sol-gel and spin-coating method, *Superlattices Microstruct.*, **43**, 112–119, 2008.
- [60] B.K. Choi, D.H. Chang, Y.S. Yoon, and S.J. Kang, Optical characterization of ZnO thin films deposited by sol-gel method, *J. Mater. Sci.: Mater. Electron.*, **17**, 1011–1015, 2006.
- [61] S.W. Xue, X.T. Zu, L.X. Shao, Z.L. Yuan, W.G. Zheng, X.D. Jiang, and H. Deng, Effects of annealing on optical properties of Zn-implanted ZnO thin films, *J. Alloys Compd.*, **458**, 569–573, 2008.
- [62] G. Torres, C.I. Zuniga, S.A. Mayen, R. Castanedo, and O. Zelaya, Optical and structural properties of the sol-gel-prepared ZnO thin films and their effect on the photocatalytic activity, *Sol. Energy Mater. Sol. Cells*, **93**, 55–59, 2009.

- [63] L. Vayssieres, K. Keis, S.E. Lindquist, and A. Hagfeldt, Purpose-built anisotropic metal oxide material: 3D highly oriented microrod array of ZnO, *J. Phys. Chem. B*, **105**, 3350–3352, 2001.
- [64] J.M. Dreyfous, S.B. Jones, and Y. Sayed, Hexamethylenetetramine: A review, *Am. Ind. Hyg. Assoc. J.*, **50**, 579–585, 1989.
- [65] K. Govender, D.S. Boyle, P.B. Kenway, and P. O’Brien, Understanding the factors that govern the deposition and morphology of thin films of ZnO from aqueous solution, *J. Mater. Chem.*, **14**, 2575–2591, 2004.
- [66] I.S. Ahuja, C.L. Yadava, and R. Singh, Structural information on manganese(II), cobalt(II), nickel(II), zinc(II) and cadmium (II) sulphate complexes with hexamethylenetetramine (a potentially tetradentate ligand) from their magnetic moments, electronic and infrared spectra, *J. Mol. Struct.*, **81**, 229–234, 1982.
- [67] S. Ma, G. Fang, C. Li, S. Sheng, L. Fang, Q. Fu, and X.-Z. Zhao, Controllable synthesis of vertically aligned ZnO nanorod arrays in aqueous solution, *J. Nanosci. Nanotechnol.*, **6**, 2062–2066, 2006.
- [68] M. Ladanov, M.K. Ram, G. Matthews, and A. Kumar, Structure and opto-electrochemical properties of ZnO nanowires grown on n-Si substrate, *Langmuir*, **27**, 9012–9017, 2011.
- [69] Y.F. Gao, M. Nagai, T.C. Chang, and J.J. Shyue, Solution-derived ZnO nanowire array film as photoelectrode in dyesensitized solar cells, *Cryst. Growth Des.*, **7**, 2467–2471, 2007.

- [70] D.S. Boyle, K. Govender, and P. O'Brien, Novel low temperature solution deposition of perpendicularly orientated rods of ZnO: Substrate effects and evidence of the importance of counter-ions in the control of crystallite growth, *Chem. Commun.*, 80–81, 2002.
- [71] R.B. Peterson, C.L. Fields, and B.A. Gregg, Epitaxial chemical deposition of ZnO nanocolumns from NaOH solutions, *Langmuir*, 20, 5114–5118, 2004.
- [72] Z.Z. Zhou and Y.L. Deng, Kinetics study of ZnO nanorod growth in solution, *J. Phys. Chem. C*, **113**, 19853–19858, 2009.
- [73] L.E. Greene, M. Law, D.H. Tan, M. Montano, J. Goldberger, G. Somorjai, and P. Yang, General route to vertical ZnO nanowire arrays using textured ZnO seeds, *Nano Lett.*, **5**, 1231–1236, 2005.
- [74] S. Baruah and J. Dutta, Effect of seeded substrates on hydrothermally grown ZnO nanorods, *J. Sol-Gel Sci. Technol.*, **50**, 456–464, 2009.
- [75] H. Ghayour, H.R. Rezaie, S. Mirdamadi, and A.A. Nourbakhsh, The effect of seed layer thickness on alignment and morphology of ZnO nanorods, *Vacuum*, **86**, 101–105, 2011.
- [76] W.Y. Wu, C.C. Yeh, and J.M. Ting, Effects of seed layer characteristics on the synthesis of ZnO nanowires, *J. Am. Ceram. Soc.*, **92**, 2718–2723, 2009.
- [77] G. Kenanakis, D. Vernardou, E. Koudoumas, and N. Katsarakis, Growth of *c*-axis oriented ZnO nanowires from aqueous solution: The decisive role of a seed layer for controlling the wires' diameter, *J. Cryst. Growth*, **311**, 4799–4804, 2009.

- [78] L.W. Ji, S.M. Peng, J.S. Wu, W.S. Shih, C.Z. Wu, and I.T. Tang, Effect of seed layer on the growth of well-aligned ZnO nanowires, *J. Phys. Chem. Solids*, **70**, 1359–1362, 2009.
- [79] M.N.R. Ashfold, R.P. Doherty, N.G. Ndifor-Angwafor, D.J. Riley, and Y. Sun, The kinetics of the hydrothermal growth of ZnO nanostructures, *Thin Solid Films*, **515**, 8679–8683, 2007.
- [80] Y. Zhou, W. Wu, G. Hu, H. Wu, and S. Cui, Hydrothermal synthesis of ZnO nanorod arrays with the addition of polyethyleneimine, *Mater. Res. Bull.*, **43**, 2113–2118, 2008.
- [81] L.-Y. Chen, Y.-T. Yin, C.-H. Chen, and J.-W. Chiou, Influence of polyethyleneimine and ammonium on the growth of ZnO nanowires by hydrothermal method, *J. Phys. Chem. C*, **115**, 20913–20919, 2011.
- [82] S. Xu, C. Lao, B. Weintraub, and Z.L. Wang, Density-controlled growth of aligned ZnO nanowire arrays by seedless chemical approach on smooth surfaces, *J. Mater. Res.*, **23**, 2072–2077, 2008.
- [83] S.F. Wang, T.Y. Tseng, Y.R. Wang, C.Y. Wang, H.C. Lu, and W.L. Shih, Effects of preparation conditions on the growth of ZnO nanorod arrays using aqueous solution method, *Int. J. Appl. Ceram. Tec.*, **5**, 419–429, 2008.
- [84] A.R. Kim, J.-Y. Lee, B.R. Jang, J.Y. Lee, H.S. Kim, and N.W. Jang, Effect of Zn^{2+} source concentration on hydrothermally grown ZnO nanorods, *J. Nanosci. Nanotechnol.*, **11**, 6395–6399, 2011.

- [85] O. Akhavan, M. Mehrabian, K. Mirabbaszadeh, and R. Azimirad, Hydrothermal synthesis of ZnO nanorod arrays for photocatalytic inactivation of bacteria, *J. Phys. D: Appl. Phys.*, **42**, 225305, 2009.
- [86] Z. Yuan, J. Yu, N. Wang, and Y. Jiang, Well-aligned ZnO nanorod arrays from diameter-controlled growth and their application in inverted polymer solar cell, *J. Mater. Sci.*, **12**, 502–507, 2011.
- [87] J.J. Hassan, Z. Hassan, and H. Abu-Hassan, High-quality vertically aligned ZnO nanorods synthesized by microwave assisted CBD with ZnO-PVA complex seed layer on Si substrates, *J. Alloys Compd.*, **509**, 6711–6719, 2011.
- [88] H.E. Unalan, P. Hiralal, N. Rupesinghe, S. Dalal, W.I. Milne, and G.A.J. Amaratunga, Rapid synthesis of aligned zinc oxide nanowires, *Nanotechnology*, **19**, 255608, 2008.
- [89] S.H. Jung, E. Oh, K.H. Lee, W. Park, and S.H. Jeong, A sonochemical method for fabricating aligned ZnO nanorods, *Adv. Mater.*, **19**, 749–753, 2007.
- [90] L. Shi, K.Y. Bao, J. Cao, and Y.T. Qian, Sunlight-assisted fabrication of a hierarchical ZnO nanorod array structure, *Cryst. Eng. Comm.*, **11**, 2009–2014, 2009.
- [91] P.C. Chang, Z. Fan, C.J. Chien, D. Stichtenoth, C. Ronning, and J.G. Lu, High-performance ZnO nanowire field effect transistors, *Appl. Phys. Lett.*, **89**, 133113, 2006.
- [92] J.-I. Song, J.-S. Park, H. Kim, Y.-W. Heo, J.-H. Lee, J.-J. Kim, and B.D. Choi, Transparent amorphous indium zinc oxide thin-film transistors fabricated at room temperature, *Appl. Phys. Lett.*, **90**, 022106, 2007.

- [93] C.H. Liu, J.A. Zapien, Y. Yao, X.M. Meng, C.S. Lee, S.S. Fan, Y. Lifshitz, and S.T. Lee, High-density, ordered ultraviolet light-emitting ZnO nanowire arrays, *Adv. Mater.*, **15**, 838–841, 2003.
- [94] A. Tsukazaki, A. Ohtomo, T. Onuma, M. Ohtani, T. Makino, M. Sumiya, K. Ohtani, S.F. Chichibu, S. Fuke, Y. Segawa, H. Ohno, H. Koinuma, and M. Kawasaki, Repeated temperature modulation epitaxy for p-type doping and light-emitting diode based on ZnO, *Nat. Mater.*, **4**, 42–46, 2005.
- [95] S. Chu, G. Wang, W. Zhou, Y. Lin, L. Chernyak, J. Zhao, J. Kong, L. Li, J. Ren, and J. Liu, Electrically pumped waveguide lasing from ZnO nanowires, *Nat. Nanotechnol.*, **6**, 506–510, 2011.
- [96] D. Hofstetter, Y. Bonetti, F.R. Giorgetta, A.-H. El-Shaer, A. Bakin, A. Waag, R. Schmidt-Grund, M. Schubert, and M. Grundmann, Demonstration of an ultraviolet ZnO-based optically pumped third order distributed feedback laser, *Appl. Phys. Lett.*, **91**, 111108, 2007.
- [97] H. Kind, H. Yan, B. Messer, M. Law, and P. Yang, Nanowire ultraviolet photodetectors and optical switches, *Adv. Mater.*, **14**, 158–160, 2002.
- [98] M. Mehrabian, R. Azimirad, K. Mirabbaszadeh, H. Afarideh, and M. Davoudian, UV detecting properties of hydrothermal synthesized ZnO nanorods, *Physica E*, **43**, 1141–1145, 2011.
- [99] Z.L. Wang, R. Yang, J. Zhou, Y. Qin, C. Xu, Y. Hu, and S. Xu, Lateral nanowire/nanobelt based nanogenerators, piezotronics and piezophototronics, *Mater. Sci. Eng., R*, **70**, 320–329, 2010.

- [100] S. Niu, Y. Hu, X. Wen, Y. Zhou, F. Zhang, L. Lin, S. Wang, and Z.L. Wang, Enhanced performance of flexible ZnO nanowire based room-temperature oxygen sensors by piezotronic effect, *Adv. Mater.*, **25**, 3701–3706, 2013.
- [101] F. Xue, L. Zhang, W. Tang, C. Zhang, W. Du, and Z.L. Wang, Piezotronic effect on ZnO nanowire film based temperature sensor, *ACS Appl. Mater. Interfaces*, **6**, 5955–5961, 2014.
- [102] S.H. Lee, J.S. Lee, W.B. Ko, S.N. Cha, J.I. Sohn, J.M. Kim, J.G. Park, Y. Park, and J.P. Hong, Solution-processed Ag-doped ZnO nanowires grown on flexible polyester for nanogenerator applications, *Nanoscale*, **5**, 9609–9614, 2013.
- [103] A.D. Pasquier, H. Chen, and Y. Lu, Dye sensitized solar cells using well-aligned zinc oxide nanotip arrays, *Appl. Phys. Lett.*, **89**, 253513, 2006.
- [104] C.Y. Jiang, X.W. Sun, G.Q. Lo, D.L. Kwong, and J.X. Wang, Improved dye-sensitized solar cells with a ZnO-nanoflower photoanode, *Appl. Phys. Lett.*, **90**, 263501, 2007.
- [105] N. Sakai, T. Miyasaka, and T.N. Murakami, Efficiency enhancement of ZnO-based dye-sensitized solar cells by low-temperature TiCl_4 treatment and dye optimization, *J. Phys. Chem. C*, **117**, 10949–10956, 2013.
- [106] M. Boucharef, C.D. Bin, M.S. Boumaza, M. Colas, H.J. Snaith, B. Ratier, and J. Boucle, Solid-state dye-sensitized solar cells based on ZnO nanocrystals, *Nanotechnology*, **21**, 205203, 2010.

- [107] R.T. Ginting, C.C. Yap, M. Yahaya, and M.M. Salleh, Solution-processed Ga-doped ZnO nanorod arrays as electron acceptors in organic solar cells, *ACS Appl. Mater. Interfaces*, **6**, 5308–5318, 2014.
- [108] M. Thambidurai, J.Y. Kim, J. Song, Y. Ko, H.-J. Song, C.-M. Kang, N. Muthukumarasamy, D. Velauthapillai, and C. Lee, High performance inverted organic solar cells with solution processed Ga-doped ZnO as an interfacial electron transport layer, *J. Mater. Chem. C*, **1**, 8161–8166, 2013.
- [109] Q. Wan, Q.H. Li, Y.J. Chen, T.H. Wang, X.L. He, J.P. Li, and C.L. Lin, Fabrication and ethanol sensing characteristics of ZnO nanowire gas sensors, *Appl. Phys. Lett.*, **84**, 3654–3656, 2004.
- [110] S.J. Ippolito, S. Kandasamy, K. Kalantar-Zadeh, W. Wlodarski, K. Galatsis, G. Kiriakidis, N. Katsarakis, and M. Suchea, Highly sensitive layered ZnO/LiNbO₃ SAW device with InO_x selective layer for NO₂ and H₂ gas sensing, *Sens. Actuators B*, **111–112**, 207–212, 2005.
- [111] H.T. Wang, B.S. Kang, F. Ren, L.C. Tien, P.W. Sadik, D.P. Norton, S.J. Pearton, and J. Lin, Hydrogen-selective sensing at room temperature with ZnO nanorods, *Appl. Phys. Lett.*, **86**, 243503, 2005.
- [112] J. Wu, Z. Lan, S. Hao, P. Li, J. Lin, M. Huang, L. Fang, and Y. Huang, Progress on the electrolytes for dye-sensitized solar cells, *Pure Appl. Chem.*, **80**, 2241–2258, 2008.
- [113] J.-K. Lee and M. Yang, Progress in light harvesting and charge injection of dye-sensitized solar cells, *Mater. Sci. Eng., B*, **176**, 1142–1160, 2011.

- [114] Z. Ning, Y. Fu, and H. Tian, Improvement of dye-sensitized solar cells: What we know and what we need to know, *Energy Environ. Sci.*, **3**, 1170–1181, 2010.
- [115] Z.L. Wang and J.H. Song, Piezoelectric nanogenerators based on zinc oxide nanowire arrays, *Science*, **312**, 242–246, 2006.
- [116] M.-H. Zhao, Z.-L. Wang, and S.X. Mao, Piezoelectric characterization of individual zinc oxide nanobelt probed by piezoresponse force microscope, *Nano Lett.*, **4**, 587–590, 2004.

CHAPTER THREE

GALLIUM-DOPED ZINC OXIDE NANORODS GROWN ON GLASS

Introduction

Transparent conductive oxides (TCOs) with high optical transmittance in the visible range and high electrical conductivity are essential for the use as transparent electrodes in various applications, including flat panel displays, photovoltaic cells, transparent thin film transistors, light emitting diodes, and semiconductor lasers [1–6]. Currently, indium tin oxide (ITO) is commonly used as transparent electrodes in industry due to its high conductivity, work function, and transmittance. Although ITO is probably one of the most successful TCOs, indium is an expensive and rare metal. It is expected that indium will run out within a few decades [7,8]. There has been much interest in finding cheaper, more stable, and environmentally-friendly alternatives. ZnO is a practical candidate for ITO as transparent electrodes [9–11].

ZnO is an intrinsically n-type semiconductor due to the inevitable n-type point defects, such as oxygen vacancies and zinc interstitials, and hydrogen impurities [12–15]. Selective element doping of ZnO provides a method for controlling its structural, optical, electrical, and magnetic properties. Group-I (Li, Na, K, Cu, and Ag) and group-V (N, P, As, and Sb) elements are used for p-type doping, but reliable p-type doping of ZnO with high carrier concentration and mobility remains difficult due to the low solubility of p-type dopants and compensation by a high concentration of n-type defects [16–25]. Intentional n-type doping of ZnO is readily achieved by mainly doping with group-III elements (In, Al, or Ga). Among group-III elements, Ga is the most effective dopant due

to its lower reactivity towards oxygen compared to those of other doped ZnO. In addition, Ga has less influence on the ZnO lattice. Al^{3+} has an ionic radius of 0.54 Å, which is smaller than that of Zn^{2+} (0.74 Å), and Al^{3+} can occupy the place of Zn^{2+} in lattice easily, leading to a reduction of the lattice parameter. In contrast, Ga^{3+} has a similar ionic radius (0.62 Å) to Zn^{2+} , which results in less lattice deformation in ZnO when Ga substitutes for Zn [26–29].

Various techniques have been applied to prepare Ga-doped ZnO, such as chemical vapor deposition, atomic layer deposition, pulsed laser deposition, molecular beam epitaxy, and magnetron sputtering [30–34]. These techniques provide Ga-doped ZnO with high crystal quality under well-controlled vacuum conditions but have some limitations including low product yield and high growth temperature, which results in a limited choice of substrate materials. In contrast, the hydrothermal method enables the preparation of ZnO at much lower temperatures, which makes the process more effective, simplifies the control of dopant concentrations, and allows the use of simple equipment.

In this work, ZnO nanorods were doped using Ga as an n-type dopant by the hydrothermal method for use in transparent electrodes. Vertically well-aligned uniform ZnO nanorod arrays were obtained in the Ga-doped ZnO layers on glass substrates. The undoped and Ga-doped ZnO nanorods were characterized by contact angle goniometer, field-emission scanning electron microscopy (FE-SEM), X-ray diffraction (XRD), ultraviolet/visible/near-infrared spectroscopy, and four-point probe, and a systematic study of structural, optical, and electrical properties of Ga-doped ZnO nanorods as a function of Ga concentration was discussed in detail.

Experimental Details

Synthesis of Ga-Doped ZnO Nanorods on Glass

The ZnO seed layer was implanted on glass substrates using a sol-gel spin-coating method. The sol-gel solution consists of a dissolved zinc acetate dihydrate of 0.5 M in a mixture of its solvent, 2-methoxyethanol, and a stabilizer, monoethanolamine. The solution was stirred for 2 h and was stored at room temperature for 24 h in order to obtain a homogenous solution. The spin-coating process consisted of placing several small drops of sol-gel solution on the substrate and rotating it at 1000 rpm for 10 sec and then at 3000 rpm for 20 sec in order to get a uniformly distributed seed layer across the substrate. After spin coating, the ZnO seed layer was then heated to 350 °C in order to get rid of the organic remnants and to evaporate the precursor solution. This procedure from the spin-coating to the pre-heat treatment was repeated 4 times. The samples were then heated at 500 °C for 30 min to improve the crystalline quality of the ZnO seed layer.

A one-pot hydrothermal method was used to grow the ZnO nanorod arrays on the seed layer. The samples were placed into Teflon containers with a 100 ml aqueous solution of 0.05 M zinc nitrate hexahydrate and 0.05 M hexamethylenetetramine (HMTA). Ga doping was achieved by adding varying amounts of gallium nitrate hydrate to the solutions starting from 0.5 at.% to 3.0 at.%. These solutions were then heated for 6 h at 85 °C to grow the ZnO nanorods on the seed layer. After the reaction, the sample was rinsed thoroughly with deionized water and dried with flowing nitrogen gas in order to remove residual salts.

Characterization

The contact angle goniometer (KSV, CAM 200) was used to determine the surface wettability of the Ga-doped ZnO nanorods. FE-SEM (Hitachi, S-4800) and XRD (Rigaku, ULTIMA IV diffractometer) were used to determine the morphological and structural properties of the Ga-doped ZnO nanorods. The optical properties of the samples were investigated using ultraviolet/visible/near-infrared spectroscopy (Perkin Elmer, Lambda 850) with a reflectance accessory. The electrical properties were determined by measuring the resistivity of the samples using a four-point probe (Keithley).

Effects of Gallium Doping Concentration

Figure 3.1 shows SEM images of the as-grown and Ga-doped ZnO nanorods. A variety of changes in nanorod properties can be seen as the doping concentration increases; the properties are its morphology, size, density, and alignment. The crystal shape of the nanorods changes from pointed and needle-like tips (0.5 and 1.0 at.%) to a more flat hexagon (3.0 at.%). Randomly distributed ZnO nanorods with an average length of 1.7 μm are observed at low Ga concentrations (0.5 at.%). The further incorporation of Ga in the ZnO crystal results in the formation of dense and vertically well-aligned nanorod arrays with a uniform length of 0.83 μm (3.0 at.%). In the solution for the hydrothermal method, Ga ions are inclined to interact with OH^- ions released from HMTA to create complexes. The heterogeneous nucleation is limited due to the reduction of OH^- ions, and a lower number of nucleation sites are formed in the early stage of the

growth process, which results in ZnO nanorods with a larger diameter and smaller length at higher Ga concentration (3.0 at.%) [33,35–37].

The interfacial properties of ZnO nanorods were investigated by contact angle measurements (Figure 3.2). The measurements indicate that the wettability of the ZnO nanorods changed from superhydrophilic to less hydrophilic as doping concentration increased. ZnO nanorods with low Ga concentration (0.5 and 1.0 at.%) exhibit superhydrophilic nature. The highest contact angle of 40.3° was observed from the Ga concentrations of 3.0 at.%. The decrease in hydrophilic properties is due to the denser morphology of the nanorods, which will not accept the liquid as well as a more porous material.

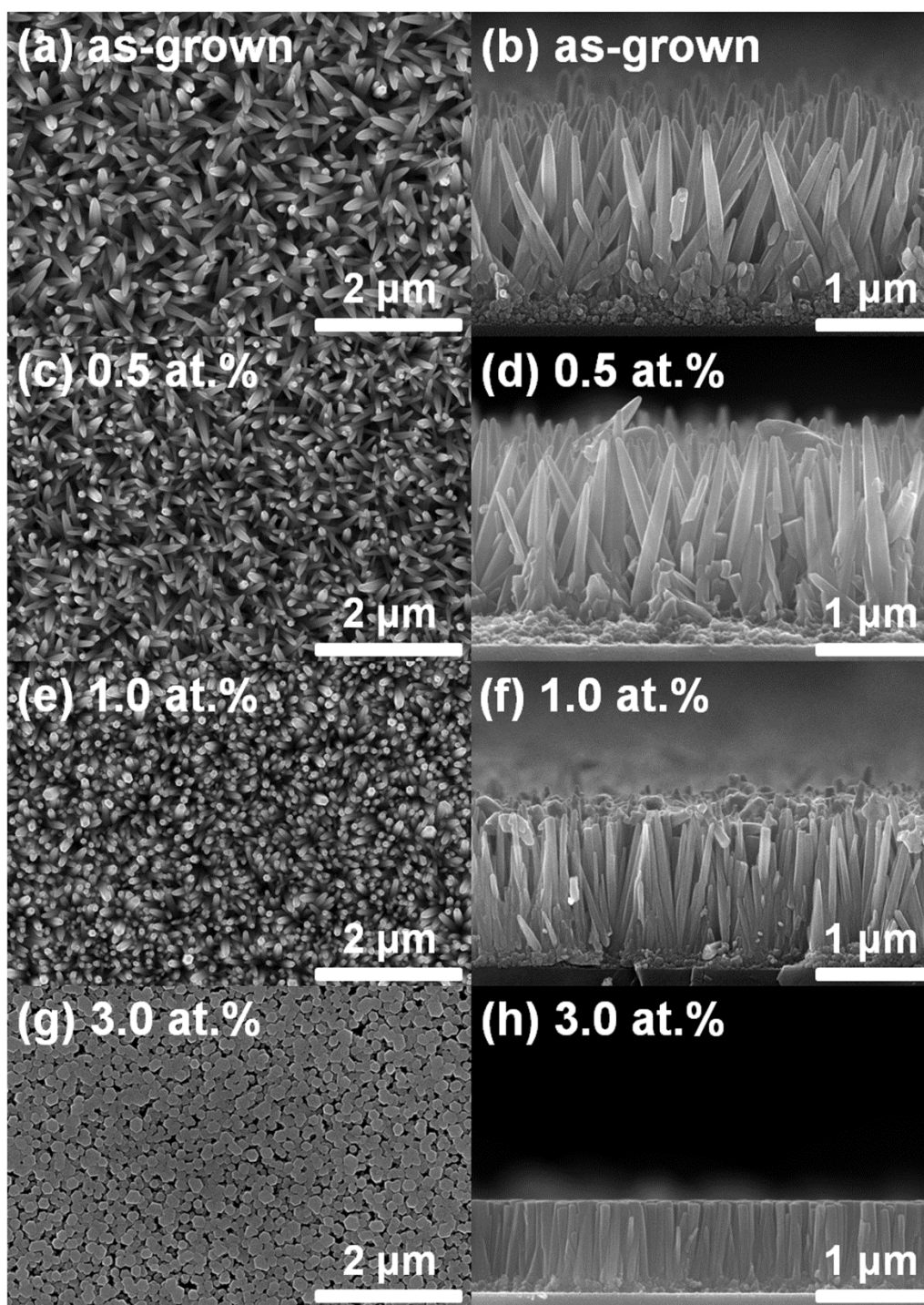


Figure 3.1: SEM images of the ZnO nanorods with different Ga doping concentrations:

(a and b) as-grown, (c and d) 0.5 at.%, (e and f) 1.0 at.%, and (g and h) 3.0 at.%.

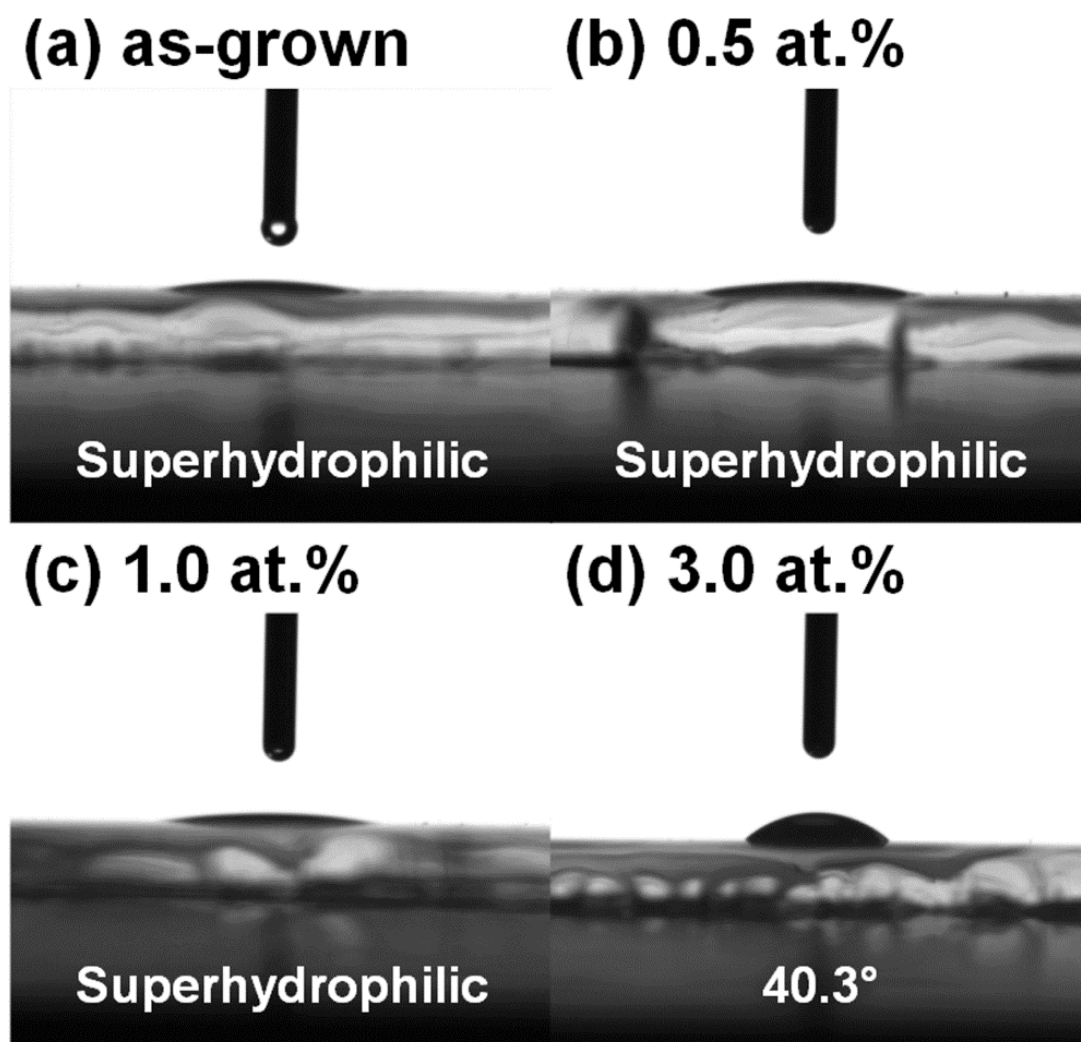


Figure 3.2: Contact angle measurement of the ZnO nanorods with different Ga doping concentrations: (a) as-grown, (b) 0.5 at.%, (c) 1.0 at.%, and (d) 3.0 at.%.

Figure 3.3 shows the XRD patterns of the ZnO nanorods. All the diffraction peaks from the ZnO nanorods are well indexed to the hexagonal wurtzite structure of ZnO. The patterns show mainly the ZnO(002) peak, which is related to the growth direction towards the *c*-axis, with weak peaks including ZnO(101), ZnO(102), and ZnO(103). ZnO crystals are usually grown with a *c*-axis preferred orientation because of the low surface energy of the basal plane in ZnO, leading to a preferred growth in the (002) direction [38–40]. In addition, diffraction peaks related to Ga or other crystalline phases are not observed in the XRD patterns.

In order to determine the preferred orientation, the texture coefficient ($TC_{(hkl)}$) for the peaks from the XRD patterns was calculated using the following equation [41,42]:

$$TC_{(hkl)} = \frac{I_{(hkl)}/I_{0(hkl)}}{1/N \sum_N I_{(hkl)}/I_{0(hkl)}}$$

, where N is the number of diffraction peaks, $I_{(hkl)}$ is the measured relative intensity of the reflection from the (hkl) plane, and $I_{0(hkl)}$ is that from the same plane in a standard reference sample (JCPDS card No. 36-1451). With an increase in Ga doping concentration, $TC_{(002)}$ increases while $TC_{(101)}$, $TC_{(102)}$, and $TC_{(103)}$ decrease (Figure 3.4 and Table 3.1). $TC_{(002)}$ increases from 74.49% for the as-grown sample up to 98.82% for the Ga 3.0 at.% doped sample, which indicates that the incorporation of Ga dopant in ZnO crystal can promote the growth of ZnO nanorods along the *c*-axis direction as confirmed from SEM images shown in Figure 3.1.

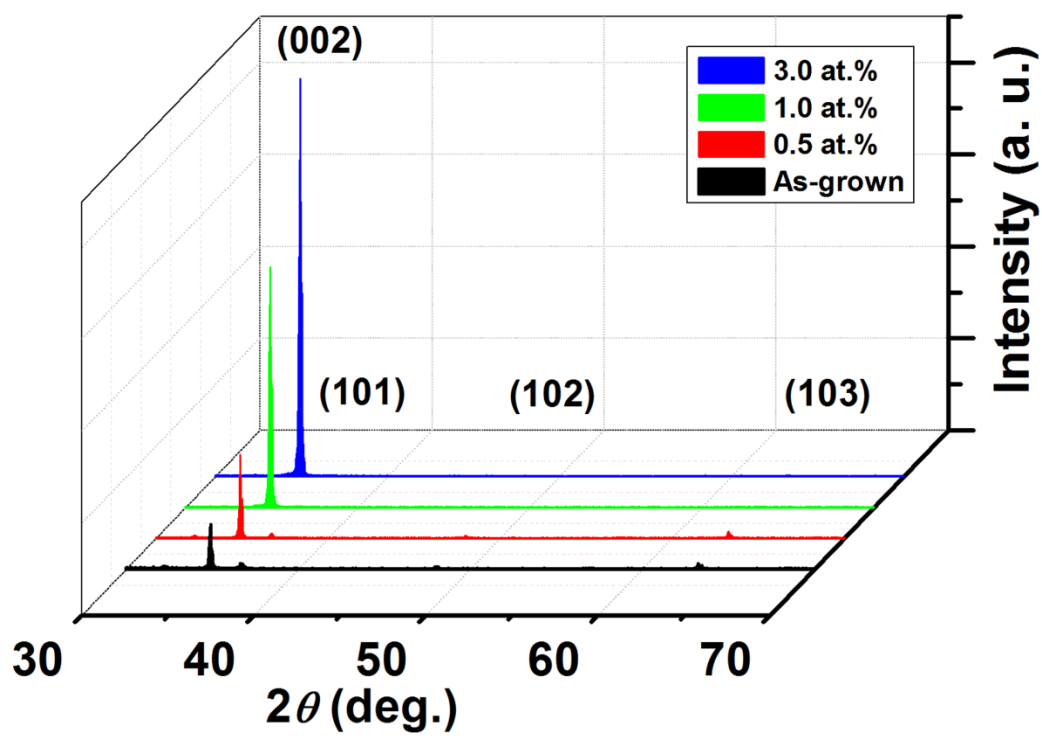


Figure 3.3: XRD patterns of the ZnO nanorods with different Ga doping concentrations.

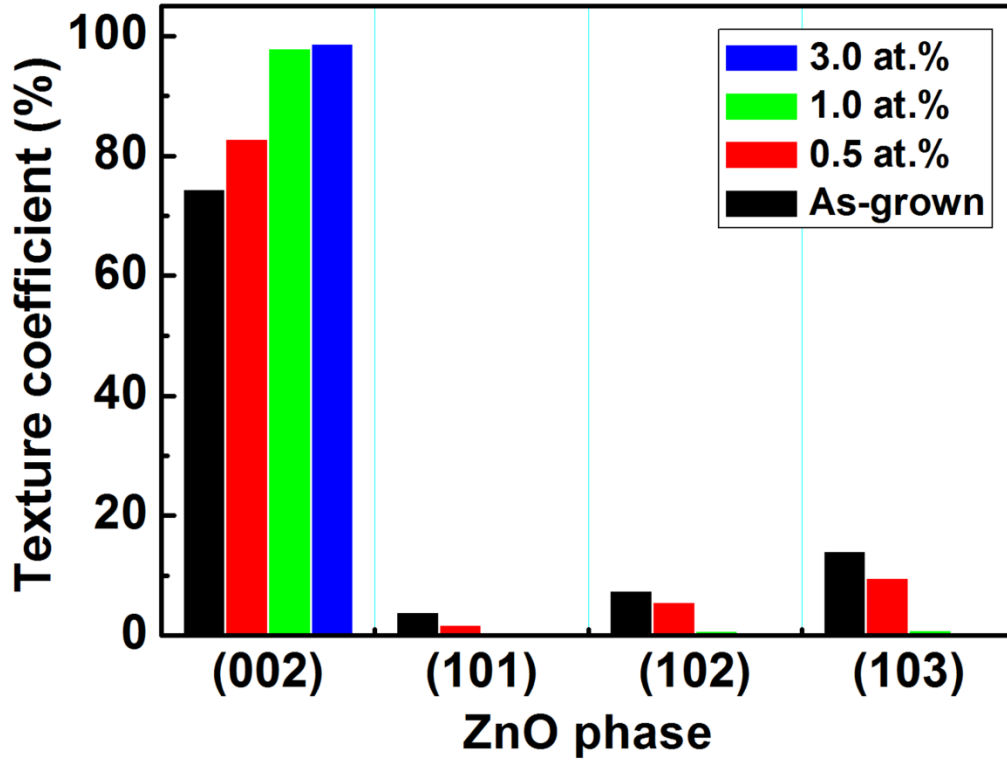


Figure 3.4: Texture coefficient of the ZnO nanorods with different Ga doping concentrations.

Table 3.1: Calculated values of texture coefficients of the ZnO nanorods with different Ga doping concentrations.

Sample	$TC_{(002)}$ (%)	$TC_{(101)}$ (%)	$TC_{(102)}$ (%)	$TC_{(103)}$ (%)
As-grown	74.49	3.87	7.51	14.13
0.5 at. %	82.82	1.81	5.67	9.70
1.0 at. %	97.97	0.32	0.81	0.90
3.0 at. %	98.82	0.20	0.53	0.45

The peak position of the ZnO(002) diffraction shifts toward a higher 2θ value as Ga doping concentration increases, indicating a change in the interplanar spacing in the crystals (Figure 3.5). The a -axis and c -axis lattice constants for the different doping concentration were calculated using the following equations:

$$a = \frac{(0.6237)\lambda}{\sin\theta}$$

$$c = \frac{\lambda}{\sin\theta}$$

, where λ is the wavelength of the Cu-K α radiation (1.5406 Å) and θ is the Bragg angle of the ZnO(002) diffraction. As shown in Figure 3.6, the lattice constants of the as-grown ZnO are close to the values reported for bulk ZnO ($a = 0.32495$ nm and $c = 0.52069$ nm) [43]. Ga doping induces a decrease in both the a -axis and c -axis lattice constants because the ionic radius of Ga³⁺ (0.62 Å) is smaller than that of Zn²⁺ (0.74 Å) [26–29]. This indicates that Ga atoms are successfully incorporated into the Zn site in the ZnO lattice.

The residual stress (σ) and bond length (L) of the ZnO nanorods with different doping concentrations were investigated (Figure 3.7). The residual stress in the ZnO nanorods can be calculated as follows [44]:

$$\sigma = \left(\frac{2c_{13}^2 - C_{33}(C_{11} + C_{12})}{2C_{13}} \right) \times \left(\frac{c - c_0}{c_0} \right)$$

, where C_{ij} ($i, j = 1, 2, 3$) are elastic stiffness constants for ZnO ($C_{11} = 207.0$ GPa, $C_{12} = 117.7$ GPa, $C_{13} = 106.1$ GPa, and $C_{33} = 209.5$ GPa), c_0 is the lattice constant of strain-free ZnO, and c is the lattice constant of the Ga-doped ZnO nanorods in this study. If the stress is positive, the biaxial stress is tensile; if the stress is negative, the biaxial stress is

compressive. All the samples exhibit tensile stress as shown in Figure 3.7. The biaxial stress is observed even in the undoped ZnO nanorods due to the difference in the thermal expansion coefficients between the substrate material and the ZnO nanorods. The tensile stress of the ZnO nanorods increases as doping concentration increases. Based on this analysis, the shifts of the ZnO(002) diffraction toward a higher 2θ value is due to the variation in tensile stress. The bond length of Zn-O is given by

$$L = \sqrt{\frac{a^2}{3} + \left(\frac{1}{2} - u\right)^2 \times c^2}$$

, where u is given by (in the wurtzite structure)

$$u = \frac{a^2}{3c^2} + 0.25$$

and u is related to the lattice constant ratio of a -axis and c -axis of ZnO. There is a decrease in the bond length of the Ga-doped ZnO nanorods due to the smaller Ga atom substituting Zn in the ZnO crystal, such as with the trends of the lattice constants.

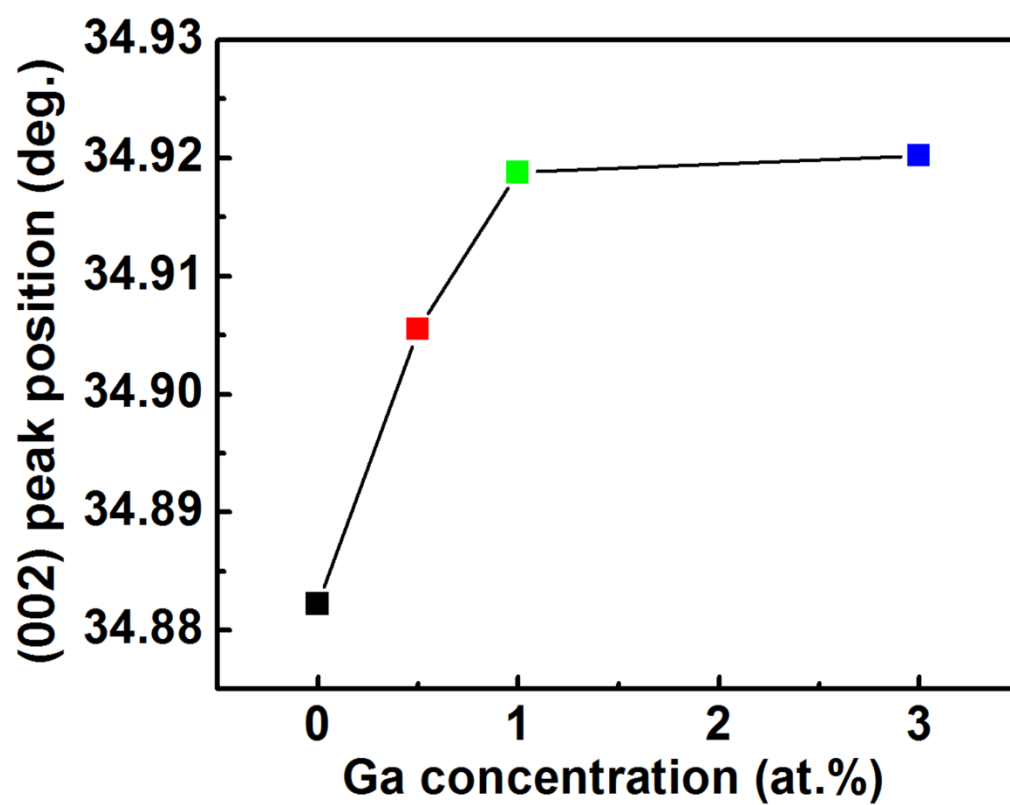


Figure 3.5: Peak position of the ZnO(002) diffraction with different Ga doping concentrations.

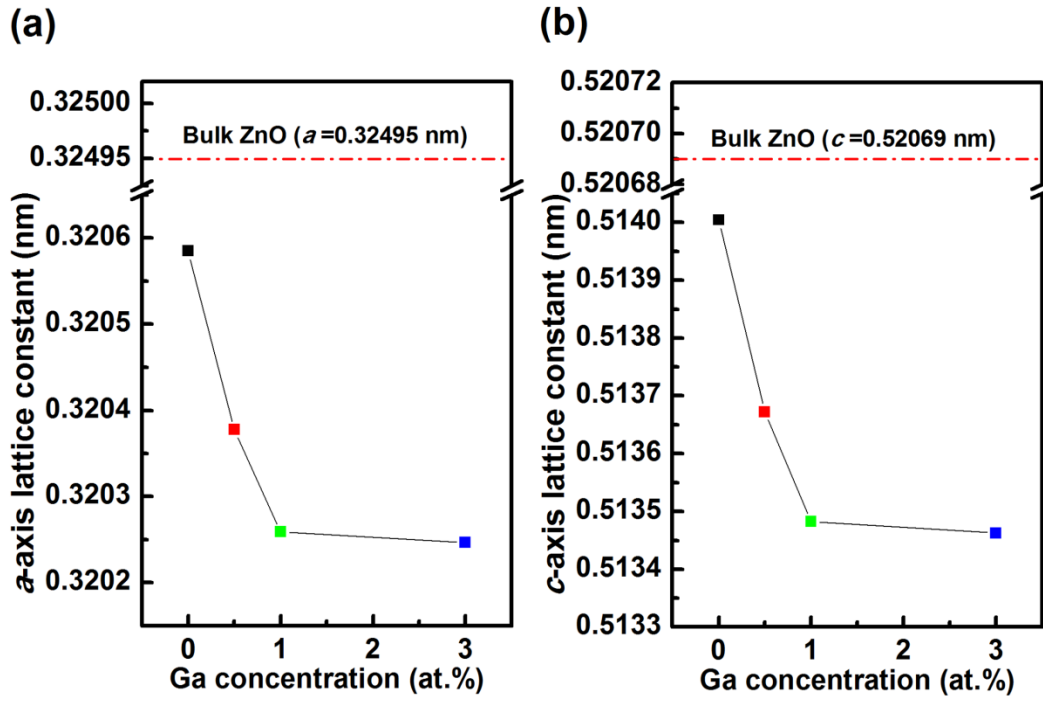


Figure 3.6: Lattice constants of the ZnO nanorods with different Ga doping concentrations: (a) *a*-axis lattice constant and (b) *c*-axis lattice constant.

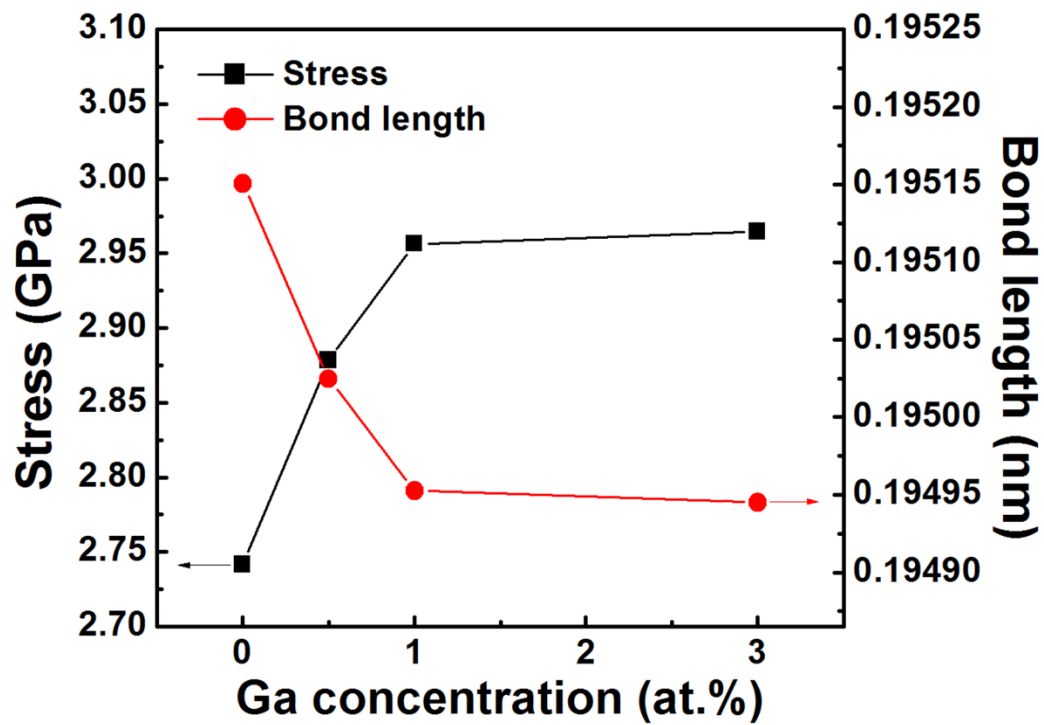


Figure 3.7: Biaxial stress and bond length of the ZnO nanorods with different Ga doping concentrations.

Figure 3.8 shows the optical transmittance spectra of the Ga-doped ZnO nanorods. The inset shows optical reflectance of the Ga-doped ZnO nanorods. An increase in the transmittance is observed as Ga doping concentration increases, with a highest value at 3.0 at.%. The optical transmittance of a material is closely related to the absorption coefficient, surface morphology, and thickness of the material. The absorption coefficient is obtained using the following equation:

$$I = I_0 e^{-\alpha d}$$

, where I and I_0 represent the intensities of the transmitted and incident light, respectively, α is the absorption coefficient, and d is the film thickness. Considering interfaces related to the thin films and the thickness in practical experiments, the transmittance and reflectance of the ZnO-based materials obey the following equation [45]:

$$T = (1 - R)^2 e^{-\alpha d}$$

, where T is the transmittance and R is the reflectance. The absorption coefficients with different Ga doping concentrations are shown in Figure 3.9. Overall, the absorption coefficients for the Ga-doped ZnO nanorods were smaller than that for the undoped ZnO nanorods. Furthermore, the disorder in nanorod placement results in a strong suppression of the transmission due to localized surface plasmon resonances related to the clustering of the rods [46]. Therefore, the improved transmittance can be attributed to the improved vertical alignment of the nanorods, decreased thickness, and decreased absorption coefficient with an increase in the Ga doping concentration. In addition, all of the samples exhibit lower transmittance at shorter wavelength than at longer wavelength because of the Rayleigh scattering of light, which may occur when light travels through a

transparent solid. It is strongly dependent on wavelength ($\sim\lambda^{-4}$) and thus blue light is scattered much more than red light.

The absorption coefficient for a direct-transition semiconductor material obeys the following relation with respect to the optical band gap (E_g) [47]:

$$\alpha h\nu = B(h\nu - E_g)^{1/2}$$

, where h is the Planck's constant, ν is the frequency of the incident photons, and B is a constant related to the electron-hole mobility of the material. The optical band gaps can be obtained by plotting $(\alpha h\nu)^2$ as a function of photon energy and extrapolating the linear regions of the curves near the onset of the absorption edge to the energy axis as shown in Figure 3.10.

Figure 3.11 shows the optical band gap energy as a function of Ga doping concentration. The optical band gap of the ZnO nanorods grown under the Ga doping concentrations of 0.5, 1.0, and 3.0 at.% is 3.226, 3.255, and 3.294 eV, respectively, which indicates that Ga doping significantly influences the optical band gap of the ZnO. The shift in the optical band gap is because of the Burstein-Moss shift and the energy band widening (blue-shift) effect, which results from the increase in the Fermi level of the conduction bands of degenerate semiconductors [47–49]. The donor electrons in the doped semiconductors occupy states at the bottom of the conduction band. Because the Pauli exclusion principle prevents states from being doubly occupied and optical transitions are vertical, the valence electrons require additional energy in order to be excited into the higher energy states in the conduction band so that linear momentum is

conserved. Hence, the Burstein-Moss effect dominates and the band gap widens with increasing carrier concentration in the Ga-doped ZnO nanorods.

Figure 3.12 shows the resistivity of the ZnO nanorods as a function of Ga doping concentration. As the doping concentration increased, the resistivity of the nanorods decreased due to the increase in charge carrier concentration as Ga substituted Zn in the ZnO lattice, releasing an electron into the conduction band. The lowest electrical resistivity was obtained at the doping concentration of 3.0 at.%.

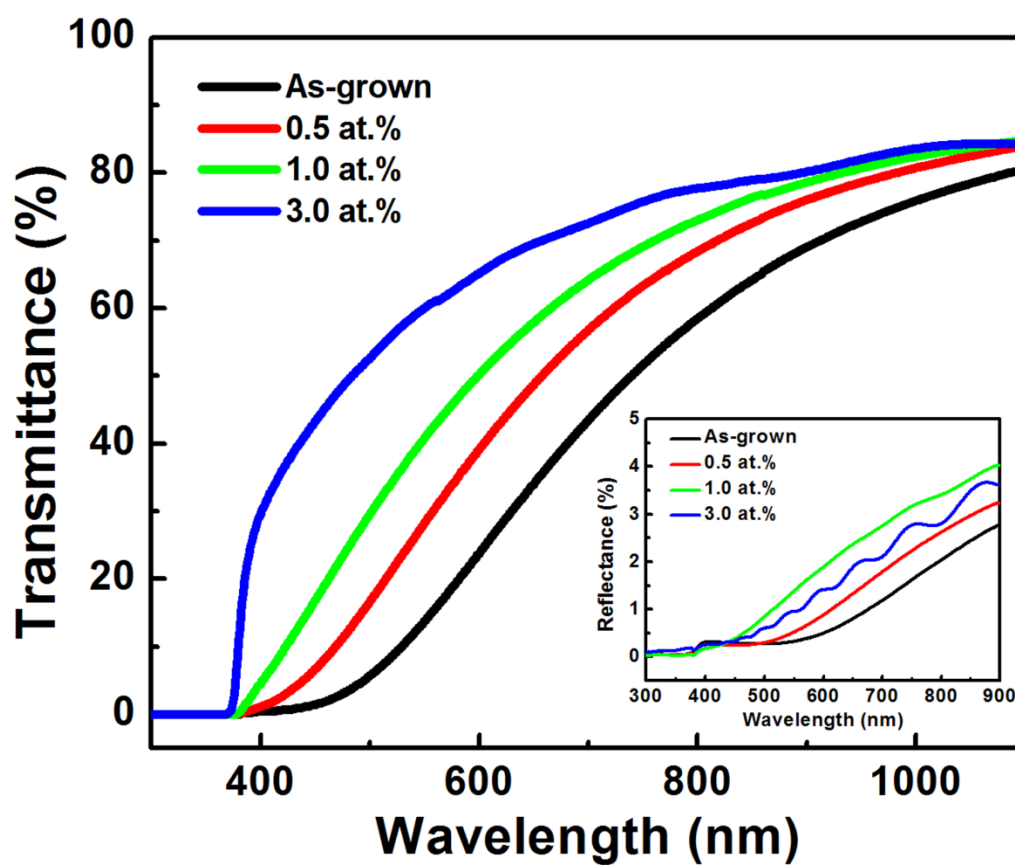


Figure 3.8: Optical transmittance spectra of the ZnO nanorods with different Ga doping concentrations. Inset shows optical reflectance spectra for the same ZnO nanorods.

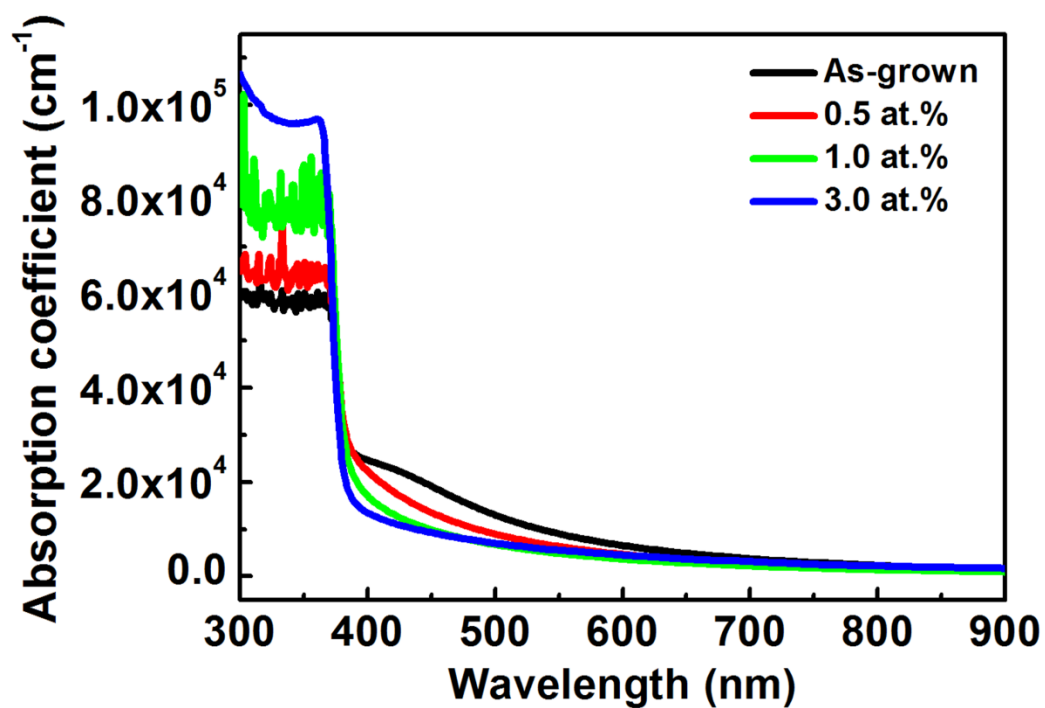


Figure 3.9: Absorption coefficient of the ZnO nanorods with different Ga doping concentrations.

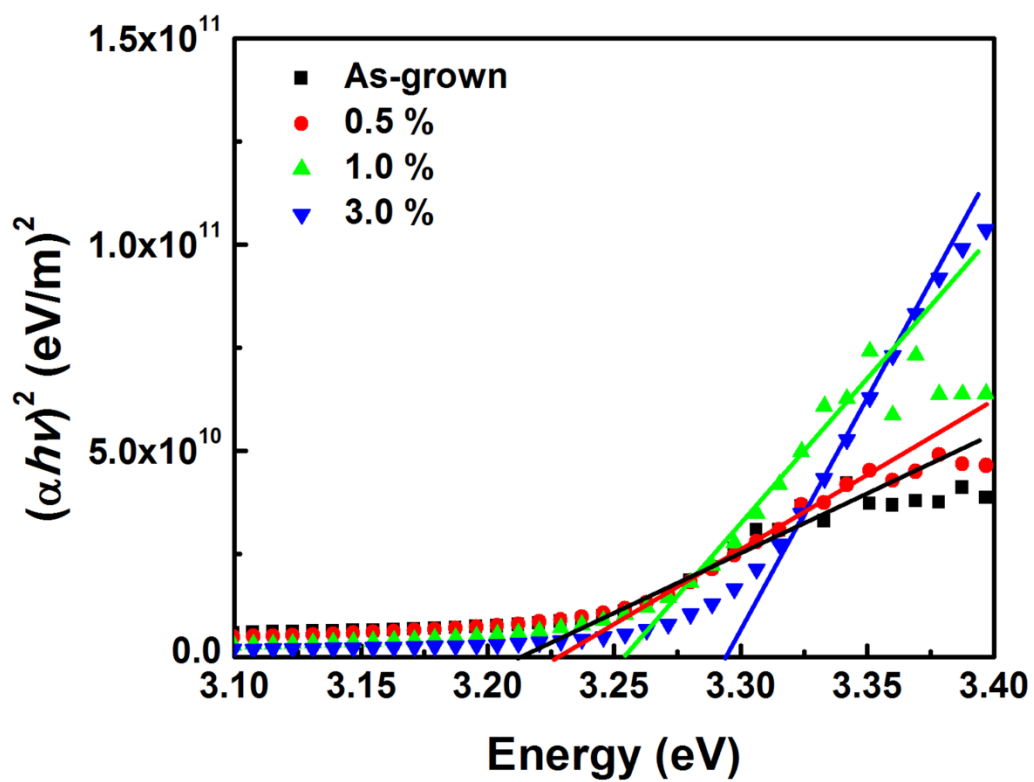


Figure 3.10: $(\alpha h\nu)^2$ plotted as a function of photon energy for the ZnO nanorods with different Ga doping concentrations.

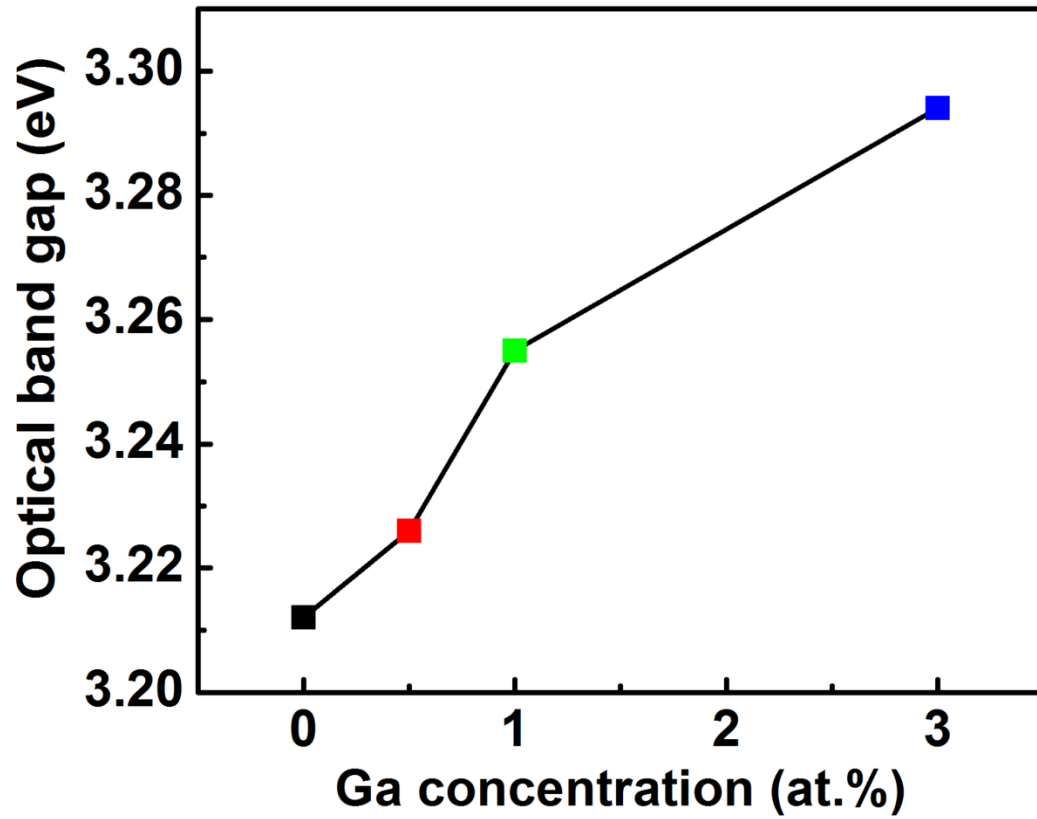


Figure 3.11: Optical band gap energy of the ZnO nanorods with different Ga doping concentrations.

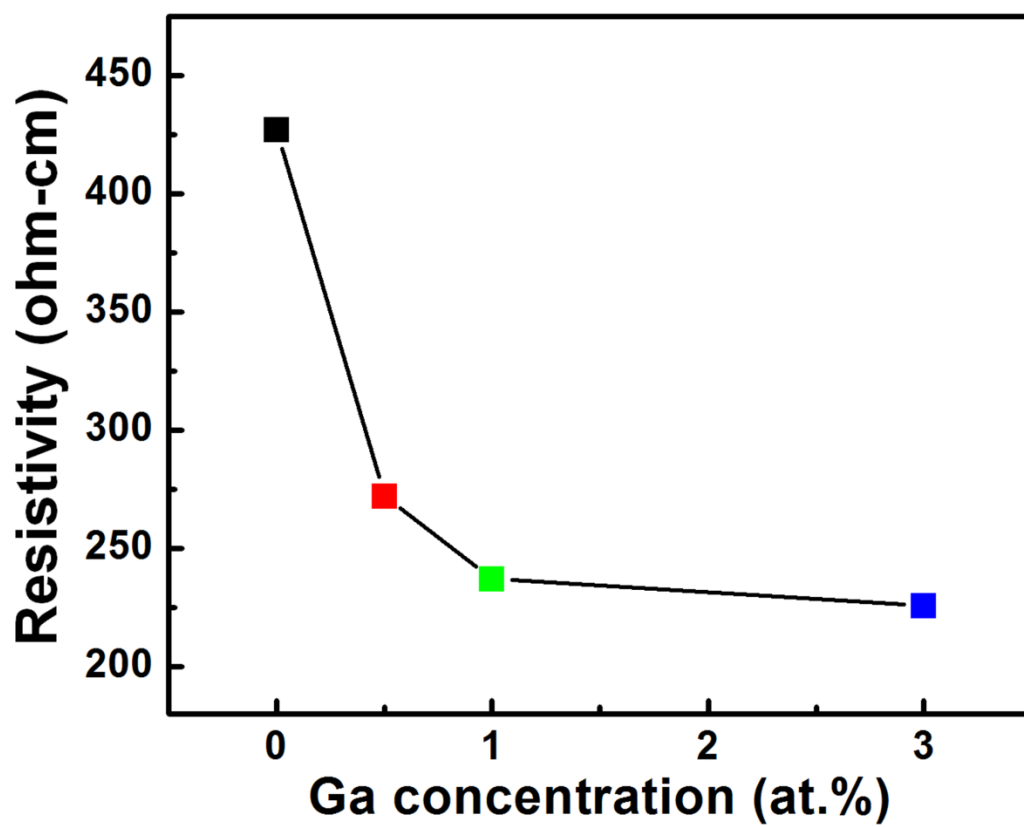


Figure 3.12: Resistivity of the ZnO nanorods with different Ga doping concentrations.

Conclusions

Ga-doped ZnO nanorods with Ga concentrations from 0.5 to 3.0 at.% were grown on glass substrates by the hydrothermal method. The structural, optical, and electrical properties of Ga-doped ZnO nanorods were compared with an undoped sample. The crystal shape of the tips of the ZnO nanorods changed from pointed and needle-like, to more of a flat hexagon. Dense and vertically well-aligned ZnO nanorods with uniform length were obtained at 3.0 at.% Ga doping. The surface wettability changed from superhydrophilic to less hydrophilic with contact angle of 40.3° . From the XRD analysis, it was confirmed that incorporation of Ga in ZnO promoted the growth direction along the *c*-axis, and both the *a*-axis and *c*-axis lattice constants decreased due to the smaller ionic radius of Ga compared to Zn. The Ga-doped ZnO nanorods notably exhibited increased transmittance and optical band gap energy. The resistivity of the ZnO nanorods decreased as Ga doping concentration increased because of the increase in charge carrier concentration. The lowest electrical resistivity was obtained at the doping concentration of 3.0 at.%.

References

- [1] T. Minami, Transparent conducting oxide semiconductors for transparent electrodes, *Semicond. Sci. Technol.*, **20**, S35–S44, 2005.
- [2] H. Hosono, Recent progress in transparent oxide semiconductors: Materials and device application, *Thin Solid Films*, **515**, 6000–6014, 2007.
- [3] H. Kim, J.S. Horwitz, G.P. Kushto, S.B. Qadri, Z.H. Kafafi, and D.B. Chrisey, Transparent conducting Zr-doped In_2O_3 thin films for organic light-emitting diodes, *Appl. Phys. Lett.*, **78**, 1050–1052, 2001.
- [4] X. Jiang, F.L. Wong, M.K. Fung, and S.T. Lee, Aluminum-doped zinc oxide films as transparent conductive electrode for organic light-emitting devices, *Appl. Phys. Lett.*, **83**, 1875–1877, 2003.
- [5] S. Major and K.L. Chopra, Indium-doped zinc oxide films as transparent electrodes for solar cells, *Sol. Energy Mater.*, **17**, 319–327, 1988.
- [6] V. Bhosle, J.T. Prater, F. Yang, D. Burk, S.R. Forrest, and J. Narayan, Gallium-doped zinc oxide films as transparent electrodes for organic solar cell applications, *J. Appl. Phys.*, **102**, 023501, 2007.
- [7] T. Minami, Substitution of transparent conducting oxide thin films for indium tin oxide transparent electrode applications, *Thin Solid Films*, **516**, 1314–1321, 2008.
- [8] K. Ellmer, Past achievements and future challenges in the development of optically transparent electrodes, *Nature Photon.*, **6**, 12, 809–817, 2012.

- [9] J.-H. Lee and J.-T. Song, Dependence of the electrical and optical properties on the bias voltage for ZnO:Al films deposited by r.f. magnetron sputtering, *Thin Solid Films*, **516**, 1377–1381, 2008.
- [10] Y. Liu, Y. Li, and H. Zeng, ZnO-based transparent conductive thin films: Doping, performance, and processing, *J. Nanomater.*, **2013**, 196521, 2013.
- [11] M. Sibinski, K. Znajdek, S. Walczak, M. Sloma, M. Gorski, and A. Cenian, Comparison of ZnO:Al, ITO and carbon nanotube transparent conductive layers in flexible solar cells applications, *Mater. Sci. Eng. B*, **177**, 1292–1298, 2012.
- [12] S.B. Zhang, S.-H. Wei, and A. Zunger, Intrinsic n-type versus p-type doping asymmetry and the defect physics of ZnO, *Phys. Rev. B*, **63**, 075205, 2001.
- [13] F. Oba, S.R. Nishitani, S. Isotani, H. Adachi, and I. Tanaka, Energetics of native defects in ZnO, *J. Appl. Phys.*, **90**, 824–828, 2001.
- [14] D.C. Look, G.C. Farlow, P. Reunchan, S. Limpijumnong, S.B. Zhang, and K. Nordlund, Evidence for native-defect donors in n-type ZnO, *Phys. Rev. Lett.*, **95**, 225502, 2005.
- [15] F. Oba, M. Choi, A. Togo, and I. Tanaka, Point defects in ZnO: An approach from first principles, *Sci. Technol. Adv. Mater.*, **12**, 034302, 2011.
- [16] C. Lizandara-Pueyo, S. Dilger, M.R. Wagner, M. Gerigk, A. Hoffmann, and S. Polarz, Li-doped ZnO nanorods with single-crystal quality-non-classical crystallization and self-assembly into mesoporous materials, *Cryst. Eng. Comm.*, **16**, 1525–1531, 2014.

- [17] K. Kim, S.Y. Park, K.-H. Lim, C. Shin, J.-M. Myoung, and Y.S. Kim, Low temperature and solution-processed Na-doped zinc oxide transparent thin film transistors with reliable electrical performance using methanol developing and surface engineering, *J. Mater. Chem.*, **22**, 23120, 2012.
- [18] M.K. Gupta, N. Sinha, and B. Kumar, p-type K-doped ZnO nanorods for optoelectronic applications, *J. Appl. Phys.*, **90**, 083532, 2011.
- [19] C.X. Xu, X.W. Sun, X.H. Zhang, L. Ke, and S.J. Chua, Photoluminescent properties of copper-doped zinc oxide nanowires, *Nanotechnology*, **15**, 856–861, 2004.
- [20] O.A. Yildirim, H.E. Unalan, and C. Durucan, Highly efficient room temperature synthesis of silver-doped zinc oxide (ZnO:Ag) nanoparticles: Structural, optical, and photocatalytic properties, *J. Am. Ceram. Soc.*, **96**, 766–773, 2013.
- [21] B. Chavillon, L. Cario, A. Renaud, F. Tessier, F. Chevire, M. Boujtita, Y. Pellegrin, E. Blart, A. Smeigh, L. Hammarstrom, F. Odobel, and S. Jobic, P-type nitrogen-doped ZnO nanoparticles stable under ambient conditions, *J. Am. Chem. Soc.*, **134**, 464–470, 2012.
- [22] D. Yu, L. Hu, S. Qiao, H. Zhang, S.-E.A. Len, L.K. Len, Q. Fu, X. Chen, and K. Sun, Photoluminescence study of novel phosphorus-doped ZnO nanotetrapods synthesized by chemical vapour deposition, *J. Phys. D: Appl. Phys.*, **42**, 055110, 2009.
- [23] W. Lee, M.-C. Jeong, and J.-M. Myoung, Optical characteristics of arsenic-doped ZnO nanowires, *Appl. Phys. Lett.*, **85**, 6167–6169, 2004.

- [24] F.X. Xiu, Z. Yang, L.J. Mandalapu, D.T. Zhao, and J.L. Liu, Photoluminescence study of Sb-doped p-type ZnO films by molecular-beam epitaxy, *Appl. Phys. Lett.*, **87**, 252102, 2005.
- [25] A.B. Djurisic and Y.H. Leung, Optical properties of ZnO nanostructures, *Small*, **2**, 944–961, 2006.
- [26] C. Lee, K. Lim, and J. Song, Highly textured ZnO thin films doped with indium prepared by the pyrosol method, *Sol. Energ. Mat. Sol. Cells*, **43**, 37–45, 1996.
- [27] J.K. Kim, S.J. Yun, J.M. Lee, and J.W. Lim, Effect of rf-power density on the resistivity of Ga-doped ZnO film deposited by rf-magnetron sputter deposition technique, *Curr. Appl. Phys.*, **10**, S451-S454, 2010.
- [28] J.A. Sans, J.F. Sanchez-Royo, A. Segura, G. Tobias, and E. Canadell, Chemical effects on the optical band-gap of heavily doped ZnO: M_{III} ($M = \text{Al, Ga, In}$): An investigation by means of photoelectron spectroscopy, optical measurements under pressure, and band structure calculations, *Phys. Rev. B*, **79**, 195105, 2009.
- [29] J.L. Zhao, X.W. Sun, H. Ryu, and Y.B. Moon, Thermally stable transparent conducting and highly infrared reflective Ga-doped ZnO thin films by metal organic chemical vapor deposition, *Opt. Mater.*, **33**, 768–772, 2011.
- [30] G.-D. Yuan, W.-J. Zhang, J.-S. Jie, X. Fan, J.-X. Tang, I. Shafiq, Z.-Z. Ye, C.-S. Lee, and S.-T. Lee, Tunable n-type conductivity and transport properties of Ga-doped ZnO nanowire arrays, *Adv. Mater.*, **20**, 168–173, 2008.

- [31] K. Saito, Y. Hiratsuka, A. Omata, H. Makino, S. Kishimoto, T. Yamamoto, N. Horiuchi, and H. Hirayama, Atomic layer deposition and characterization of Ga-doped ZnO thin films, *Superlattice. Microst.*, **42**, 172–175, 2007.
- [32] Y.Y. Kim, B.H. Kong, and H.K. Cho, Vertically arrayed Ga-doped ZnO nanorods grown by magnetron sputtering: The effect of Ga contents and microstructural evaluation, *J. Cryst. Growth*, **330**, 17–21, 2011.
- [33] S.M. Park, T. Ikegami, and K. Ebihara, Effects of substrate temperature on the properties of Ga-doped ZnO by pulsed laser deposition, *Thin Solid Films*, **513**, 90–94, 2006.
- [34] H.J. Ko, Y.F. Chen, S.K. Hong, H. Wensch, T. Yao, and D.C. Look, Ga-doped ZnO films grown on GaN templates by plasma-assisted molecular-beam epitaxy, *Appl. Phys. Lett.*, **77**, 3761–3763, 2000.
- [35] R.T. Ginting, C.C. Yap, M. Yahaya, and M.M. Salleh, Solution-processed Ga-doped ZnO nanorod arrays as electron acceptors in organic solar cells, *ACS Appl. Mater. Interfaces*, **6**, 5308–5318, 2014.
- [36] D.-T. Phan and G.-S. Chung, Effects of defects in Ga-doped ZnO nanorods formed by a hydrothermal method on CO sensing properties, *Sens. Actuators, B*, **187**, 191–197, 2013.
- [37] H. Wang, S. Baek, J. Song, J. Lee, and S. Lim, Microstructural and optical characteristics of solution-grown Ga-doped ZnO nanorod arrays, *Nanotechnology*, **19**, 075607, 2008.

- [38] S.S. Kim and B.-T. Lee, Effects of oxygen pressure on the growth of pulsed laser deposited ZnO films on Si(0 0 1), *Thin Solid Films*, **446**, 307–312, 2004.
- [39] C. Pacholski, A. Kornowski, and H. Weller, Self-assembly of ZnO: From nanodots to nanorods, *Angew. Chem. Int. Ed.*, **41**, 1181–1191, 2002.
- [40] W.I. Park, D.H. Kim, S.-W. Jung, and G.-C. Yi, Metal organic vapor-phase epitaxial growth of vertically well-aligned ZnO nanorods, *Appl. Phys. Lett.*, **80**, 4232–4234, 2002.
- [41] R. Romero, D. Leinen, E.A. Dalchiele, J.R. Ramos-Barrado, and F. Martin, The effects of zinc acetate and zinc chloride precursors on the preferred crystalline orientation of ZnO and Al-doped ZnO thin films obtained by spray pyrolysis, *Thin Solid Films*, **515**, 1942–1949, 2006.
- [42] M. Benhaliliba, C.E. Benouis, M.S. Aida, F. Yakuphanoglu, and J.A. Sanchez, Indium and aluminium-doped ZnO thin films deposited onto FTO substrates: Nanostructure, optical, photoluminescence and electrical properties, *J. Sol-Gel Sci. Technol.*, **55**, 335–342, 2010.
- [43] R.B. Heller, J. McGannon, and A.H. Weber, Precision determination of the lattice constants of zinc oxide, *J. Appl. Phys.*, **21**, 1283–1284, 1950.
- [44] D. Singh and Y.P. Varshni, Debye temperatures for hexagonal crystals, *Phys. Rev. B*, **24**, 4340–4347, 1981.
- [45] M.S. Kim, K.G. Yim, S. Kim, G. Nam, D.-Y. Lee, J.S. Kim, J.S. Kim, and J.-Y. Leem, Growth and characterization of indium-doped zinc oxide thin films prepared by sol-gel method, *Acta Phys. Pol. A*, **121**, 217–220, 2012.

- [46] A.I. Rahachou and I.V. Zozoulenko, Light propagation in nanorod arrays, *J. Opt. A: Pure Appl. Opt.*, **9**, 265–270, 2007.
- [47] E. Burstein, Anomalous optical absorption limit in InSb, *Phys. Rev.*, **93**, 632–633, 1954.
- [48] T.S. Moss, The interpretation of the properties of indium antimonide, *Proc. Phys. Soc. B*, **67**, 775–782, 1954.
- [49] A.D. Trolino, E.M. Bauer, G. Scavia, and C. Veroli, Blueshift of optical band gap in *c*-axis oriented and conducting Al-doped ZnO thin films, *J. Appl. Phys.*, **105**, 113109, 2009.

CHAPTER FOUR

MULTIPLE STACKED ZINC OXIDE NANOFLOWERS GROWN ON PLASTIC

Introduction

Since both the shape and size of nanostructures can influence the resultant properties, there have been numerous reports focused on engineered nanostructures including nanorods (or nanowires), nanotubes, nanosheets, nanoflowers, and nanospheres grown by changing growth conditions [1–11]. Among the diverse range of ZnO nanostructures, nanoflowers have the particular advantages of a high surface area to volume ratio and a short conduction path for electrons to transport. These features are highly preferred for bio-device, display, sensor, and solar cell applications [12–16]. In addition, ZnO nanoflowers have superhydrophobic surfaces, which are very favorable characteristics for self-cleaning applications.

There are two principal synthetic approaches that yield ZnO nanoflowers: a vapor-phase method and a solution-phase method. The vapor-phase method produces high-quality ZnO nanoflowers under well-controlled high vacuum conditions. However, it is not an appropriate technology for flexible electronics on plastic substrates because of the high growth temperatures (400–600 °C) [17,18]. Conversely, the solution-phase method has been widely used as an alternative technique because of the simpler equipment, more environmentally-friendly chemicals, larger capacity growth vessels, and lower-cost. More importantly, the solution-phase method can be performed at low temperatures (100–200 °C), permitting the use of a variety of substrate materials.

To-date, ZnO nanoflowers have mostly been synthesized in the form of nanopowders without a substrate [19–22]. ZnO nanoflowers grown on substrates have only been single-stacks due to the low surface energy and low roughness of the various template layers, which conventionally are grown on substrates before the growth of the ZnO nanostructures [23–25]. There are no reports on the growth of multiple-stacks of ZnO nanoflowers on plastic substrates because of the general lack of a method that can simultaneously provide a large enough surface energy and appropriate roughness of the template layers. Therefore, it is necessary to develop an effective growth method to fabricate multiple-stack high-density ZnO nanoflowers on plastic substrates that permit high electron transport capacity with a high dielectric constant while maintaining a high surface area to volume ratio.

In this work, multiple-stack high-density ZnO nanoflowers/nanorods were successfully grown on plastic substrates using a hydrothermal method at temperatures below 150 °C. The multiple-stack high-density ZnO nanoflowers were obtained using an atmospheric pressure plasma jet (APPJ) treatment of the seed layers. Several advantages are expected from the plasma treatment on the plastic substrates: (i) the surface wettability of the seed layers changes from hydrophobic to hydrophilic, resulting in higher surface energies for the growth of high-density ZnO nanoflowers, (ii) the nucleation sites increase due to the increased surface roughness caused by the plasma etching, and (iii) there is no thermal damage to the plastic substrate from the plasma treatment due to its low temperature weakly-ionized discharge.

Experimental Details

Synthesis of ZnO Seed Layers

Polyethylene naphthalate (PEN) substrates were cleaned ultrasonically in a mixed solution of isopropanol, ethanol, and deionized (DI) water (volume ratios of 1:1:1) for 10 min. ZnO seed layers were then deposited on PEN substrates using a sol-gel spin-coating method. Specifically, the sol-gel solution was prepared by dissolving zinc acetate dihydrate in a mixture of 2-methoxyethanol and monoethanolamine, used as a solvent and stabilizer, respectively. The molar ratio of the monoethanolamine to zinc acetate dihydrate was held constant at 1.0; the concentration of zinc acetate was 0.5 M. The resultant solution was stirred at 60 °C for 2 h to yield a clear and homogenous solution, and then it was aged at room temperature for 24 h. The solution was drop-cast onto PEN substrates and spin-coated in two steps. The first and second coating steps were at 1000 rpm for 10 sec and then at 3000 rpm for 20 sec, respectively. After spin-coating, the ZnO seed layers were heated at 100 °C for 20 min in order to evaporate the solvent and remove the organic residue. The ZnO seed layers then were treated with the APPJ array for 30 sec. This procedure, from the coating to the plasma treatment, was repeated four times.

Atmospheric Pressure Plasma Jet System

In order to treat a wide area with the plasma, a plasma jet array device comprised of seven quartz tubes was fabricated. The complete APPJ system is described schematically in Figure 4.1a. The array was formed from a central quartz tube surrounded by six tubes, each having an inner diameter of 1 mm and an outer diameter of 2 mm such

that the center-to-center distance between two adjacent quartz tubes was 2.3 mm. Copper tape, 6 mm in width, was used as a powered electrode and was wrapped around each quartz tube 10 mm from the end of the tube. A layer of carbon tape was applied onto the copper electrode of each tube, and the seven tubes were combined using copper tape, which was functioned as a powered electrode. An indium tin oxide (ITO)-coated glass plate of 0.8 mm thickness was placed 10 mm from the end of the quartz tubes with the glass side facing the plasma jets and served as a ground electrode. High purity (99.997%) helium gas was used as the discharge gas with a flow of 5 standard liters per minute. When a sinusoidal voltage with peak value of 6 kV and frequency of 32 kHz was applied to the powered electrode, the plasma plume between the plasma jet array device and the glass side of the ITO-coated glass exhibited seven well-collimated plasma plumes as shown in Figure 4.1b. The plasma plumes were well-aligned and parallel to each other under these conditions. The ZnO seed layers grown on the PEN substrate were then positioned onto the ITO-coated glass in preparation for subsequent plasma treatments. When these seven collimated plasma plumes impinged upon the surface of the ZnO seed layers, the plasma plumes formed a uniform plasma layer. The effective area treated by the plasma plumes in this experiment was about $1.3 \times 1.3 \text{ cm}^2$.

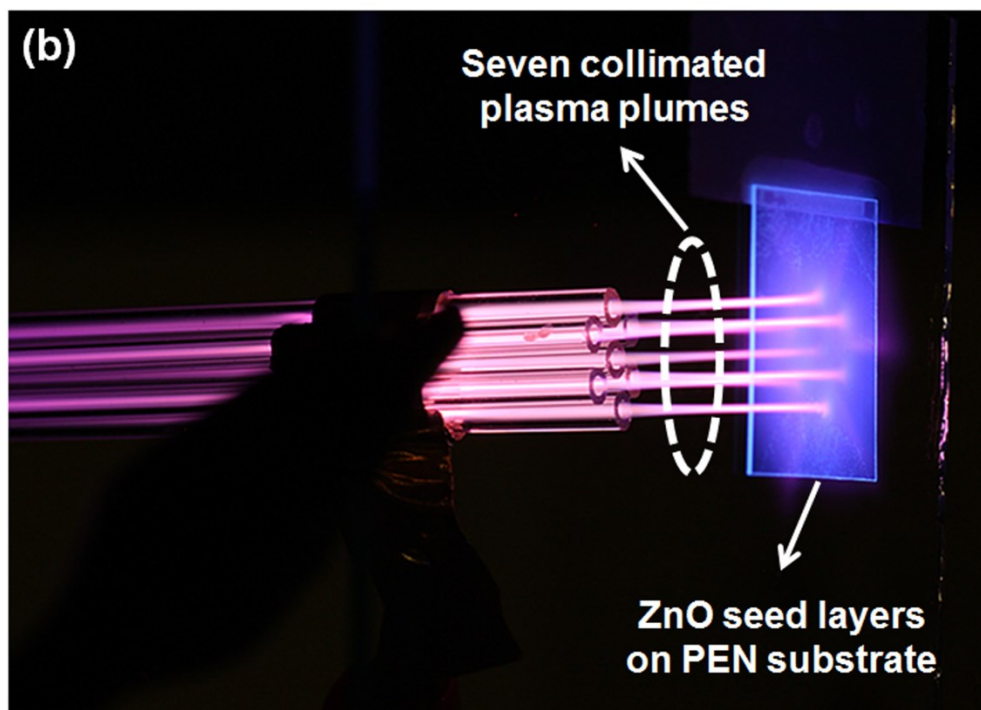
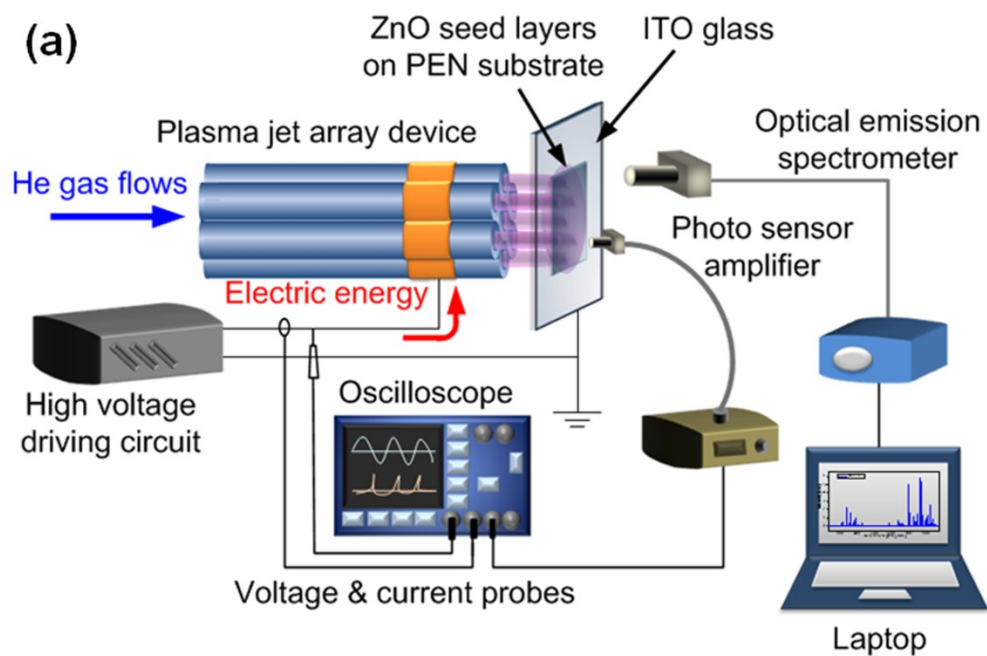


Figure 4.1: (a) Schematic diagram of the APPJ system. (b) Photograph of seven well-collimated plasma plumes between the plasma array and the PEN substrate.

Synthesis of ZnO Nanoflowers/Nanorods

A hydrothermal method was used to grow the ZnO nanoflower/nanorod structures on the as-grown and plasma-treated ZnO seed layers. The samples were transferred into a Teflon-lined autoclave (125 mL) that contained an aqueous solution of 0.05 M zinc nitrate hexahydrate and 0.05 M hexamethylenetetramine. The samples were held in position by a holding structure inside the Teflon-lined autoclave with a height of 2.2 cm from the bottom. The sample and the holding structure were completely submerged in the aqueous solution. The growth temperature was held constant at 150 °C for 10 h. After the reaction, the sample was rinsed thoroughly with DI water and dried with flowing nitrogen gas in order to remove residual salts.

Characterization

The optical emission spectrum of the APPJ array was monitored using a fiber optic spectrometer (Ocean Optics, USB-4000 UV-Vis) in order to identify the reactive species generated by the helium plasma plumes in the ambient air. The wettability of the ZnO seed layers was measured using a contact angle goniometer (KSV, CAM 200) whereas the surface morphology was observed by atomic force microscopy (AFM; Digital Instruments, Dimension 3100) in tapping mode. Field-emission scanning electron microscopy (FE-SEM; Hitachi, S-4800) and transmission electron microscopy (TEM; Hitachi, H-9500) also were used to characterize the morphology and crystal size of ZnO. Prior to the TEM measurement, ZnO nanoflowers/nanorods were dispersed ultrasonically from the PEN substrate in acetone for 30 min and then a few drops of this mixture (ZnO in acetone) were placed on the copper TEM grids and dried for subsequent observation

[26]. The crystallinity and crystal phase of the ZnO nanoflowers/nanorods were analyzed by X-ray diffraction (XRD; Rigaku, ULTIMA IV diffractometer). The optical properties of the ZnO nanoflower/nanorod structures were investigated using Raman spectroscopy (Thermo Scientific, Almega XR) in a backscattering geometry using the 488 nm emission line as an excitation source.

Plasma-Treated ZnO Seed Layers

Figure 4.2 provides the optical emission spectrum of the helium plasma plumes in the ambient air. Various excited species including N_2 , N_2^+ , He, and O were observed. The clear presence of nitrogen and oxygen species in the emission spectrum indicates that many gaseous species from the air participate in the plasma processes even though the plasma jets are produced only from pure helium gas. The reactive oxygen species in the plasma volume can effectively change the surface properties of materials which it comes in contact with.

In order to investigate the interfacial properties of the ZnO following the plasma treatment, the wettability of the ZnO seed layers was characterized by contact angle measurements. The water contact angle was found to decrease from 103.0° to 40.5° , as shown in Figure 4.3, which indicates that the surface wettability of the ZnO seed layers was changed from a hydrophobic to hydrophilic nature by the plasma. Surface energies of the ZnO seed layers were obtained using the Girifalco-Good-Fowkes-Young equation [27]:

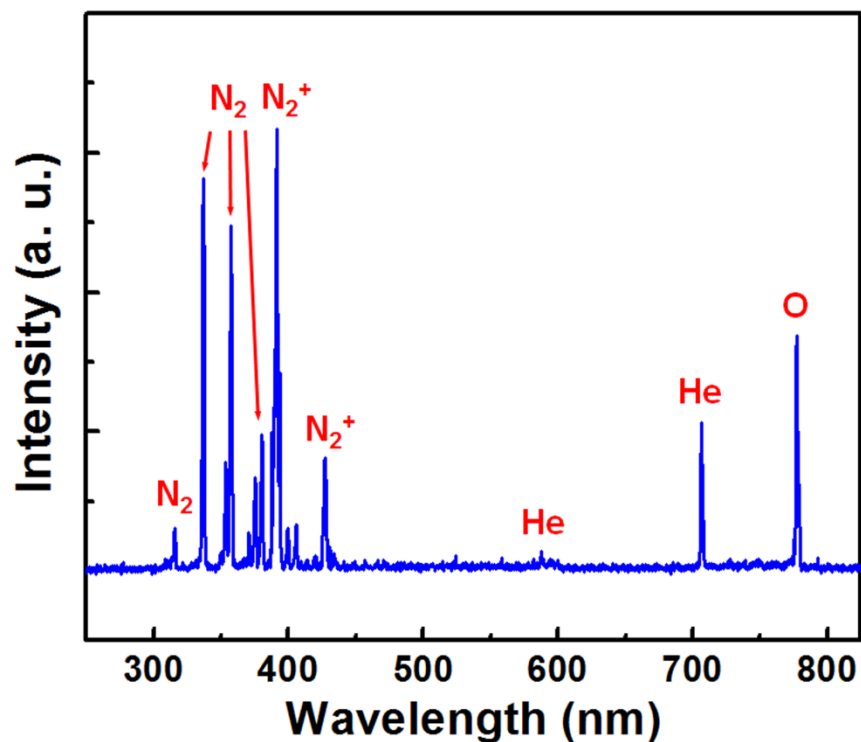


Figure 4.2: Optical emission spectrum of the APPJ array, which was monitored using a fiber-optic spectrometer.

$$\gamma_{sv} = \frac{\gamma_{lv}(1 + \cos\theta)^2}{4}$$

Here, γ_{sv} and γ_{lv} are the interfacial surface energies of the solid-vapor and liquid-vapor interfaces, respectively. For γ_{lv} , a surface energy of 72.5 mJ/m² was used for the DI water; whereas, for γ_{sv} the measured value of contact angle θ from the ZnO seed layers was used [28]. The calculated values of the surface energy are summarized in Table 4.1 and reveal that the surface energy of the ZnO seed layers is increased 5.5 times by the plasma treatment.

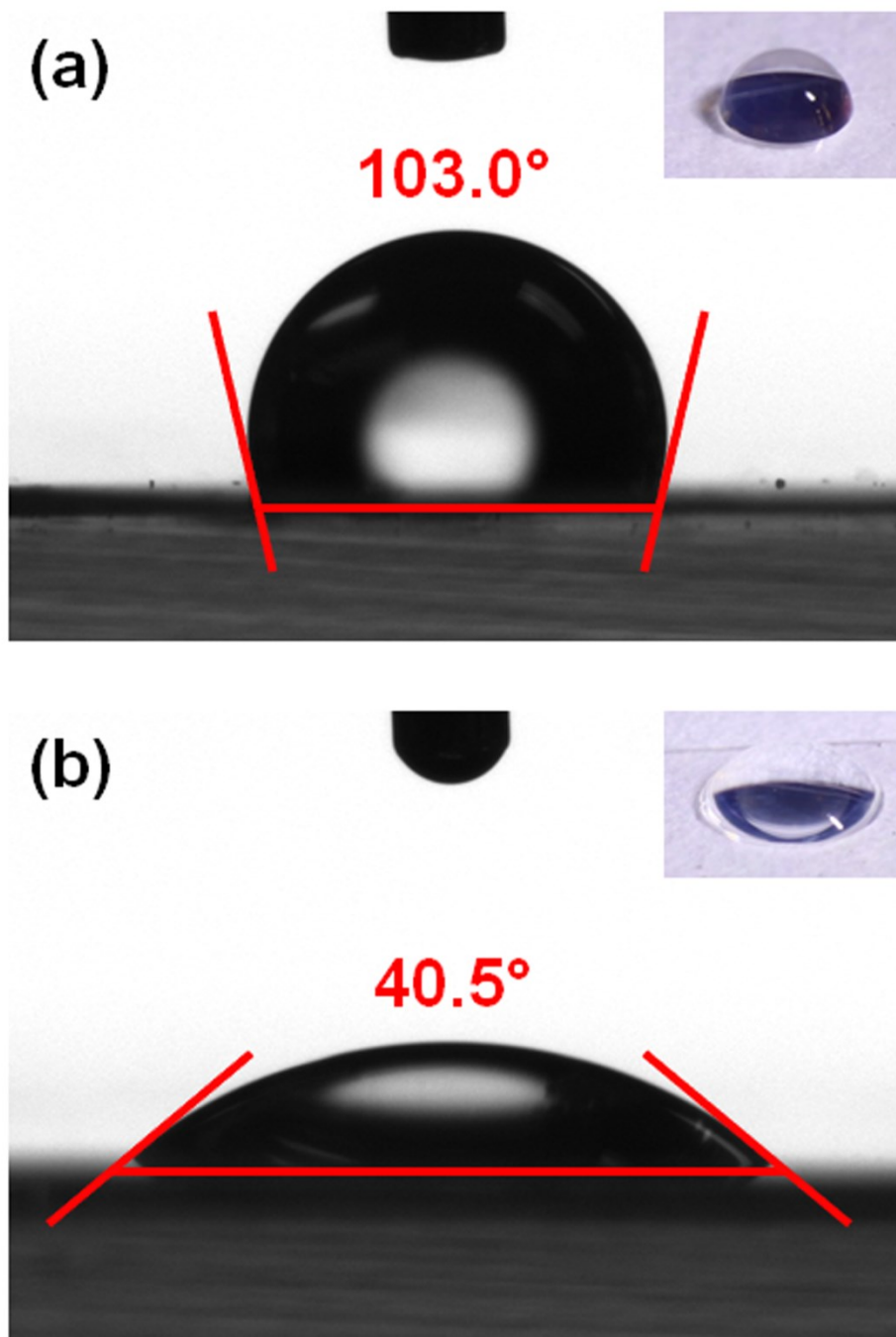


Figure 4.3: Contact angle measurement of the (a) as-grown ZnO seed layers and the (b) plasma-treated ZnO seed layers. Insets show a photograph of a water droplet on each seed layer.

Table 4.1: Contact angle and surface energy of the ZnO seed layers.

Sample	Contact angle (°)	Surface energy (mJ/m ²)
As-grown ZnO seed layers	103.0 ± 0.84	10.89
Plasma-treated ZnO seed layers	40.5 ± 0.24	56.17

The AFM and FE-SEM images of the as-grown and plasma-treated ZnO seed layers are shown in Figure 4.4. It was found that the plasma treatment results in a 10 % increase of the surface roughness of the seed layer from 2.783 nm to 3.063 nm, which can be explained by the known etching effects of plasma [29].

Multiple Stacked ZnO Nanoflowers/Nanorods

Figure 4.5 provides FE-SEM images of the ZnO nanoflowers/nanorods grown on the as-grown ZnO seed layers as well as the plasma-treated ZnO seed layers. ZnO nanoflowers/nanorods consist of a two-layered structure with nanorod arrays on the bottom layer (red rectangles) and nanoflower arrays on the top layer (blue rectangles). The individual nanoflower structure is composed of a number of hexagonal nanorods, which grow radially in many directions. It was also found that the crystal shape of the ZnO nanoflowers/nanorods is barely affected by the plasma treatment.

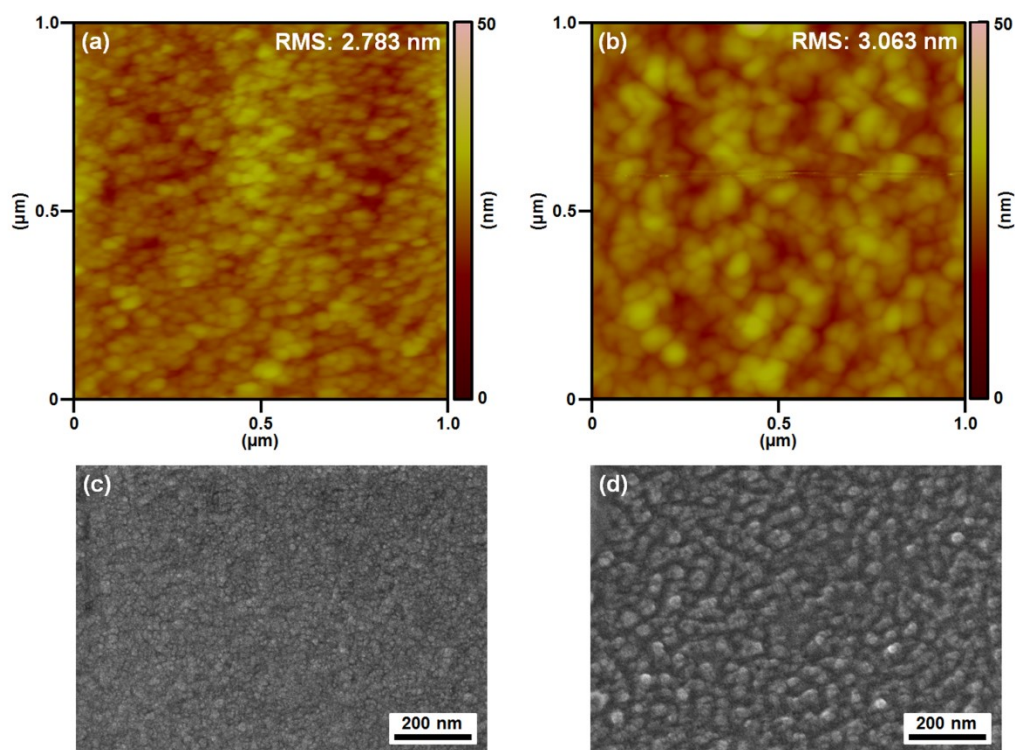


Figure 4.4: AFM images of the (a) as-grown ZnO seed layers with RMS roughness of 2.783 nm and the (b) plasma-treated ZnO seed layers with RMS roughness of 3.063 nm. Top-view FE-SEM images of the (c) as-grown ZnO seed layers and the (d) plasma-treated ZnO seed layers.

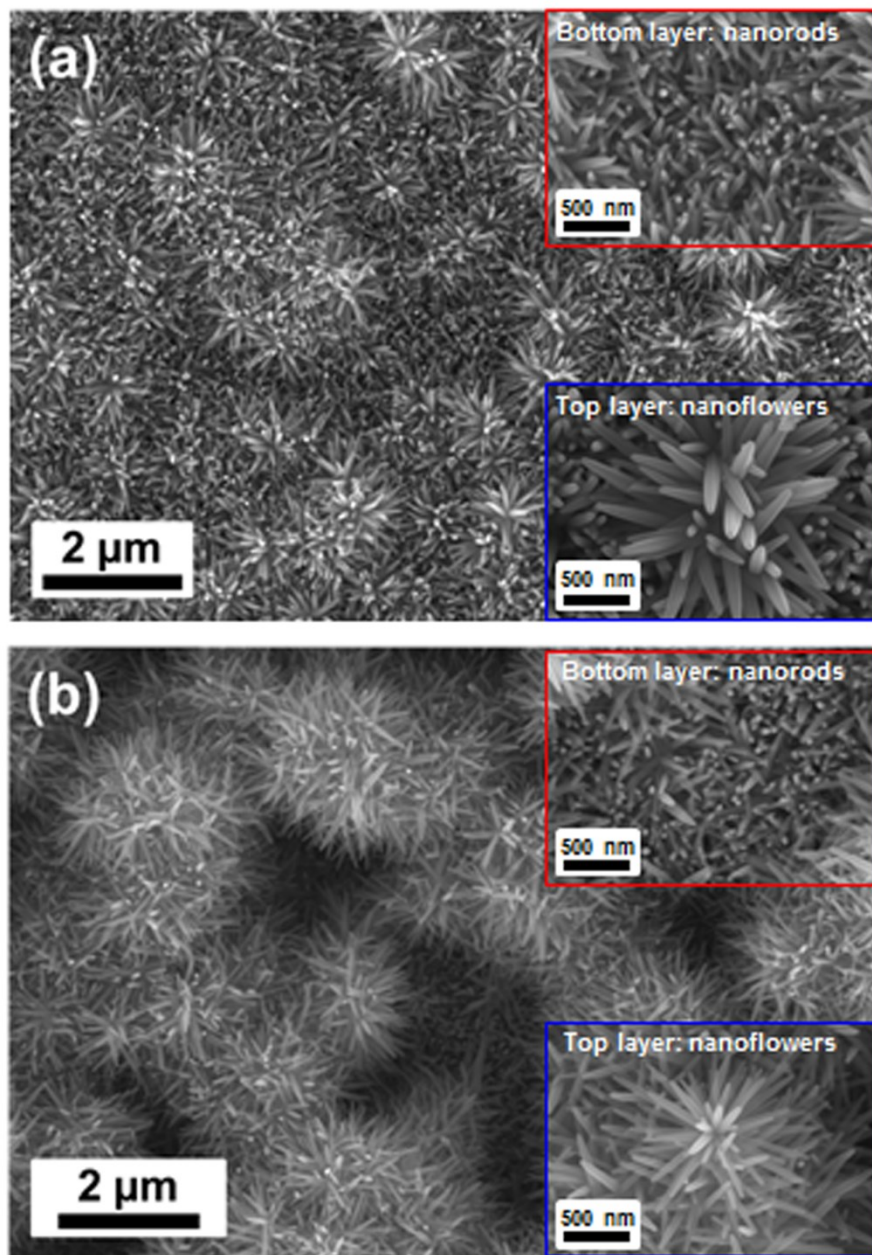


Figure 4.5: Top-view FE-SEM images of the ZnO nanoflower/nanorod structures grown on the (a) as-grown ZnO seed layers and the (b) plasma-treated ZnO seed layers. Insets show high-magnified images of the nanorods on the bottom layer (red rectangles) and nanoflowers on the top layer (blue rectangles).

Figure 4.6a–d shows cross-sectional FE-SEM images of the ZnO nanorod arrays grown on the seed layers. The typical length and diameter of the individual nanorods range from 500–1000 nm and 50–100 nm, respectively. The probability distributions for the length and diameter of the nanorods are shown in Figure 4.6e and f. The dominant length and diameter of the plasma-treated sample were smaller than those of the as-grown sample. The size of the ZnO nanorods was non-uniform due to the growth of some nanorods being hindered by their neighbors which halted subsequent growth. It is noticeable that the height and density of the ZnO nanoflowers/nanorods were significantly increased by the plasma treatment of the ZnO seed layers. As shown in Figure 4.6c and d, multiple-stacks of nanoflowers were grown continuously on the nanorods in the plasma-treated sample, whereas only one stack of nanoflowers was grown on the nanorods in the as-grown sample.

The increase in roughness of the seed layers following the plasma treatment induces the growth of ZnO nanorods with rougher surface morphology. This implies that there are a number of nanorods whose height is greater than those of adjacent nanorods. For the growth of the ZnO nanoflowers following the growth of the nanorods, nucleation sites are formed on the surface of the ZnO nanorods with greater height because of the radial growth preference of the nanorods, which is less spatially hindered. After the formation of the nucleation sites, many ZnO nanorods grow radially, which finally results in the ZnO nanoflower structure. Furthermore, the increased surface energy of the plasma-treated ZnO seed layers results in multiple-stacks of nanoflowers because the nucleation probability is increased in order to reduce the entire system energy.

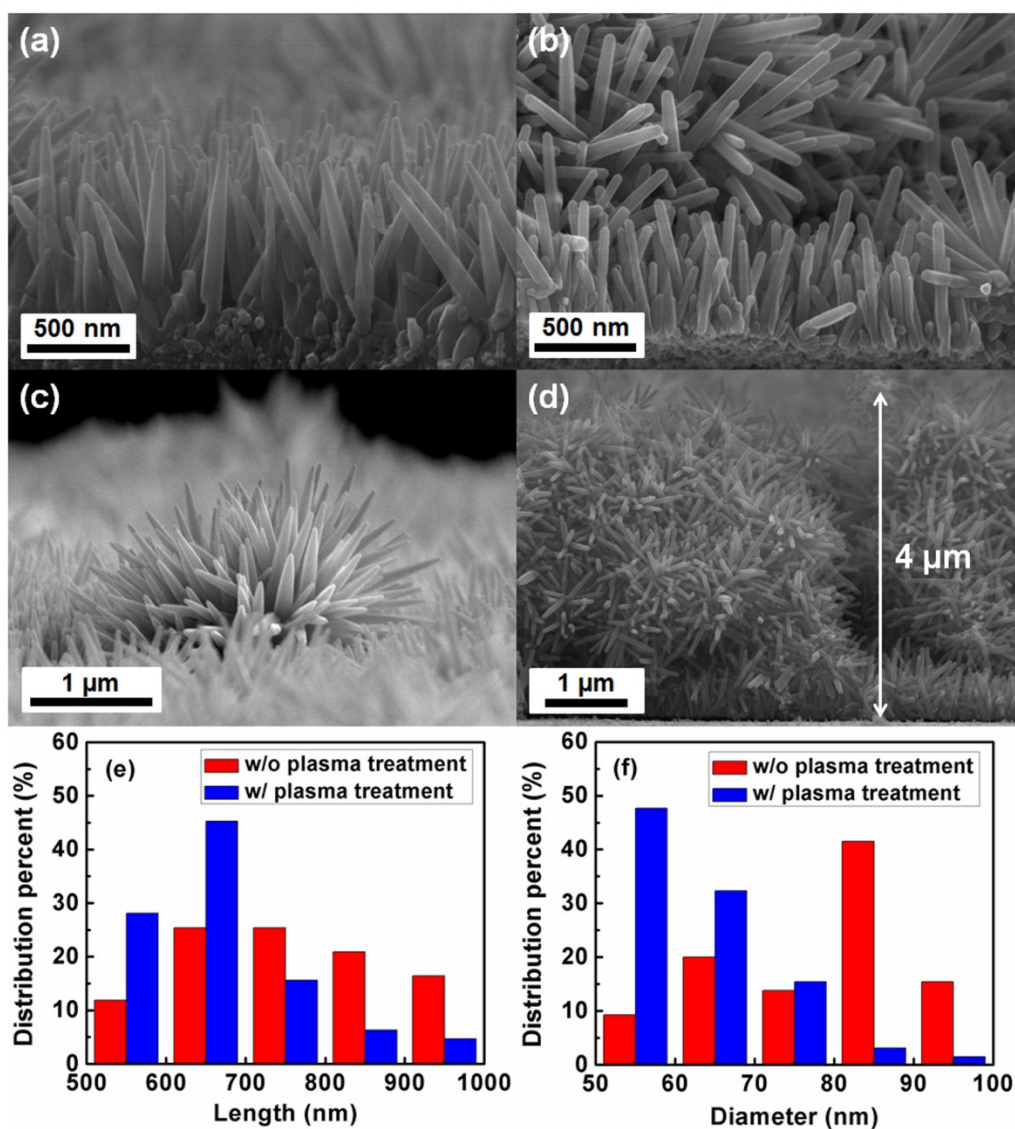


Figure 4.6: Cross-sectional FE-SEM images of ZnO nanoflowers/nanorods grown on the (a and c) as-grown ZnO seed layers and the (b and d) plasma-treated ZnO seed layers. Histograms of the (e) length and (f) diameter distribution of the nanorods.

Figure 4.7 provides the XRD patterns associated with the ZnO nanoflower/nanorod structures grown on the as-grown and plasma-treated ZnO seed layers. Various ZnO diffraction peaks were observed including those at 31.8° , 34.46° , 36.28° , 47.58° , 62.88° , 68.02° , and 69.2° , which correspond to the ZnO crystallographic reflections (100), (002), (101), (102), (103), (112), and (201), respectively. Except for the peaks from the PEN substrate, which are marked with an asterisk in Figure 4.7, all of the peaks in the obtained spectrum are well-indexed to the hexagonal ZnO phase (JCPDS card No. 36-1451) indicating that the ZnO nanoflower/nanorod structures crystallize in the typical wurtzite structure [30]. It was observed that the intensity of the ZnO(002) diffraction peak is higher compared to that of the standard ZnO diffraction pattern, which indicates a *c*-axis preferred growth direction. In addition, the intensity of the ZnO diffraction peaks increased following plasma treatment of the ZnO seed layers because of the increased density of the ZnO nanoflowers. This is consistent with the SEM results shown in Figure 4.6c and d.

TEM analysis was carried out for further structural characterization. Figure 4.8a and b provide low-magnification TEM images of the ZnO nanorods. The typical diameters of these ZnO nanorods are in the range of 30–90 nm, which is consistent with those observed using the FE-SEM and shown in Figure 4.6a and b. However, the length (200–500 nm) of the ZnO nanorods was not consistent with FE-SEM results. This is likely due to the fact that the ZnO nanorods were mechanically broken when peeled away from the substrates by sonication. High-resolution TEM (HRTEM) images of a ZnO nanorod are shown in Figure 4.8c and d. The lattice spacing was measured to be 0.26 nm,

which closely matches the literature value for the distance between (0001) planes in the ZnO crystal and indicates that the ZnO nanorods preferentially grow along the c -axis [0001] direction. Fast Fourier transform (FFT) patterns (insets of Figure 4.8c and d), performed on individual nanorods, prove that the ZnO nanorods are single crystalline.

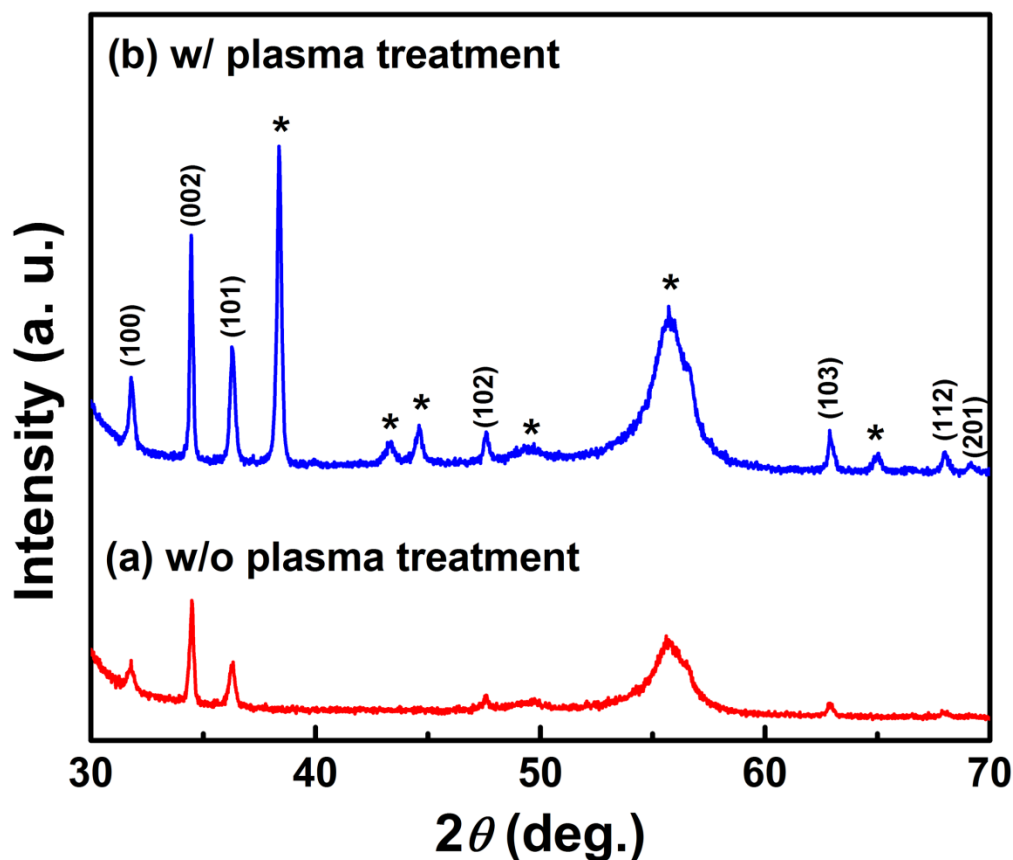


Figure 4.7: XRD patterns of the ZnO nanoflower/nanorod structures grown on the (a) as-grown ZnO seed layers and the (b) plasma-treated ZnO seed layers. The peaks denoted with an asterisk are attributed to the PEN substrates.

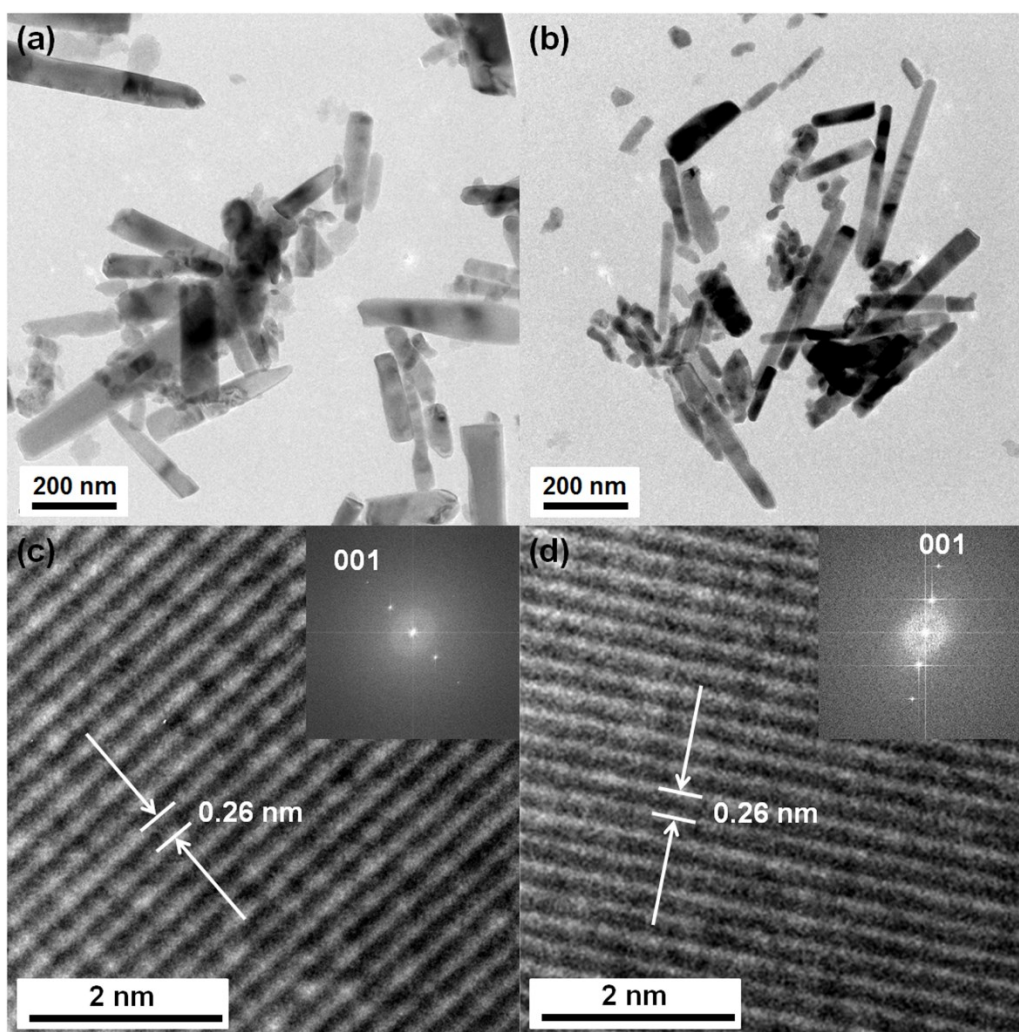


Figure 4.8: Low-magnification TEM images of the ZnO nanoflower/nanorod structures grown on the (a) as-grown ZnO seed layers and the (b) plasma-treated ZnO seed layers. HRTEM images of the ZnO nanoflower/nanorod structures grown on the (c) as-grown ZnO seed layers and the (d) plasma-treated ZnO seed layers with their corresponding FFT patterns (inset).

The optical properties of the ZnO nanoflowers/nanorods were studied using spontaneous Raman scattering. ZnO has a wurtzite crystal structure and belongs to the C_{6v}^4 space group with two formula units per primitive cell, where all the atoms occupy the C_{3v} symmetry. Near the center of the Brillouin zone, group theory predicts the existence of the following phonon modes: $\Gamma=A_1+2B_1+E_1+2E_2$. The B_1 modes are forbidden, while the A_1 , E_1 , and E_2 modes are (Raman) allowed. Additionally, the A_1 and E_1 are also infrared active and split into two components, *i.e.*, transverse optical (TO) and longitudinal optical (LO) components [31]. The frequencies of Raman active phonon modes in ZnO are as follows: E_2 (low) = 101 cm^{-1} , E_2 (high) = 437 cm^{-1} , E_1 (TO) = 407 cm^{-1} , E_1 (LO) = 583 cm^{-1} , A_1 (TO) = 380 cm^{-1} , and A_1 (LO) = 574 cm^{-1} [32]. Figure 4.9 shows the Raman scattering spectra of the bare PEN substrate (Figure 4.9a) and the ZnO nanoflowers/nanorods (Figure 4.9b and c). A sharp and strong peak at 438 cm^{-1} is assigned to the E_2 (high frequency) optical phonon mode of the ZnO, which is characteristic of the hexagonal wurtzite phase of ZnO [33]. Two weak peaks located at 333 cm^{-1} and 382 cm^{-1} are assigned to the E_2 (high)- E_2 (low) (second-order multiple-phonon scattering) and A_1 (TO) mode, respectively. The multiple-phonon scattering is likely due to the quantum confinement effects in the ZnO nanostructures [34]. The absence of the E_1 (LO) mode at 583 cm^{-1} indicates that the ZnO nanoflowers/nanorods are of good crystal quality because the E_1 (LO) mode is associated with structural defects (zinc interstitials or oxygen vacancies) and impurities in the ZnO crystal.

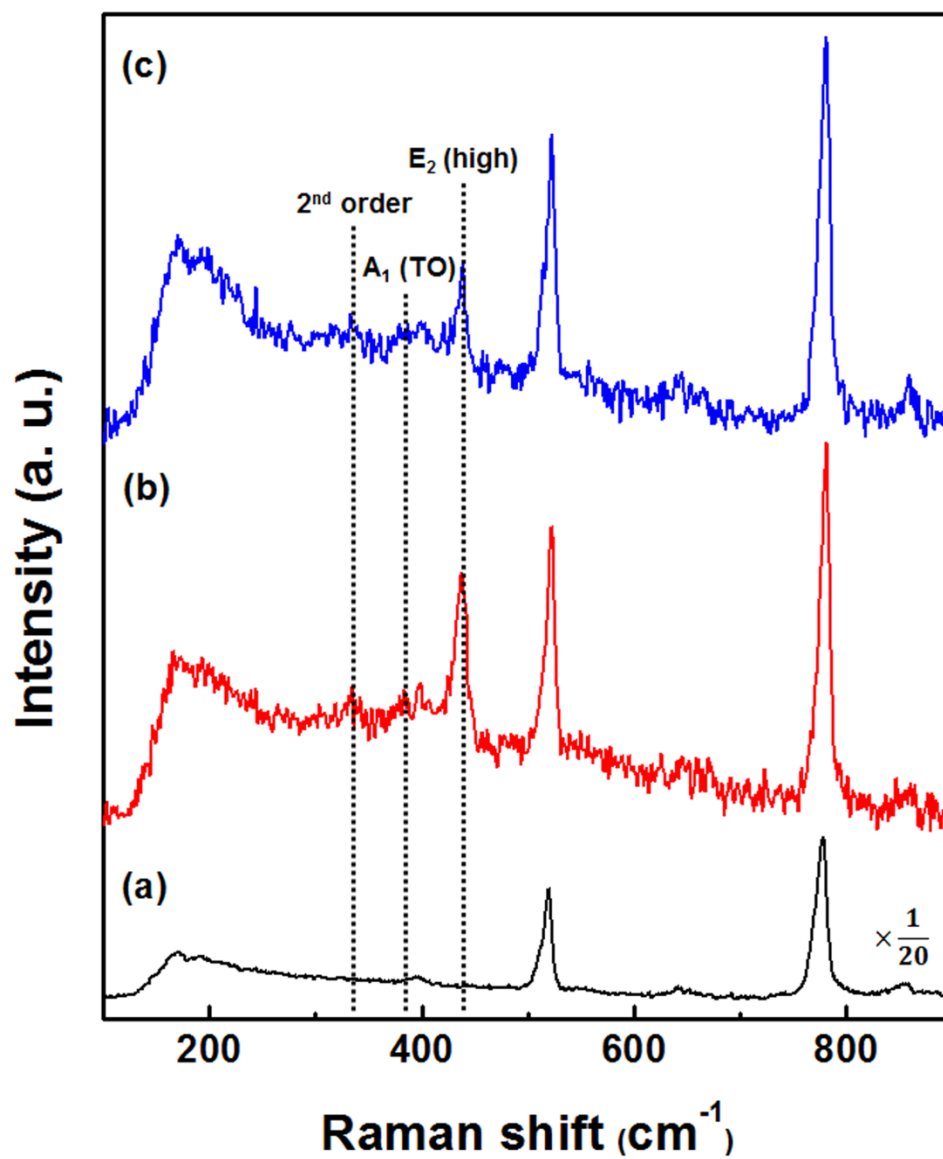


Figure 4.9: Raman scattering spectra of the (a) bare PEN substrate and the ZnO nanoflowers/nanorods grown on the (b) as-grown ZnO seed layers and the (c) plasma-treated ZnO seed layers.

Conclusions

Demonstrated in this work is the synthesis of ZnO nanoflowers/nanorods on PEN substrate using a hydrothermal method. Spin-deposited ZnO seed layers were treated with an APPJ array before the growth of the ZnO nanoflowers/nanorods. The resultant individual nanoflowers were composed of a number of hexagonal nanorods, which grew radially in many directions. The plasma treatment induced a significant increase in the height and density of the ZnO nanoflowers/nanorods because the plasma effectively increased the surface energy and roughness of the seed layers while barely affecting the crystal shape and phase of the ZnO nanoflowers/nanorods. The XRD and Raman scattering measurements indicated that the ZnO nanoflowers/nanorods have good crystal quality with a hexagonal wurtzite structure. The multiple-stack high-density ZnO nanoflowers/nanorods were easily obtained through a simple plasma treatment of the seed layers during conventional hydrothermal synthetic procedures, making APPJ treatment a very useful enhancement for flexible electronics on plastic substrates.

References

- [1] S. Baruah and J. Dutta, Effect of seeded substrates on hydrothermally grown ZnO nanorods, *J. Sol-Gel Sci. Technol.*, **50**, 456–464, 2009.
- [2] O. Lupan and T. Pauporte, Hydrothermal treatment for the marked structural and optical quality improvement of ZnO nanowire arrays deposited on lightweight flexible substrates, *J. Cryst. Growth*, **312**, 2454–2458, 2010.
- [3] A. Hu, F. Wu, J. Liu, J. Jiang, R. Ding, X. Li, C. Cheng, Z. Zhu, and X. Huang, Density- and adhesion-controlled ZnO nanorod arrays on the ITO flexible substrates and their electrochromic performance, *J. Alloys Compd.*, **507**, 261–266, 2010.
- [4] J. Han, F. Fan, C. Xu, S. Lin, M. Wei, X. Duan, and Z.L. Wang, ZnO nanotube-based dye-sensitized solar cell and its application in self-powered devices, *Nanotechnology*, **21**, 405203, 2010.
- [5] H. Sun, M. Luo, W. Weng, K. Cheng, P. Du, G. Shen, and G. Han, Room-temperature preparation of ZnO nanosheets grown on Si substrates by a seed-layer assisted solution route, *Nanotechnology*, **19**, 125603, 2008.
- [6] C. Wu, X. Qiao, L. Luo, and H. Li, Synthesis of ZnO flowers and their photoluminescence properties, *Mater. Res. Bull.*, **43**, 1883–1891, 2008.
- [7] H.F. Garces, A.E. Espinal, and S.L. Suib, Tunable shape microwave synthesis of zinc oxide nanospheres and their desulfurization performance compared with nanorods and platelet-like morphologies for the removal of hydrogen sulfide, *J. Phys. Chem. C*, **116**, 8465–8474, 2012.

- [8] J. Bao, M.A. Zimmler, and F. Capasso, Broadband ZnO single-nanowire light-emitting diode, *Nano Lett.*, **6**, 1719–1722, 2006.
- [9] Z.L. Wang and J. Song, Piezoelectric nanogenerators based on zinc oxide nanowire arrays, *Science*, **312**, 242–246, 2006.
- [10] J. Zhang, S. Wang, M. Xu, Y. Wang, B. Zhu, S. Zhang, W. Huang, and S. Wu, Hierarchically porous ZnO architectures for gas sensor application, *Cryst. Growth Des.*, **9**, 3532–3537, 2009.
- [11] M. Law, L.E. Greene, J.C. Johnson, R. Saykally, and P. Yang, Nanowire dye-sensitized solar cells, *Nat. Mater.*, **4**, 455–459, 2005.
- [12] Y. Lei, X. Liu, X. Yan, Y. Song, Z. Kang, N. Luo, and Y. Zhang, Multicenter uric acid biosensor based on tetrapod-shaped ZnO nanostructures, *J. Nanosci. Nanotechnol.*, **12**, 513–518, 2012.
- [13] Y.J. Kim, J. Yoo, B.H. Kwon, Y.J. Hong, C.H. Lee, and G.C. Yi, Position-controlled ZnO nanoflower arrays grown on glass substrates for electron emitter application, *Nanotechnology*, **19**, 315202, 2008.
- [14] X.J. Wang, W. Wang, and Y.L. Liu, Enhanced acetone sensing performance of Au nanoparticles functionalized flower-like ZnO, *Sens. Actuators, B*, **168**, 39–45, 2012.
- [15] L. Han, D. Wang, J. Cui, L. Chen, T. Jiang, and Y. Lin, Study on formaldehyde gas-sensing of In₂O₃-sensitized ZnO nanoflowers under visible light irradiation at room temperature, *J. Mater. Chem.*, **22**, 12915–12920, 2012.

- [16] C.Y. Jiang, X.W. Sun, G.Q. Lo, D.L. Kwong, and J.X. Wang, Improved dye-sensitized solar cells with a ZnO-nanoflower photoanode, *Appl. Phys. Lett.*, **90**, 263501, 2007.
- [17] X.H. Sun, S. Lam, T.K. Sham, F. Heigl, A. Jürgensen, and N.B. Wong, Synthesis and synchrotron light-induced luminescence of ZnO nanostructures: Nanowires, nanoneedles, nanoflowers, and tubular whiskers, *J. Phys. Chem. B*, **109**, 3120–3125, 2005.
- [18] N. Zhang, R. Yi, R. Shi, G. Gao, G. Chen, and X. Liu, Novel rose-like ZnO nanoflowers synthesized by chemical vapor deposition, *Mater. Lett.*, **63**, 496–499, 2009.
- [19] R. Wahab, S.G. Ansari, Y.S. Kim, H.K. Seo, G.S. Kim, G. Khang, and H.S. Shin, Low temperature solution synthesis and characterization of ZnO nano-flowers, *Mater. Res. Bull.*, **42**, 1640–1648, 2007.
- [20] S.H. Jung, E. Oh, K.H. Lee, Y. Yang, C.G. Park, W. Park, and S.H. Jeong, Sonochemical preparation of shape-selective ZnO nanostructures, *Cryst. Growth Des.*, **8**, 265–269, 2008.
- [21] P. Rai, J.N. Jo, I.H. Lee, and Y.T. Yu, Fabrication of flower-like ZnO microstructures from ZnO nanorods and their photoluminescence properties, *Mater. Chem. Phys.*, **124**, 406–412, 2010.
- [22] Z. Fang, K. Tang, G. Shen, D. Chen, R. Kong, and S. Lei, Self-assembled ZnO 3D flowerlike nanostructures, *Mater. Lett.*, **60**, 2530–2533, 2006.

- [23] H. Gao, F. Yan, J. Li, Y. Zeng, and J. Wang, Synthesis and characterization of ZnO nanorods and nanoflowers grown on GaN-based LED epiwafer using a solution deposition method, *J. Phys. D: Appl. Phys.*, **40**, 3654–3659, 2007.
- [24] F. Barka-Bouaifel, B. Sieber, N. Bezzi, J. Benner, P. Roussel, L. Boussekey, S. Szunerits, and R. Boukherroub, Synthesis and photocatalytic activity of iodine-doped ZnO nanoflowers, *J. Mater. Chem.*, **21**, 10982–10989, 2011.
- [25] Y.J. Kim, Hadiyawarman, A. Yoon, M. Kim, G.C. Yi, and C. Liu, Hydrothermally grown ZnO nanostructures on few-layer graphene sheets, *Nanotechnology*, **22**, 245603, 2011.
- [26] Q. Ahsanulhaq, J.H. Kim, and Y.B. Hahn, Etch-free selective area growth of well-aligned ZnO nanorod arrays by economical polymer mask for large-area solar cell applications, *Sol. Energy Mater. Sol. Cells*, **98**, 476–481, 2012.
- [27] R.E. Johnson and R.H. Dettre, in *wettability*, J.C. Berg. Ed., Marcel Dekker, New York, 1993.
- [28] H. Kobayashi, Surface tension of poly(fluoroalkylsilsesquioxane)s, *Macromol. Chem. Phys.*, **194**, 2569–2577, 1993.
- [29] J.Y. Kim, J.W. Cho, and S.H. Kim, The characteristic of the ZnO nanowire morphology grown by the hydrothermal method on various surface-treated seed layers, *Mater. Lett.*, **65**, 1161–1164, 2011.

- [30] M.S. Kim, K.G. Yim, H.Y. Choi, M.Y. Cho, G.S. Kim, S.M. Jeon, D.Y. Lee, J.S. Kim, J.S. Kim, J.S. Son, J.I. Lee, and J.Y. Leem, Thermal annealing effects of MBE-seed-layers on properties of ZnO nanorods grown by hydrothermal method, *J. Cryst. Growth*, **326**, 195–199, 2011.
- [31] J.M. Calleja and M. Cardona, Resonant Raman scattering in ZnO, *Phys. Rev. B*, **16**, 3753–3761, 1977.
- [32] T.C. Damen, S.P.S. Porto, and B. Tell, Raman effect in zinc oxide, *Phys. Rev.*, **142**, 570–574, 1966.
- [33] Y.J. Xing, Z.H. Xi, Z.Q. Xue, X.D. Zhang, J.H. Song, R.M. Wang, J. Xu, Y. Song, S.L. Zhang, and D.P. Yu, Optical properties of the ZnO nanotubes synthesized *via* vapor phase growth, *Appl. Phys. Lett.*, **83**, 1689–1691, 2003.
- [34] V.V. Ursaki, I.M. Tiginyanu, V.V. Zalamai, E.V. Rusu, G.A. Emelchenko, V.M. Masalov, and E.N. Samarov, Multiphonon resonant Raman scattering in ZnO crystals and nanostructured layers, *Phys. Rev. B*, **70**, 155204, 2004.

CHAPTER FIVE

HIGH TEMPERATURE PROCESSED ZINC OXIDE NANORODS GROWN ON MICA

Introduction

The development of optically transparent electronic devices fabricated on mechanically flexible substrates has been the subject of much recent research, in that it represents the next generation electronics technology because of its great potential and functionality to significantly enhance many industries from a commercial perspective. Substantial research has been conducted on developing and analyzing transparent and/or flexible devices, such as thin-film transistors, light emitting diodes, solar cells, supercapacitors, and batteries [1–5]. Metal foil, polyethylene terephthalate (PET), polyethylene naphthalate (PEN), and cellulose nanopaper have commonly been used as the flexible substrate materials [6–10]. However, these substrate materials have some limitations. For example, dye-sensitized solar cells (DSSCs) using opaque metal foil as a substrate material must be illuminated from the back-side of the cell and there are large losses of incident light through the counter electrode and electrolyte before the light reaches the dye attached to the photoanode. This reverse illumination decreases the energy conversion efficiency by 20% compared to the front-side illumination [11,12]. Another consideration is the typical use of thermal annealing processes, which are essential for improving the overall device performance in a variety of applications. Indium tin oxide (ITO) is widely used as transparent electrodes, and the transparency and conductivity of ITO can be improved by a thermal annealing process in excess of 300 °C




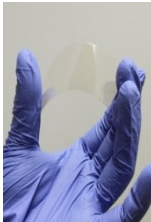
[13–15]. A post-growth annealing process has also been useful for improving the crystal quality of active layers in devices [16–19]. PET, PEN, and cellulose nanopaper are highly flexible and transparent materials but their processing temperatures, 100 °C for PET, 120 °C for PEN, and 200 °C for cellulose nanopaper, prevent their use above these temperatures. The transference of active layers to PET, PEN, or cellulose nanopaper substrates after the annealing process at high temperature is another viable alternative for improving the crystal quality of active layers, though this process is somewhat more complex to undertake [20,21]. Consequently, determining novel substrate materials with high flexibility, transparency, and thermal stability is a critical necessity for developing flexible and transparent applications.

Muscovite mica sheets are chemically inert, flexible, transparent, light-weight, perfectly insulating, and are also stable when exposed to moisture, light, and high temperatures. In addition, they cleave perfectly into very thin pliable sheets whose two principal axes are almost parallel to the cleavage plane, thus providing a sufficiently large sheet of uniform thickness [22]. These outstanding characteristics of mica satisfy the requirements of the substrate material for flexible and transparent applications. The comparison of substrate materials for flexible and/or transparent electronics is summarized in Table 5.1.

In this chapter, ZnO nanorods were grown on flexible and transparent mica substrates using a hydrothermal method depending on several growth conditions, including growth temperatures and concentrations of polyethylenimine (PEI) and ammonium hydroxide. Under elaborately managed growth conditions, vertically well-

aligned ZnO nanorods with high-aspect ratio were successfully grown on mica substrates. Flexible and transparent ZnO nanorod-based DSSCs and piezoelectric nanogenerators (NGs) were fabricated, and the effects of both the growth time and the annealing process on DSSCs and NGs were investigated.

Table 5.1: Comparison of substrate materials for flexible and/or transparent electronics.

Substrate material	Advantage	Disadvantage
Metal foil 	<ul style="list-style-type: none"> ➤ Available for high temperature processing 	<ul style="list-style-type: none"> ➤ Opaque
PET or PEN 	<ul style="list-style-type: none"> ➤ Cheap 	<ul style="list-style-type: none"> ➤ Limited processing temperature (100 °C for PET and 120 °C for PEN)
Cellulose nanopaper 	<ul style="list-style-type: none"> ➤ Eco-friendly 	<ul style="list-style-type: none"> ➤ Limited processing temperature (200 °C)
Mica 	<ul style="list-style-type: none"> ➤ Chemically inert ➤ Light-weight ➤ Perfectly insulating ➤ Stable when exposed to moisture, light, and high temperatures ➤ Available for high temperature processing 	

Experimental Details

Synthesis of ZnO Nanorods on Mica

The mica used as substrates in this research was high quality muscovite mica (Ted Pella Inc.) and the mica sheets were cleaved to ensure high transparency. The cleaved mica substrates were cleaned ultrasonically in acetone for 10 min and then rinsed with deionized (DI) water. ZnO seed layers were deposited on mica substrates using a sol-gel spin-coating method. Specifically, the sol-gel solution was prepared by dissolving 0.005 M zinc acetate dihydrate in ethanol. After spin-coating, the ZnO seed layers were heated at 350 °C for 20 min in order to evaporate the solvent and remove the organic residue. The spin-coating and pre-heating processes were repeated four times. In order to crystallize, the ZnO seed layers were over-heated in an air atmosphere at 500 °C for 30 min.

ZnO nanorods were grown on the ZnO seed layers *via* a hydrothermal process. The samples were transferred into a Teflon jar that contained an aqueous solution of 0.05 M zinc nitrate hexahydrate, 0.05 M hexamethylenetetramine (HMTA), 0.005–0.015 M PEI, and 0.1–0.4 M ammonium hydroxide. To investigate the effect of temperature on the nanorod growth, the growth temperature was varied from 75 to 95 °C. After a reaction for 9 h, the sample was rinsed thoroughly with DI water and air dried naturally.

Fabrication of Dye-Sensitized Solar Cells and Piezoelectric Nanogenerators

ITO film was deposited as a transparent electrode on mica substrate by sputtering for DSSCs and NGs because the ITO electrode on a mica substrate is currently

unavailable commercially. The ZnO nanorod samples grown on ITO were sensitized in a solution of 0.3 mM di-tetrabutylammonium *cis*-bis(isothiocyanato)bis(2,2'-bipyridyl-4,4'-dicarboxylato)ruthenium(II) (N719 dye, Sigma-Aldrich) in ethanol for 24 h. The photoanode was then removed and rinsed with ethanol to remove excess dye adsorbed. A platinum-coated ITO/mica was used as the counter electrode, and the two electrodes were assembled using a 60- μm thick hot-melt sealing foil (Meltonix 1170-60, Solaronix). Silver paste was applied to the external electrodes to reduce contact resistance. The space between the two electrodes was filled with the iodide based electrolyte (Iodolyte AN-50, Solaronix) immediately prior to characterization of the cell performance.

For NGs, a 2- μm thick poly(methyl methacrylate) (PMMA) layer was spin-coated on the ZnO nanorods at the speed of 3000 rpm; the PMMA layer effectively transmits the bending force equally throughout the ZnO nanorods. An ITO-coated mica substrate was then attached on the PMMA-coated surface *via* a curing process at 180 °C that was used as the counter electrode. The size of the effective working area of the NG was 1 \times 1 cm². Schematic diagrams of the fabricated ZnO nanorod-based DSSCs and NGs are shown in Figure 5.1.

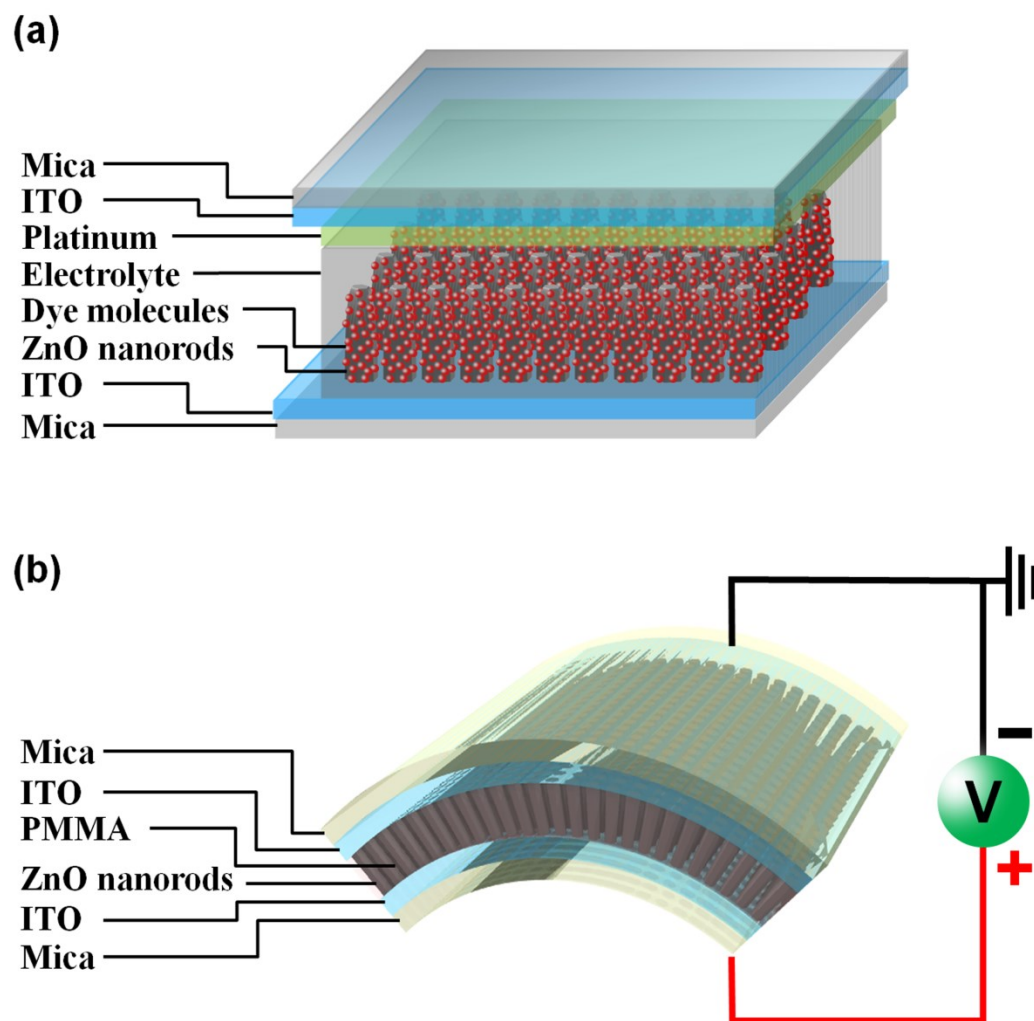


Figure 5.1: Schematic diagrams of the fabricated ZnO nanorod-based devices in this work: (a) DSSCs and (b) piezoelectric NGs.

Characterization

Field-emission scanning electron microscopy (FE-SEM; Hitachi, S-4800) and transmission electron microscopy (TEM; Hitachi, H-9500) were used to characterize the morphology and crystal size of the ZnO nanorods. The crystallinity and crystal phase of the ZnO nanorods were analyzed by X-ray diffraction (XRD; Rigaku, Ultima IV Diffractometer) using Cu-K α radiation ($\lambda=1.5406 \text{ \AA}$). The optical properties of the ZnO nanorods were investigated using Raman spectroscopy (Thermo Scientific, Almega XR) in a backscattering geometry using the 488 nm emission line as an excitation source. The transmittance and sheet resistance of ITO/PET and ITO/mica substrates were compared using an ultraviolet/visible/near-infrared spectrophotometer (Perkin Elmer, Lambda 900) and a four-point probe, respectively. The photovoltaic performance of DSSCs was obtained by measuring the photocurrent-voltage curves. The cell was irradiated using a solar simulator (Newport, 91160 300 W) with an AM 1.5 spectrum distribution calibrated against a NREL reference cell to accurately simulate a full-sun intensity (100 mW/cm^2). The output signal of NGs was recorded *via* a low-noise voltage preamplifier (Stanford Research Systems, SR560) and a low-noise current preamplifier (Stanford Research Systems, SR570). For comparison, all tests were carried out under the same experimental conditions, in which the applied strain was 0.13% at a strain rate of $2.2\% \text{ s}^{-1}$.

Growth Parameters

PEI Concentration

The growth characteristics of ZnO nanorods on mica substrates were investigated because there is as yet no data on these characteristics. However, it is known that the

addition of low-molecular-weight PEI to the solution when using a hydrothermal method results in the creation of ZnO nanorods with a high aspect ratio. The polymer chain of the PEI molecules is effectively adsorbed onto the nonpolar lateral planes of the ZnO nanorod, *i.e.* $(11\bar{2}0)$ (*a*-plane) and $(10\bar{1}0)$ (*m*-plane); as a result, the steric hindrance of the PEI chain inhibits the crystal growth along the faces [23–26]. Consequently, the ZnO nanorods preferentially grow along the *c*-axis $[0001]$ direction resulting in a high aspect ratio. Figure 5.2 shows ZnO nanorods grown at 90 °C with the different concentrations of PEI (0–0.01 M). At low PEI concentrations (0 and 0.005 M), large ZnO nanorods are sparsely formed by the direct agglomeration among adjacent nanorods, which results in the creation of ZnO nanorods of a non-uniform length and diameter. As the PEI concentration increases, the fluctuation in diameter of the ZnO nanorods decreases, resulting in the acquisition of a relatively uniform group of ZnO nanorods with the PEI concentration of 0.01 M. No ZnO nanorods were found growing on a mica substrate with 0.015 M PEI (Figure 5.3), which was due to the excessive PEI chain inhibiting the formation of nucleation sites on the ZnO seed layers.

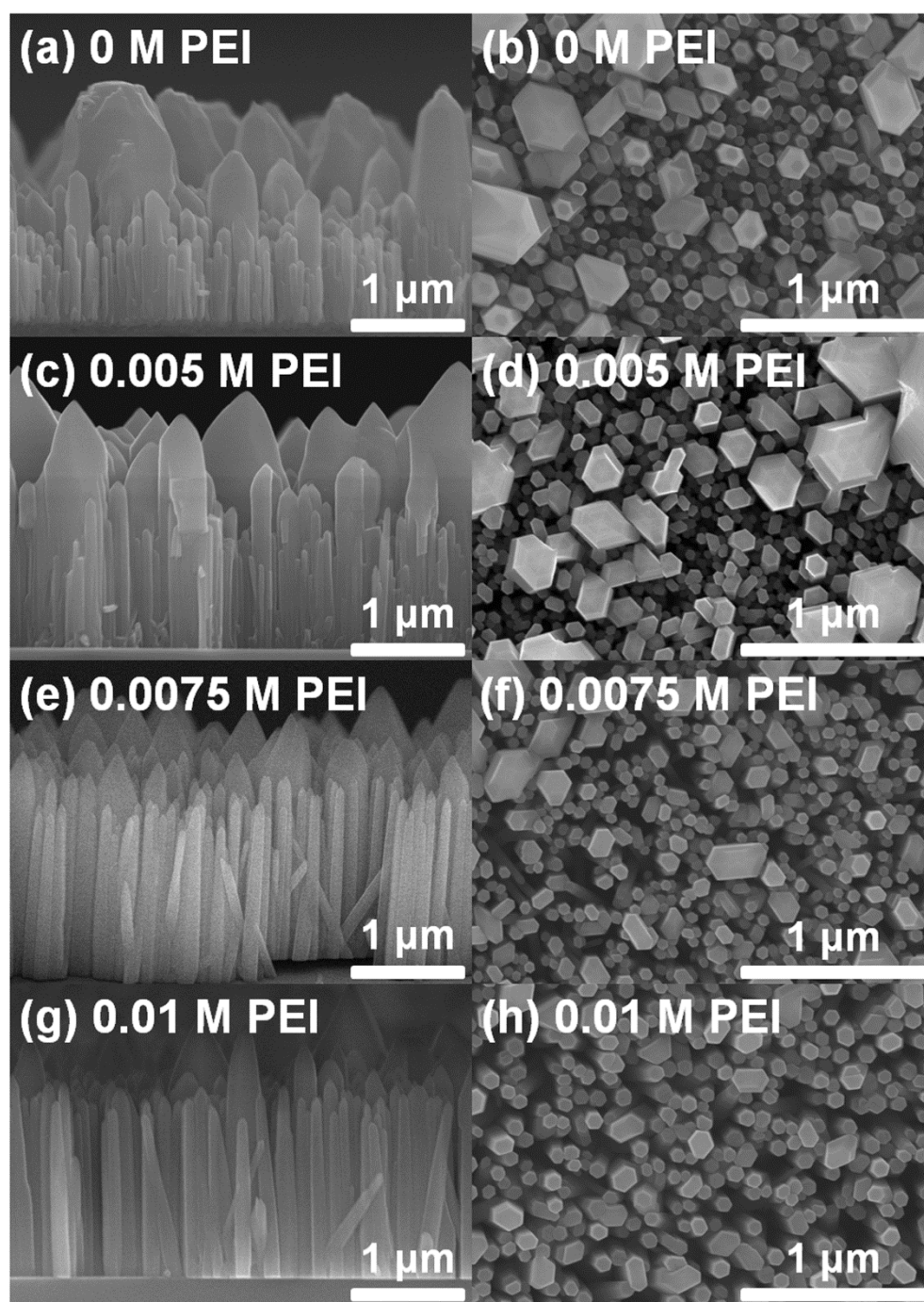


Figure 5.2: FE-SEM images of the ZnO nanorods grown at different PEI concentrations: (a and b) 0 M, (c and d) 0.005 M, (e and f) 0.0075 M, and (g and h) 0.01 M. The growth temperature and time are 90 °C and 9 h, respectively.

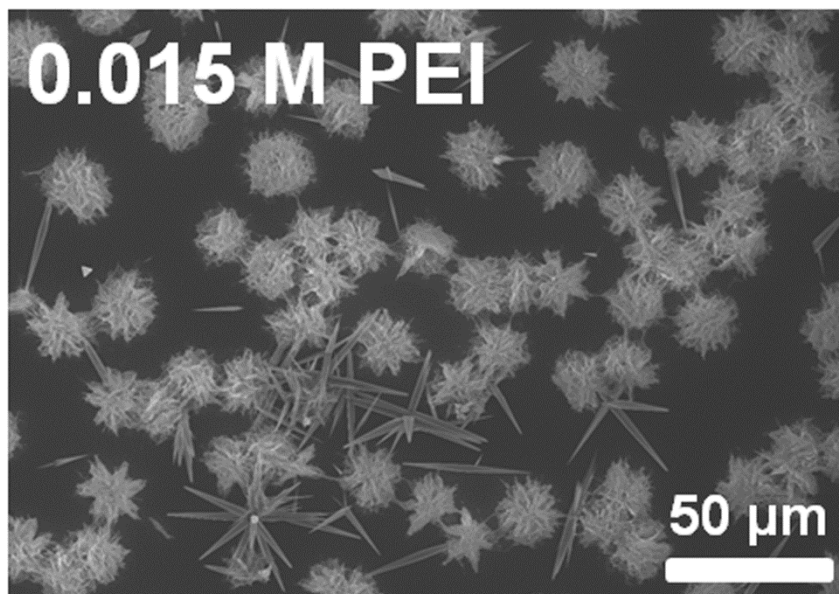


Figure 5.3: FE-SEM image of the ZnO nanorods grown at 0.015 M PEI concentration. The growth temperature and time are 90 °C and 9 h, respectively.

Growth Temperature

Figure 5.4 shows ZnO nanorods grown under temperatures varying from 75 to 95 °C with a constant PEI concentration (0.005 M). The uniformity of the length and diameter of nanorods exhibited an opposite dependence upon growth temperature. Specifically, at the growth temperature of 75 °C, the length of nanorods was non-uniform while the diameter of nanorods was uniform. Conversely, however, the growth at 95 °C exhibited the opposite tendency of a uniform length and a non-uniform diameter. The average length and diameter of nanorods was found to increase with a corresponding increase in growth temperature. At high temperature, the decomposition rate of HMTA was so rapid that the produced OH⁻ ions were large enough to generate a sufficient and

thorough growth of ZnO. Consequently, both the lateral and vertical growth rates largely increased compared to those of the low temperature process [27,28]. In this experiment, the moderate uniformity in length and diameter of nanorods was obtained at the growth temperature of 85 °C.

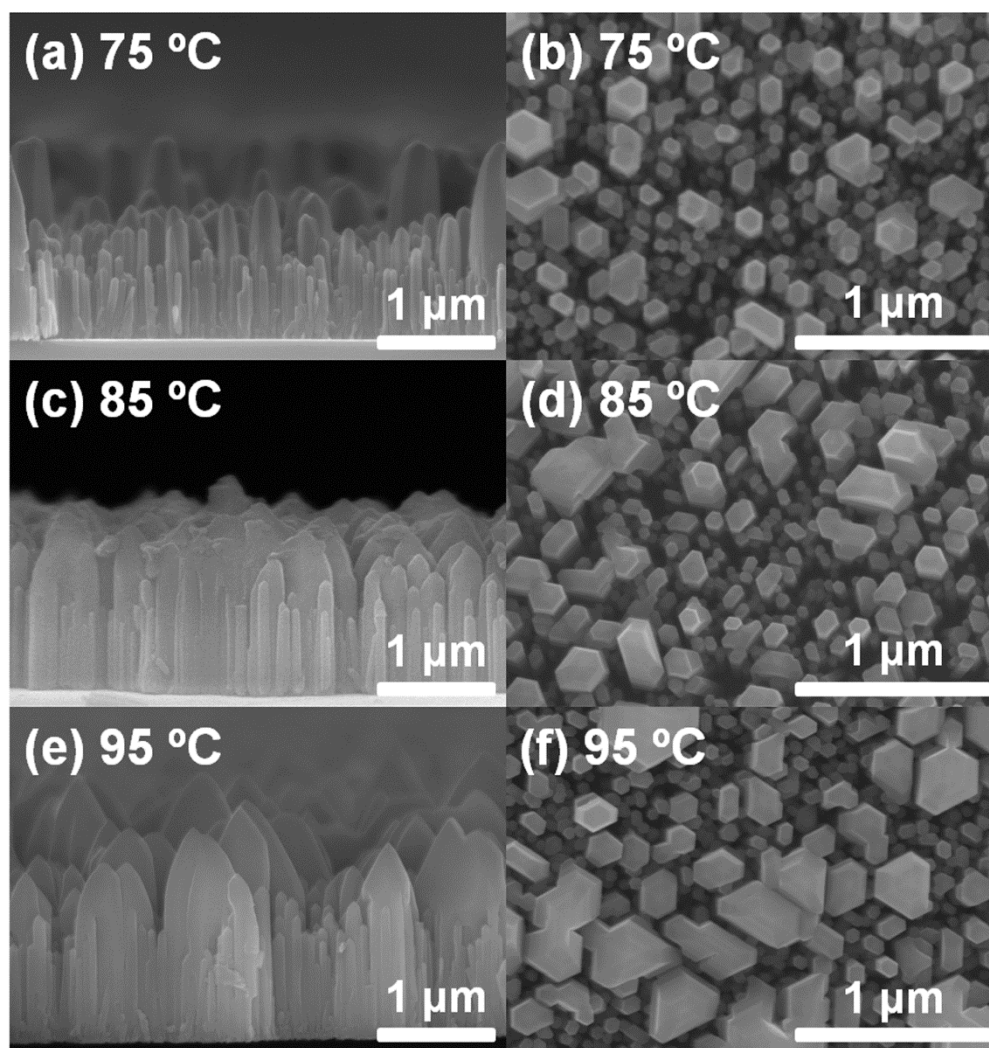


Figure 5.4: FE-SEM images of the ZnO nanorods grown at different temperatures: (a and b) 75 °C, (c and d) 85 °C, and (e and f) 95 °C. The growth time and PEI concentration are 9 h and 0.005 M, respectively.

Ammonium Hydroxide Concentration

In a hydrothermal method, a ZnO crystal is also formed into white precipitates in the bulk solution through a homogeneous nucleation because of a high degree of supersaturation with respect to ZnO or Zn(OH)₂ in the reaction system. The homogeneous nucleation can be suppressed effectively with the introduction of ammonium hydroxide into the reaction solution. The coordination of ammonia to zinc ion results in complexes based on the following reaction: $\text{Zn}^{2+} + n\text{NH}_3 \leftrightarrow \text{Zn}(\text{NH}_3)_n^{2+}$, where $n = 1, 2, 3$, or 4. These complexes also serve as a buffer for Zn^{2+} and continuously supply Zn^{2+} while lowering the degree of supersaturation in the reaction mixture [24,27]. Moreover, the degree of supersaturation has less effect on the crystal growth rate of nanorods on the seeded substrate compared to the homogeneous nucleation [29]. Therefore, introducing ammonium hydroxide into the reaction mixture can suppress the homogeneous nucleation and thus reduce ZnO precipitates in the bulk solution while maintaining moderate growth rate of ZnO nanorods on the seeded substrate.

In order to investigate the effects of ammonium hydroxide on the size of ZnO nanorods grown on mica substrates, ZnO nanorods were grown at varying ammonium hydroxide concentrations from 0.1 M to 0.25 M with a constant PEI concentration (0.005 M) and growth temperature (85 °C). The average length and diameter of nanorods increased with a corresponding increase in the concentrations of ammonium hydroxide (Figures 5.4 and 5.5). However, at an ammonium hydroxide concentration over 0.25 M, the growth of ZnO nanorods did not entirely cover the surface of the mica substrate because of a very low degree of supersaturation and of a deviation of the suitable pH

range for the growth of ZnO nanorods [30]. Specifically, the direct agglomeration among the adjacent nanorods became severe with an excess of ammonium hydroxide beyond 0.2 M. As previously stated, a higher ammonium hydroxide concentration within the moderate pH ranges provides more zinc ions for the growth of ZnO nanorods on the seeded substrates while suppressing the homogeneous nucleation. Consequently, a larger PEI polymer chain is necessary to ensure the inhibition of crystal growth along the lateral planes and a preferential growth of ZnO in the direction of the c -axis [0001]. In this experiment, an insufficiency of PEI over the 0.2 M ammonium hydroxide is expected. Therefore, to grow ZnO nanorods with a high aspect ratio, the lateral growth must be effectively inhibited, which requires controlling the growth conditions of temperature and the concentrations of both PEI and ammonium hydroxide.

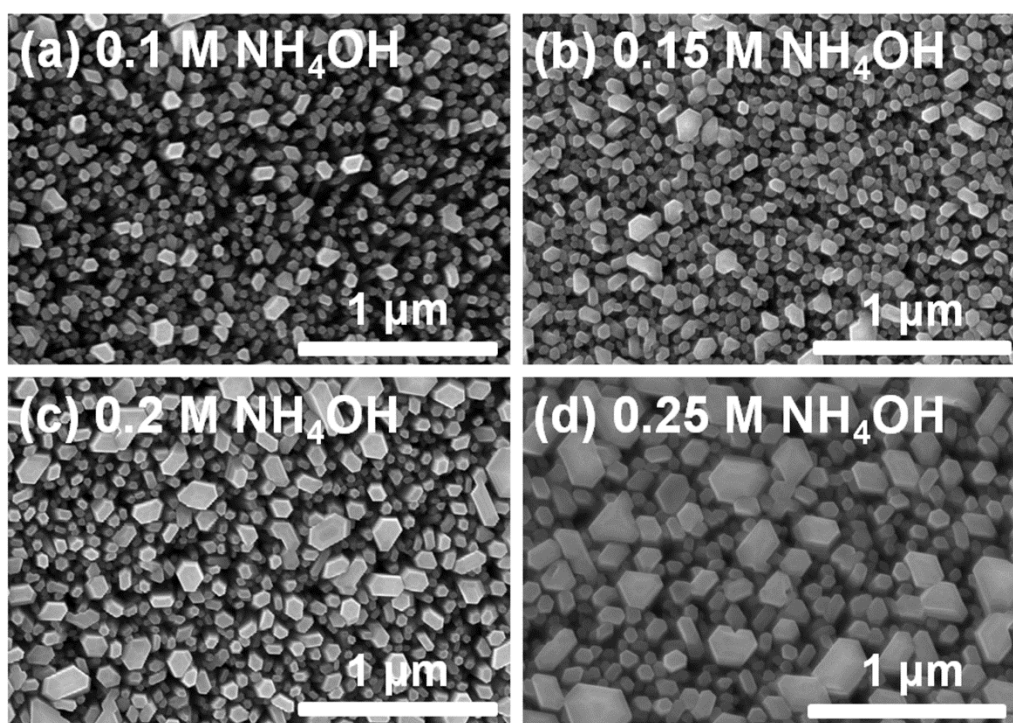


Figure 5.5: FE-SEM images of the ZnO nanorods grown at different ammonium hydroxide concentrations: (a) 0.1 M, (b) 0.15 M, (c) 0.2 M, and (d) 0.25 M. The growth temperature and concentration of PEI are 85 °C and 0.005 M, respectively.

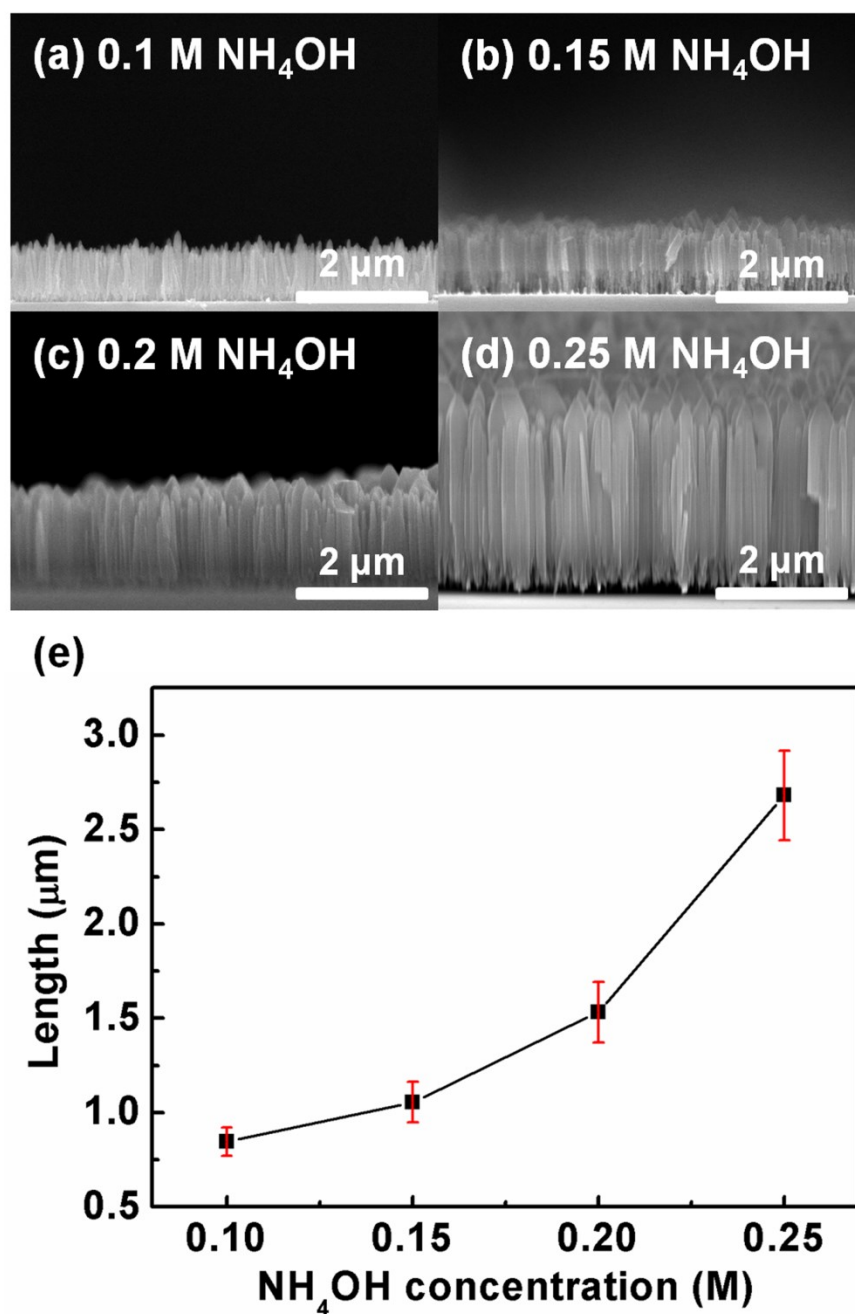


Figure 5.6: Cross-sectional FE-SEM images of the ZnO nanorods grown at different ammonium hydroxide concentrations: (a) 0.1 M, (b) 0.15 M, (c) 0.2 M, and (d) 0.25 M. The growth temperature and PEI concentration are 85 °C and 0.005 M, respectively. (e) Average length of the nanorods as a function of ammonium hydroxide concentration.

Optimal Growth Condition

The coupled use of PEI and ammonium hydroxide was most successful in growing vertically well-aligned ZnO nanorods on mica substrates under 0.01 M PEI and 0.4 M ammonium hydroxide at 85 °C for 9 h (Figure 5.7a and b). The average length and diameter of nanorods were about 5 μm and 170 nm, respectively. TEM analysis was carried out for further structural characterization. Prior to the TEM measurement, ZnO nanorods were dispersed ultrasonically from the mica substrate in acetone for 30 min, and then a few drops of this mixture (ZnO in acetone) were placed on the copper TEM grids and dried for subsequent observation. A low-magnification TEM image of the ZnO nanorod is shown in Figure 5.7c. The inconsistency in the length (1.25 μm) of the nanorod compared to FE-SEM result is because the ZnO nanorods were mechanically broken when peeled away from the substrate by sonication. A high-resolution TEM (HRTEM) image of the ZnO nanorod is shown in Figure 5.7d. The measurement of the lattice spacing is 0.26 nm, which is a close approximation of the literature value for the distance between (0001) planes in the ZnO crystal, indicating that the ZnO nanorods preferentially grow along direction of the *c*-axis [0001] [31–33]. Fast Fourier transform (FFT) pattern (Figure 5.7d, inset), performed on individual nanorod, showed the single crystalline of the ZnO nanorods with the hexagonal wurtzite phase growing in the [0001] direction. In addition, no increase in the length of nanorods over the 18 h-growth (Figure 5.8) was observed because of a complete depletion of the zinc source in solution.

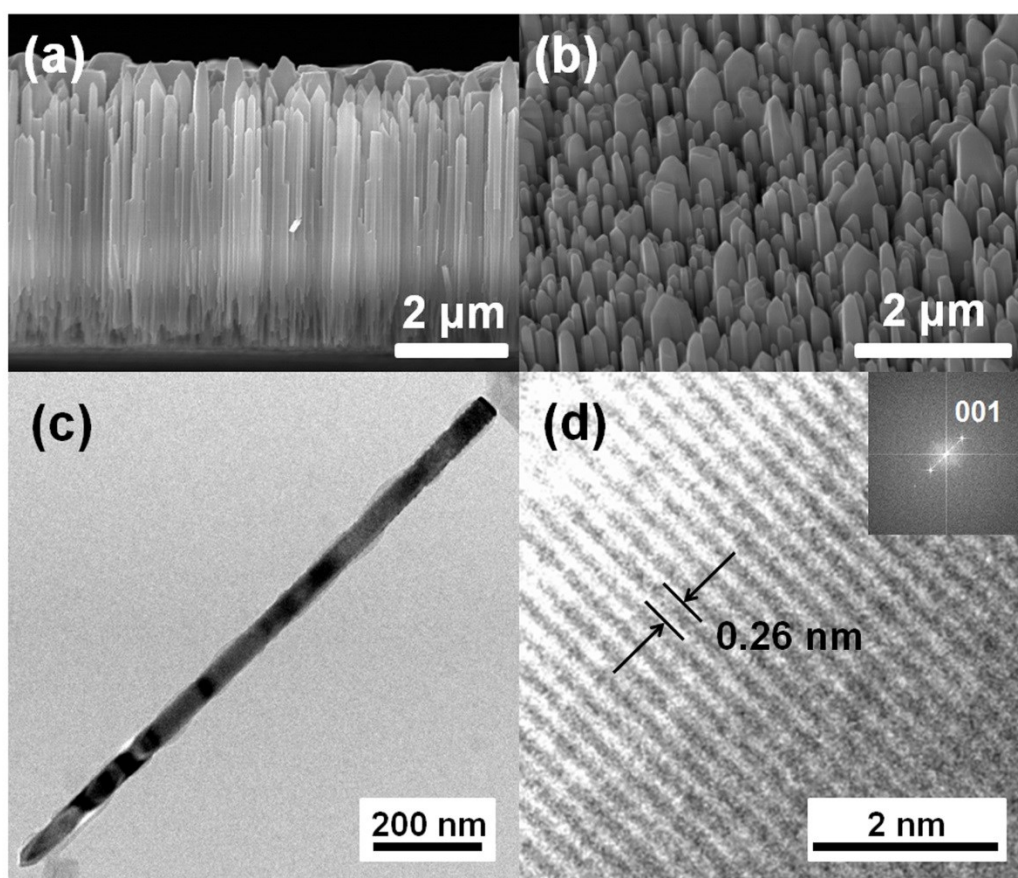


Figure 5.7: FE-SEM images of the ZnO nanorods grown in the solution containing 0.01 M PEI and 0.4 M ammonium hydroxide at 85 °C: (a) cross-sectional view and (b) tilted view. (c) Low-magnification TEM image of the ZnO nanorod. (d) HRTEM image of the ZnO nanorod with its corresponding FFT pattern (inset).

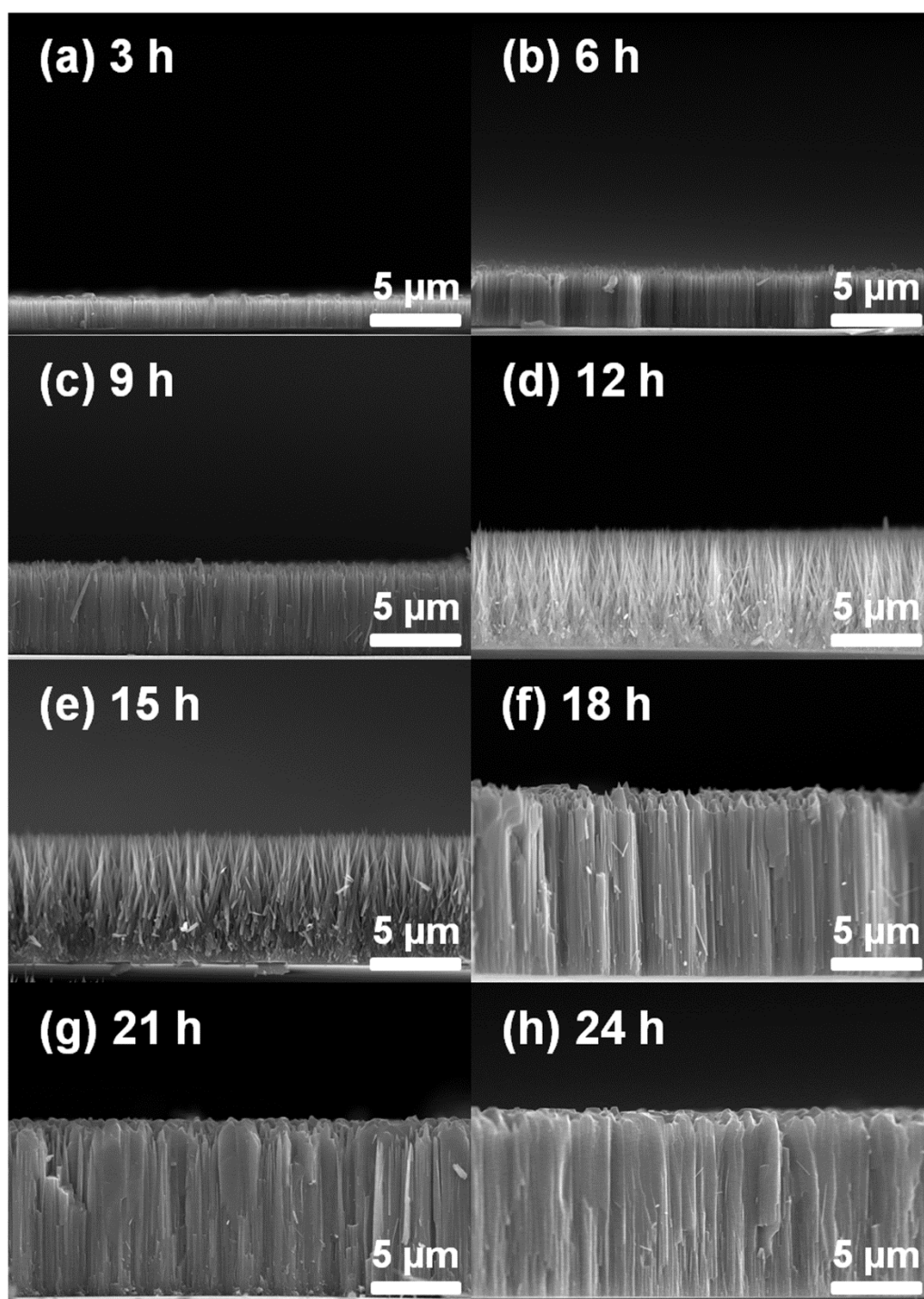


Figure 5.8: Cross-sectional FE-SEM images of the ZnO nanorods grown with different growth times: (a) 3 h, (b) 6 h, (c) 9 h, (d) 12 h, (e) 15 h, (f) 18 h, (g) 21 h, and (h) 24 h.

Effects of Thermal Annealing Processes

To investigate annealing effects on the structural and optical properties of ZnO nanorods grown on mica substrates, a post-growth annealing process was conducted at 500 °C for 30 min. Figure 5.9 shows the XRD patterns of the as-grown and annealed ZnO nanorods. Two ZnO diffraction peaks were observed, at 34.48° and 72.54° respectively, which correspond to the subsequent respective ZnO crystallographic reflections: (002) and (004). Except for the peaks from the mica substrate which are marked with an asterisk in Figure 5.9, all of the peaks in the obtained spectrum were well-indexed to the hexagonal ZnO phase, indicating the single-phase structure of all ZnO nanorods [34]. The intensity of the ZnO(002) diffraction peak was higher compared to that of the standard ZnO diffraction pattern, which indicates a preferential growth direction along the *c*-axis.

The optical properties of the ZnO nanorods were investigated using spontaneous Raman scattering. The frequencies of Raman active phonon modes in ZnO are as follows: E_2 (low) = 102 cm^{-1} , E_2 (high) = 437 cm^{-1} , E_1 (TO) = 410 cm^{-1} , E_1 (LO) = 591 cm^{-1} , A_1 (TO) = 379 cm^{-1} , and A_1 (LO) = 577 cm^{-1} [35,36]. Figure 5.10 shows the Raman scattering spectra of the as-grown and annealed ZnO nanorods. A sharp and strong peak at 438.5 cm^{-1} is assigned to the E_2 (high frequency) optical phonon mode of the ZnO, which is a characteristic of the wurtzite hexagonal phase of ZnO [37]. Two weak peaks located at 380.7 cm^{-1} and 577.4 cm^{-1} are assigned to the A_1 (TO) and A_1 (LO) modes, respectively. The very low intensity of the E_1 (LO) mode at 591 cm^{-1} indicates that the ZnO nanorods are of good crystal quality as the E_1 (LO) mode is associated with

structural defects (zinc interstitials or oxygen vacancies) and impurities in the ZnO crystal.

In addition, the annealing effects on transmittance and sheet resistance of ITO/PET and ITO/mica substrates were investigated to compare the characteristics of the ITO electrode on the two different substrates treated by the different process temperature, which also greatly affected device performances. Figure 5.11 shows the optical transmittance spectra and top-view photographs of PET (black), mica (orange), ITO/PET (red), ITO/mica (green), and annealed ITO/mica (blue). The transmittance spectrum of mica is similar to that of the PET with the sharp oscillatory features of mica falling in the range of 700–1100 nm; these Fabry-Perot interference effects were identified from internal reflections in the atomically layered structures of the mica [38]. The growth of ITO thin films resulted in a subsequent and significant decrease in transmittance in both PET and mica substrates. However, the transmittance of ITO/mica substrates did realign with its original values after an annealing process that peaked at 500 °C for 30 min, while the thermal annealing process could not be conducted on the ITO/PET configuration. The sheet resistance of the ITO/mica substrates also decreased by 80% after the annealing process (Figure 5.12) due to the increased grain size and carrier concentration [13,14]. The transmittance at 550 nm and sheet resistance of the ITO/PET and ITO/mica substrates are summarized in Table 5.2.

Furthermore, a much greater coverage and much improved adhesion properties of ZnO nanorods on the mica substrate were achieved (Figure 5.13). In the observations of the non-growth regions of the ZnO nanorods on PET, most ZnO nanorods peeled off

from the PET substrate after a bending of 1000 cycles with a bending radius of 5 mm. However, under these conditions ZnO nanorods on the mica neither peeled off nor became brittle. This discrepancy is because the temperature of the spin-coating process for the ZnO seed layers on the mica was high enough to evaporate organic residues and crystallize the ZnO seed layers, while the process temperature for the ZnO seed layers on the PET was limited to 100 °C to prevent heat damage and distortion from the process. It was also observed that a use of mica substrates narrowed the full width at half maximum (FWHM) of the ZnO (002) diffraction peak compared to PET substrates, which indicated that the ZnO nanorods grown on a mica substrate exhibited a better crystal quality (Figure 5.14). The comparison of the thermal treatment processes for PET and mica substrates is summarized in Table 5.3.

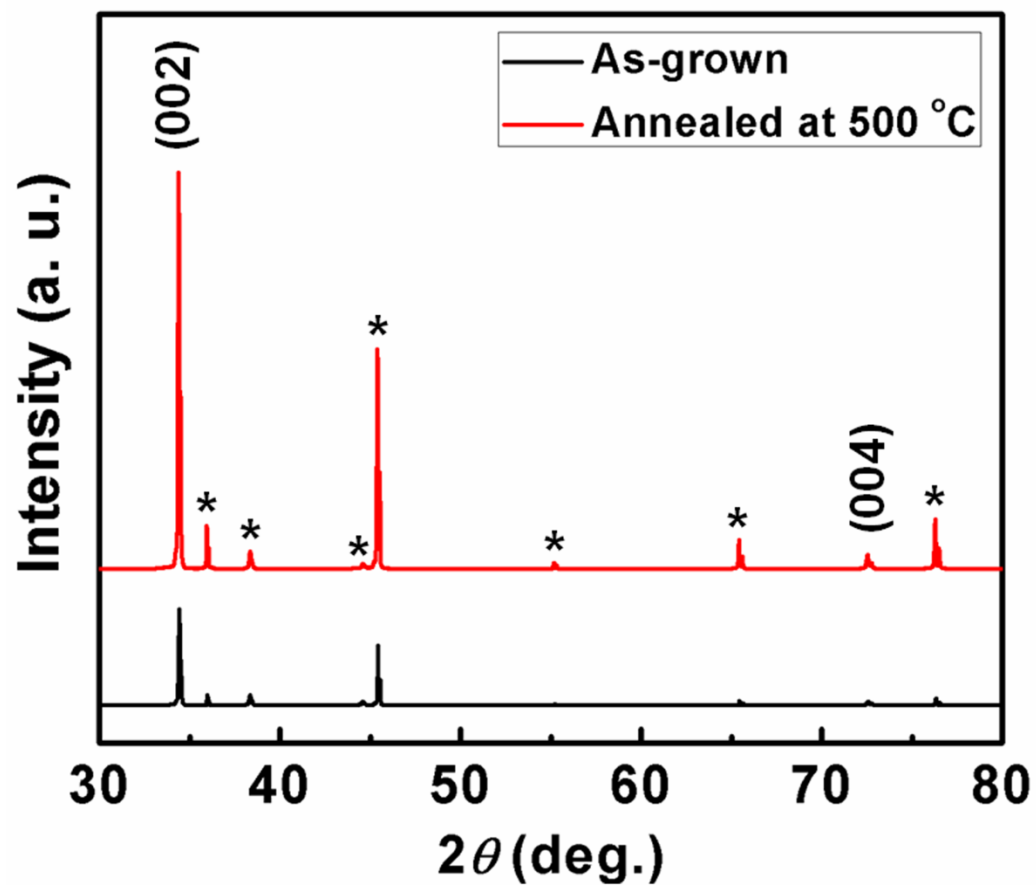


Figure 5.9: XRD patterns of the as-grown and annealed ZnO nanorods. The peaks denoted with an asterisk are attributed to the mica.

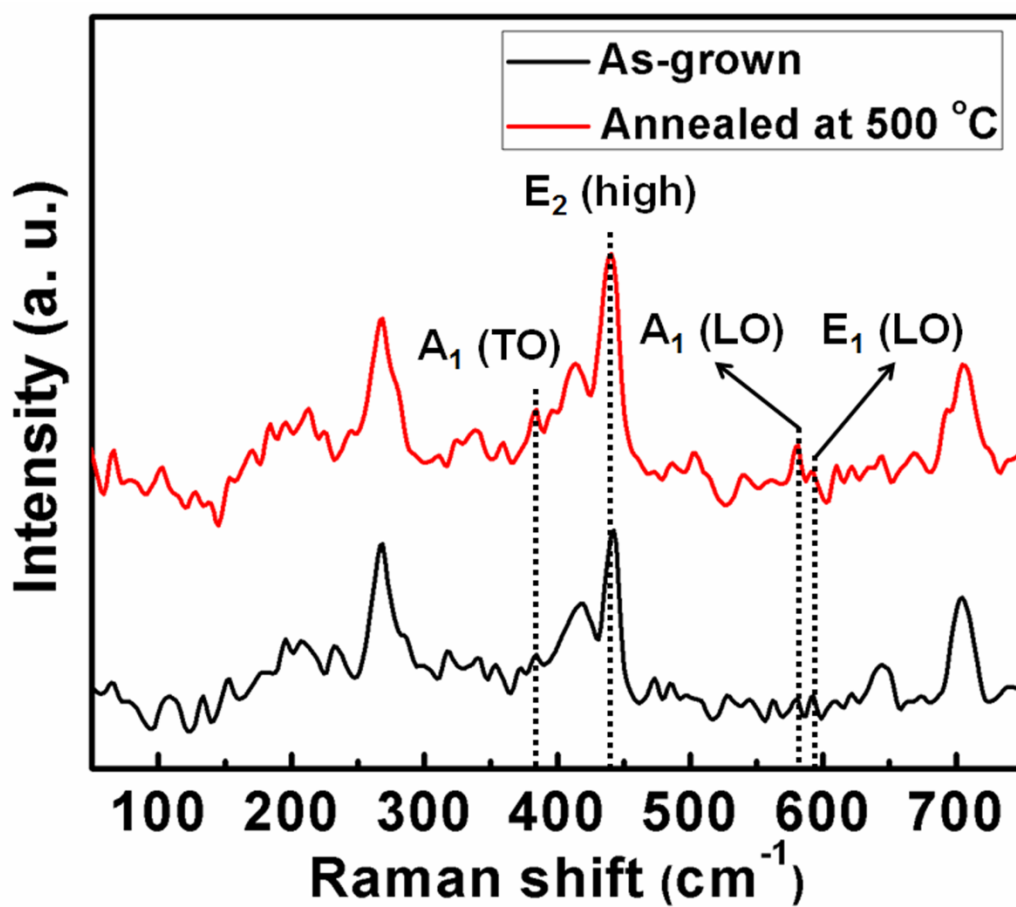


Figure 5.10: Raman scattering spectra of the as-grown and annealed ZnO nanorods.

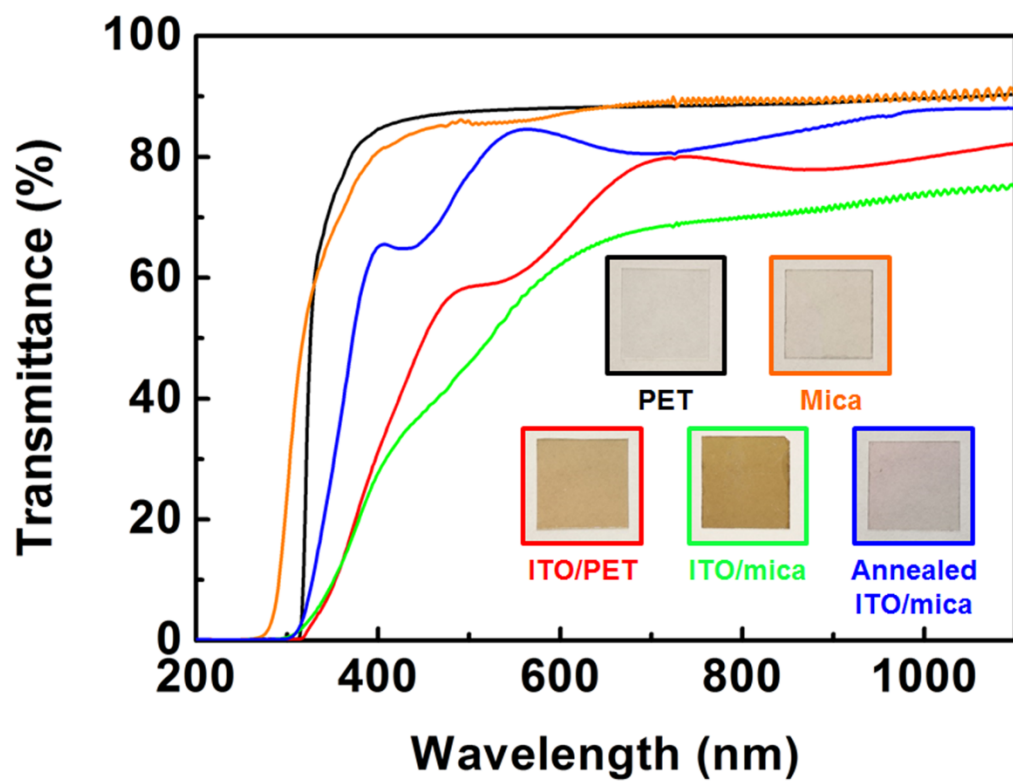


Figure 5.11: Transmittance spectra and top view photographs of PET (black), mica (orange), ITO/PET (red), ITO/mica (green), and annealed ITO/mica (blue).

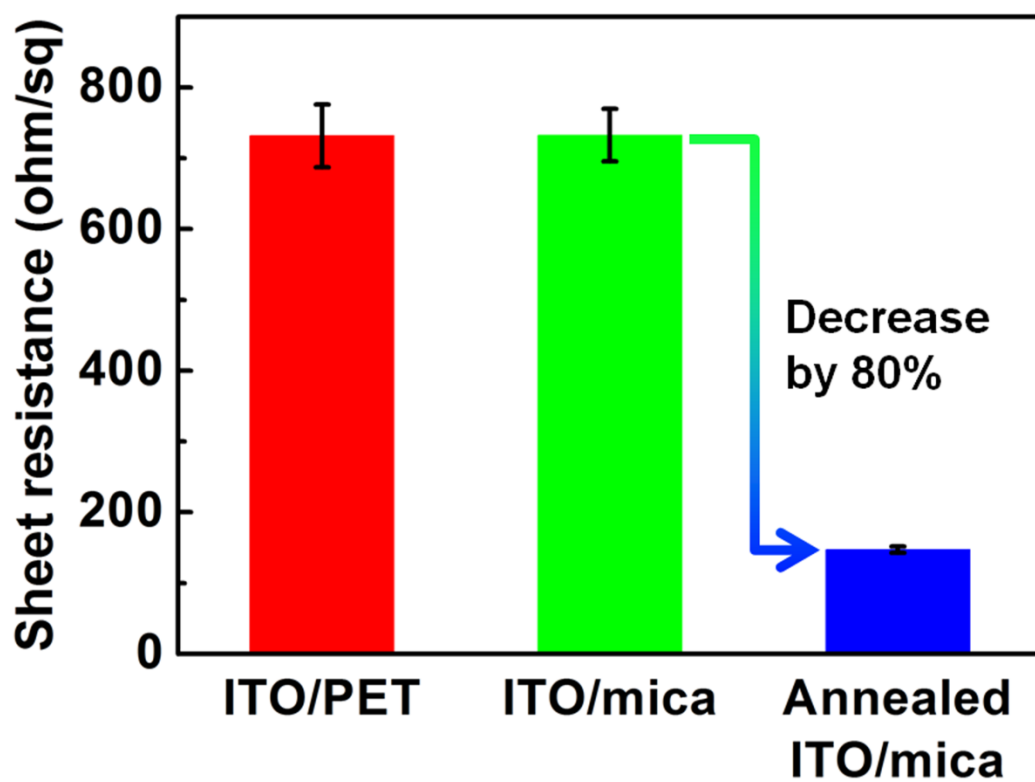


Figure 5.12: Sheet resistance of the ITO/PET (red), ITO/mica (green), and annealed ITO/mica (blue).

Table 5.2: Comparison of transmittance and sheet resistance of the ITO/PET and ITO/mica substrates.

	Transmittance at 550 nm (%)	Sheet resistance (ohm/sq)
PET	87.9	N/A
Mica	86.0	N/A
ITO/PET	60.3	731.6±44.5
ITO/mica	55.3	732.4±37.0
Annealed ITO/mica	84.3	147.1±4.4

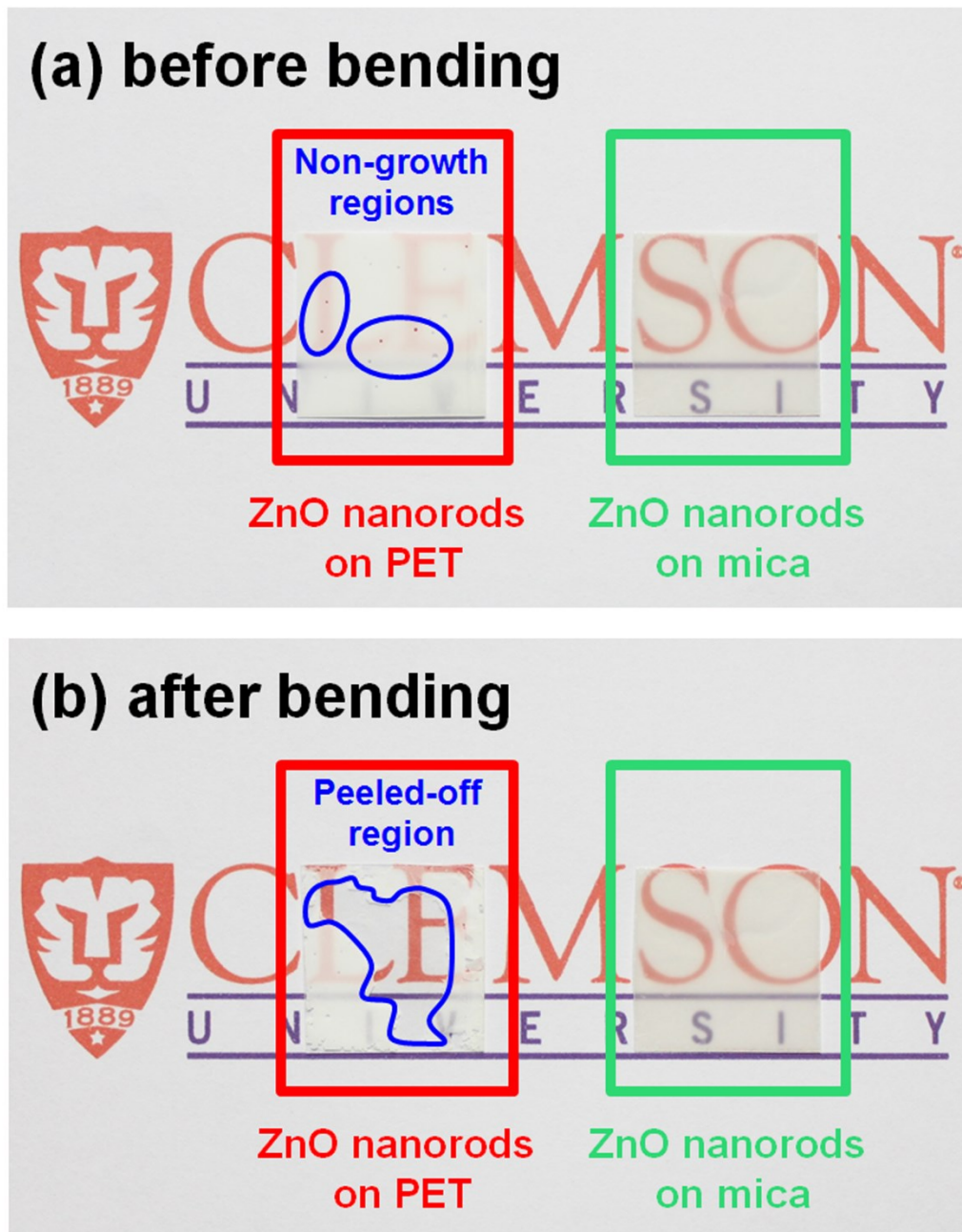


Figure 5.13: Photographs of ZnO nanorods grown on PET and mica substrates: (a) before a bending and (b) after a bending of 1000 cycles with a bending radius of 5 mm.

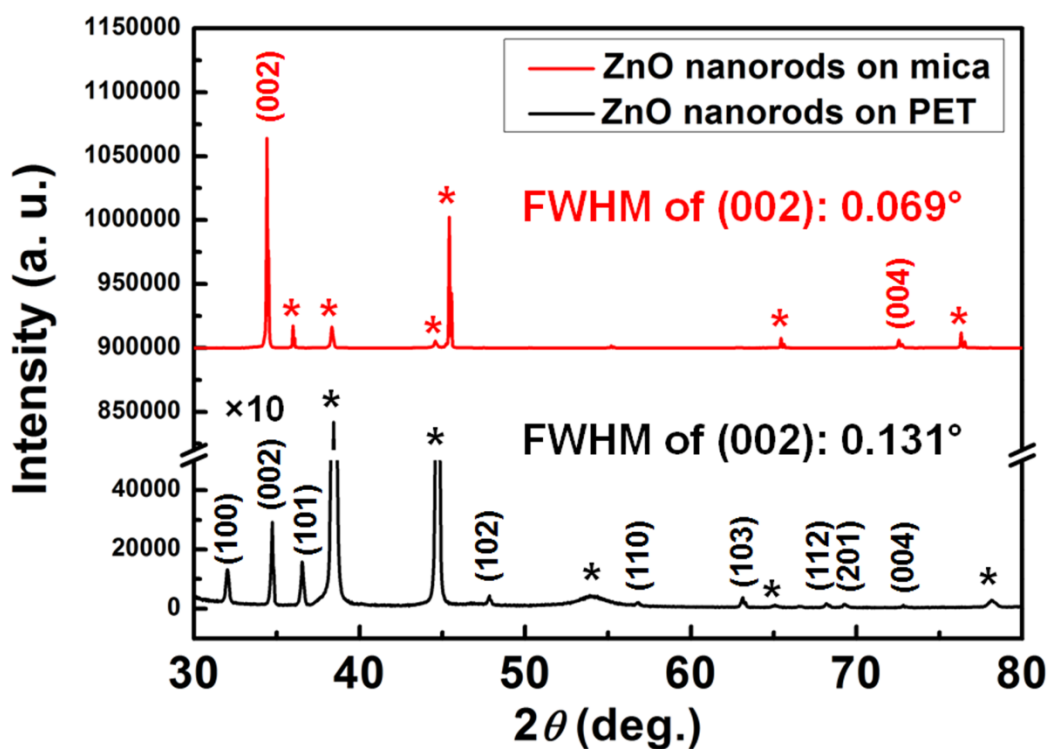


Figure 5.14: XRD patterns of the ZnO nanorods grown on PET and mica substrates. The peaks denoted with an asterisk are attributed to the mica and PET substrates. The signals from the ZnO nanorods grown on PET were multiplied by 10 times of their original values.

Table 5.3: Comparison of the thermal treatment processes for PET and mica substrates.

	Pre-heating temperature for the ZnO seed layers (°C)	Post-heating temperature for the ZnO seed layers (°C)	Post-growth annealing temperature of the ZnO nanorods (°C)
PET	100	-	-
Mica	350	500	500

ZnO Nanorod-Based Dye-Sensitized Solar Cells

Figure 5.15 shows photocurrent density-voltage characteristics of the DSSCs using different growth and annealing schemes: sample A (9 h-growth), sample B (18 h-growth), sample C (9 h-growth and post-growth annealing), and sample D (18 h-growth and post-growth annealing). Longer growth time and an annealing process induced an increase in both the open circuit voltage (V_{oc}) and short circuit current density (J_{sc}). As a result, the efficiency was increased by 42% with an increase in growth time from 9 to 18 h, while the efficiency increased by 53% after a post-growth annealing process for the 9 h-growth samples. Finally, the DSSCs based on the ZnO nanorods (18h-growth and post-growth annealing) exhibited an efficiency of 0.69% with J_{sc} (3.95 mA/cm²) and V_{oc} (0.65 V).

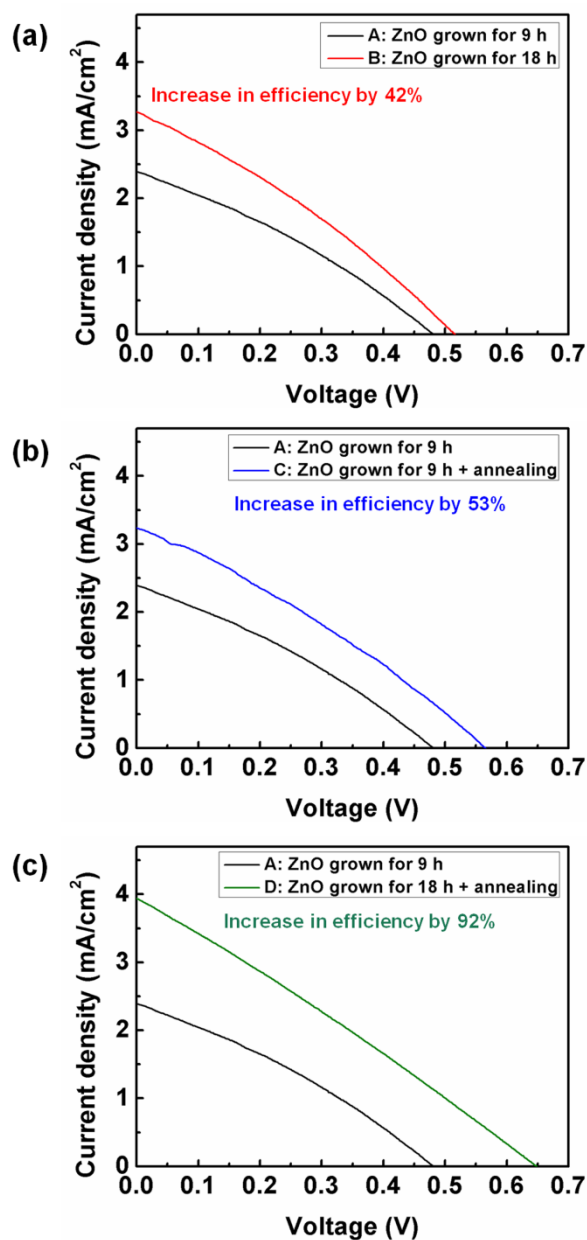


Figure 5.15: Photocurrent density-voltage characteristics of DSSCs with photoanodes made from ZnO nanorods grown on mica under AM 1.5 illumination: (a) sample A (9 h-growth) vs. sample B (18 h-growth), (b) sample A (9 h-growth) vs. sample C (9 h-growth and post-growth annealing) and (c) sample A (9 h-growth) vs. sample D (18 h-growth and post-growth annealing).

ZnO Nanorod-Based Piezoelectric Nanogenerators

The annealing effects on the NG's performance were investigated by preparing two types of NG devices: one fabricated by using as-grown ZnO nanorods and the other by using post-growth annealed ZnO nanorods. As shown in Figure 5.16a and b, the output voltage and output current density for the as-grown ZnO nanorod-based NG were approximately 0.5 V and 25 nA/cm², respectively. When the post-growth annealed ZnO nanorods were used, the output voltage was approximately 1.5 V, with an output current density approaching 80 nA/cm². Both the output voltage and output current density when the post-growth annealed ZnO nanorods were used were approximately three times higher than the output voltage and output current density obtained from the as-grown ZnO nanorods. In other words, this post-growth annealing process of the ZnO nanorods improves the crystal quality by reducing oxygen-vacancy-related defects, which consequently leads to an increase of piezoelectric potential in the ZnO nanorods under the same external conditions. Since the output of the piezoelectric NG is proportional to the piezoelectric potential created in piezoelectric nanorods, the output performance of the post-growth annealed ZnO nanorod-based NG is increased [39–41].

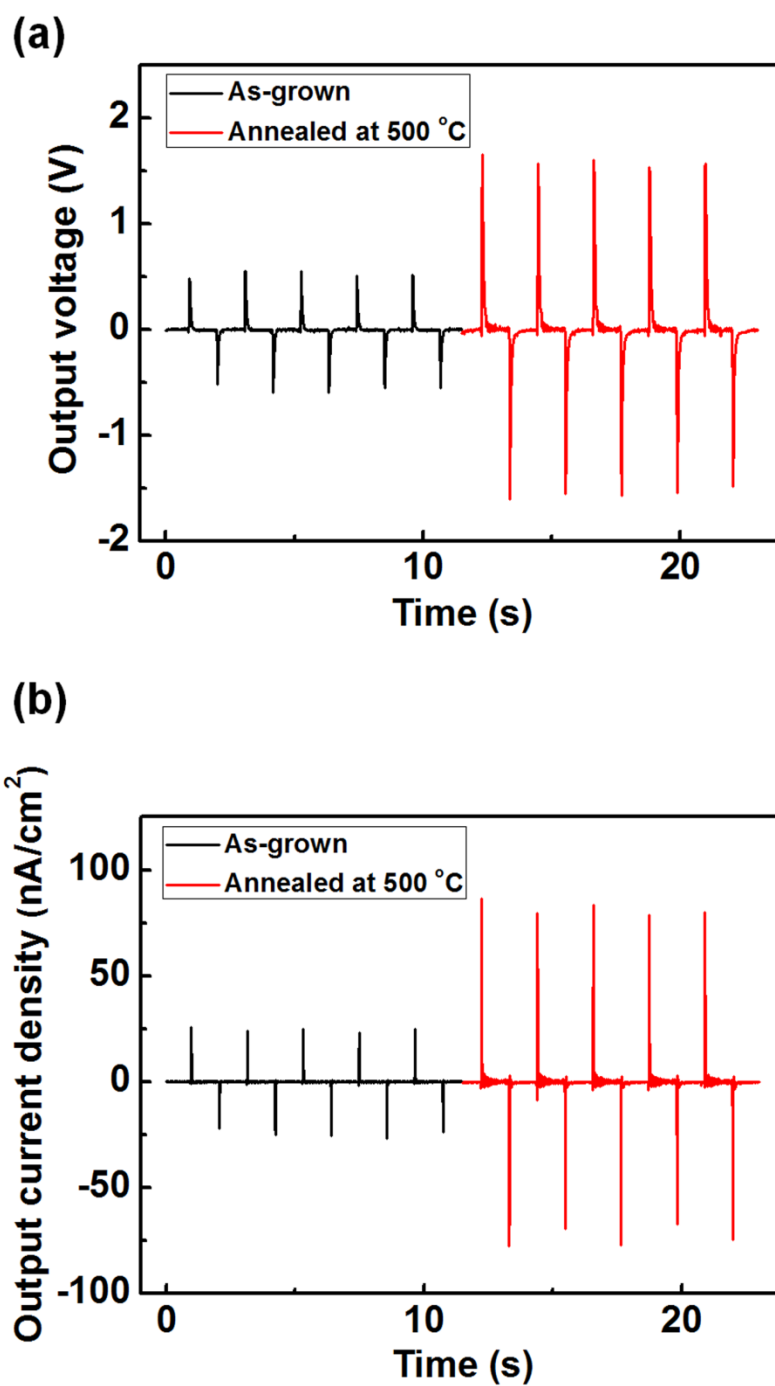


Figure 5.16: Measured output performance of the NG based on as-grown ZnO nanorods (black) and post-growth annealed ZnO nanorods (red): (a) output voltage and (b) output current density.

Conclusions

Mica substrates were first used for the ZnO nanorod-based DSSCs and NGs because of their high flexibility and transparency. Through the coupled use of PEI and ammonium hydroxide, vertically well-aligned ZnO nanorods were successfully grown on mica substrates under 0.01 M PEI and 0.4 M ammonium hydroxide at 85 °C for 9 h. The XRD and Raman scattering measurements indicated that the ZnO nanorods exhibited a good crystal quality with a hexagonal wurtzite structure. The adoption of mica as a substrate material permitted the use of high temperature annealing processes to significantly improve adhesion of ZnO nanorods/ZnO seed layers/ITO/mica as well as transmittance and conductance of ITO/mica. Longer growth times and a post-growth annealing process of ZnO nanorods largely improved the performance of solar cells. Furthermore, the post-growth annealing process of ZnO nanorods led to an increase of the output performance of the NG. In this study, the author simultaneously presented the potential for flexible and transparent hybrid systems (solar cells/displays/batteries), including medical devices that could serve as the mechanism with which to develop the next generation of mobile technologies.

References

- [1] K. Nomura, H. Ohta, A. Takagi, T. Kamiya, M. Hirano, and H. Hosono, Room-temperature fabrication of transparent flexible thin-film transistors using amorphous oxide semiconductors, *Nature*, **432**, 488–492, 2004.
- [2] D. Zhang, K. Ryu, X. Liu, E. Polikarpov, J. Ly, M.E. Thompson, and C. Zhou, Transparent, conductive, and flexible carbon nanotube films and their application in organic light-emitting diodes, *Nano Lett.*, **6**, 1880–1886, 2006.
- [3] D. Zhang, T. Yoshida, T. Oekermann, K. Furuta, and H. Minoura, Room-temperature synthesis of porous nanoparticulate TiO₂ films for flexible dye-sensitized solar cells, *Adv. Funct. Mater.*, **16**, 1228–1234, 2006.
- [4] L. Yuan, X.-H. Lu, X. Xiao, T. Zhai, J. Dai, F. Zhang, B. Hu, X. Wang, L. Gong, J. Chen, C. Hu, Y. Tong, J. Zhou, and Z.L. Wang, Flexible solid-state supercapacitors based on carbon nanoparticles/MnO₂ nanorods hybrid structure, *ACS Nano*, **6**, 656–661, 2011.
- [5] Y. Yang, S. Jeong, L. Hu, H. Wu, S.W. Lee, and Y. Cui, Transparent lithium-ion batteries, *Proc. Natl. Acad. Sci. USA*, **108**, 13013–13018, 2011.
- [6] X. Luan, D. Guan, and Y. Wang, Facile synthesis and morphology control of bamboo-type TiO₂ nanotube arrays for high-efficiency dye-sensitized solar cells, *J. Phys. Chem. C*, **116**, 14257–14263, 2012.

- [7] J.Y. Kim, D. Lee, H.J. Kim, I. Lim, W.I. Lee, and D.J. Jang, Annealing-free preparation of anatase TiO₂ nanopopcorns on Ti foil *via* a hydrothermal process and their photocatalytic and photovoltaic applications, *J. Mater. Chem. A*, **1**, 5982–5988, 2013.
- [8] N.Q. Fu, Y.Y. Fang, Y.D. Duan, X.W. Zhou, X.R. Xiao, and Y. Lin, High-performance plastic platinized counter electrode *via* photoplatinization technique for flexible dye-sensitized solar cells, *ACS Nano*, **6**, 9596–9605, 2012.
- [9] H. Li, Q. Zhao, W. Wang, H. Dong, D. Xu, G. Zou, H. Duan, and D. Yu, Novel planar-structure electrochemical devices for highly flexible semitransparent power generation/storage sources, *Nano Lett.*, **13**, 1271–1277, 2013.
- [10] H. Zhu, Z. Xiao, D. Liu, Y. Li, N.J. Weadock, Z. Fang, J. Huang, and L. Hu, Biodegradable transparent substrates for flexible organic-light-emitting diodes, *Energy Environ. Sci.*, **6**, 2105–2111, 2013.
- [11] S. Ito, N.L.C. Ha, G. Rothenberger, P. Liska, P. Comte, S.M. Zakeeruddin, P. Pechy, M.K. Nazeeruddin, and M. Grätzel, High-efficiency (7.2%) flexible dye-sensitized solar cells with Ti-metal substrate for nanocrystalline-TiO₂ photoanode, *Chem. Commun.*, 4004–4006, 2006.
- [12] S. Lee, J.H. Noh, H.S. Han, D.K. Yim, D.H. Kim, J.K. Lee, J.Y. Kim, H.S. Jung, and K.S. Hong, Nb-doped TiO₂: A new compact layer material for TiO₂ dye-sensitized solar cells, *J. Phys. Chem. C*, **113**, 6878–6882, 2009.

- [13] M. Himmerlich, M. Koufaki, G. Ecke, C. Mauder, V. Cimalla, J.A. Schaefer, A. Kondilis, N.T. Pelekanos, M. Modreanu, S. Krischok, and E. Aperathitis, Effect of annealing on the properties of indium-tin-oxynitride films as ohmic contacts for GaN-based optoelectronic devices, *ACS Appl. Mater. Interfaces*, **1**, 1451–1456, 2009.
- [14] P. Vacca, M. Petrosino, A. Guerra, R. Chierchia, C. Minarini, D.D. Sala, and A. Rubino, The relation between the electrical, chemical, and morphological properties of indium-tin oxide layers and double-layer light-emitting diode performance, *J. Phys. Chem. C*, **111**, 17404–17408, 2007.
- [15] T.M. Hammad, Effect of annealing on electrical, structural, and optical properties of sol-gel ITO thin films, *Phys. Status Solidi A*, **206**, 2128–2132, 2009.
- [16] S. Shen, J. Jiang, P. Guo, C.X. Kronawitter, S.S. Mao, and L. Guo, Effect of Cr doping on the photoelectrochemical performance of hematite nanorod photoanodes, *Nano Energy*, **1**, 732–741, 2012.
- [17] Y. Hu, L. Lin, Y. Zhang, and Z.L. Wang, Replacing a battery by a nanogenerator with 20 V output, *Adv. Mater.*, **24**, 110–114, 2012.
- [18] H. Tan, R. Santbergen, A.H.M. Smets, and M. Zeman, Plasmonic light trapping in thin-film silicon solar cells with improved self-assembled silver nanoparticles, *Nano Lett.*, **12**, 4070–4076, 2012.
- [19] F. Xu and L. Sun, Solution-derived ZnO nanostructures for photoanodes of dye-sensitized solar cells, *Energy Environ. Sci.*, **4**, 818–841, 2011.

- [20] F.N. Ishikawa, H.-K. Chang, K. Ryu, P.-C. Chen, A. Badmaev, L.G.D. Arco, G. Shen, and C. Zhou, Transparent electronics based on transfer printed aligned carbon nanotubes on rigid and flexible substrates, *ACS Nano*, **3**, 73–79, 2009.
- [21] J.B. In, D. Lee, F. Fornasiero, A. Noy, and C.P. Grigoropoulos, Laser-assisted simultaneous transfer and patterning of vertically aligned carbon nanotube arrays on polymer substrates for flexible devices, *ACS Nano*, **6**, 7858–7866, 2012.
- [22] S. Ozder, O. Koysal, S.E. San, and F.N. Ecevit, Determination of the refractive index dispersion of thick films by continuous wavelet transform, *Thin Solid Films*, **458**, 257–262, 2004.
- [23] M. Law, L. Greene, J.C. Johnson, R. Saykally, and P. Yang, Nanowire dye-sensitized solar cells, *Nat. Mater.*, **4**, 455–459, 2005.
- [24] C. Xu, P. Shin, L. Cao, and D. Gao, Preferential growth of long ZnO nanowire array and its application in dye-sensitized solar cells, *J. Phys. Chem. C*, **114**, 125–129, 2010.
- [25] Y. Zhou, W. Wu, G. Hu, H. Wu, and S. Cui, Hydrothermal synthesis of ZnO nanorod arrays with the addition of polyethyleneimine, *Mater. Res. Bull.*, **43**, 2113–2118, 2008.
- [26] W. Wu, G. Hu, S. Cui, Y. Zhou, and H. Wu, Epitaxy of vertical ZnO nanorod arrays on highly (001)-oriented ZnO seed monolayer by a hydrothermal route, *Cryst. Growth Des.*, **8**, 4014–4020, 2008.

- [27] J.H. Tian, J. Hu, S.S. Li, F. Zhang, J. Liu, J. Shi, X. Li, Z.Q. Tian, and Y. Chen, Improved seedless hydrothermal synthesis of dense and ultralong ZnO nanowires, *Nanotechnology*, **22**, 245601, 2011.
- [28] H.S. Choi, M. Vaseem, S.G. Kim, Y.H. Im, and Y.B. Hahn, Growth of high aspect ratio ZnO nanorods by solution process: Effect of polyethyleneimine, *J. Solid State Chem.*, **189**, 25–31, 2012.
- [29] J.W. Mullin, in *Crystal Growth*, B.R. Pamplin Ed., Pergamon Press, New York, 1974.
- [30] L.E. Greene, B.D. Yuhas, M. Law, D. Zitoun, and P. Yang, Solution-grown zinc oxide nanowires, *Inorg. Chem.*, **45**, 7535–7543, 2006.
- [31] J.M. Jang, S.D. Kim, H.M. Choi, J.Y. Kim, and W.G. Jung, Morphology change of self-assembled ZnO 3D nanostructures with different pH in the simple hydrothermal process, *Mater. Chem. Phys.*, **113**, 389–394, 2009.
- [32] Y. Tak and K. Yong, Controlled growth of well-aligned ZnO nanorod array using a novel solution method, *J. Phys. Chem. B*, **109**, 19263–19269, 2005.
- [33] J. Qiu, X. Li, F. Zhuge, X. Gan, X. Gao, W. He, S.J. Park, H.K. Kim, and Y.H. Hwang, Solution-derived 40 μm vertically aligned ZnO nanowire arrays as photoelectrodes in dye-sensitized solar cells, *Nanotechnology*, **21**, 195602, 2010.
- [34] L.-Y. Chen, Y.-T. Yin, C.-H. Chen, and J.-W. Chiou, Influence of polyethyleneimine and ammonium on the growth of ZnO nanowires by hydrothermal method, *J. Phys. Chem. C*, **115**, 20913–20919, 2011.

- [35] J.M. Calleja and M. Cardona, Resonant Raman scattering in ZnO, *Phys. Rev. B*, **16**, 3753–3761, 1977.
- [36] N. Ashkenov, B.N. Mbenkum, C. Bundesmann, V. Riede, M. Lorenz, D. Spemann, E.M. Kaidashev, A. Kasic, M. Schubert, M. Grundmann, G. Wagner, H. Neumann, V. Darakchieva, H. Arwin, and B. Monemar, Infrared dielectric functions and phonon modes of high-quality ZnO films, *J. Appl. Phys.*, **93**, 126–133, 2003.
- [37] Y.J. Xing, Z.H. Xi, Z.Q. Xue, X.D. Zhang, J.H. Song, R.M. Wang, J. Xu, Y. Song, S.L. Zhang, and D.P. Yu, Optical properties of the ZnO nanotubes synthesized *via* vapor phase growth, *Appl. Phys. Lett.*, **83**, 1689–1691, 2003.
- [38] H. Peng, W. Dang, J. Cao, Y. Chen, D. Wu, W. Zheng, H. Li, Z.X. Shen, and Z. Liu, Topological insulator nanostructures for near-infrared transparent flexible electrodes, *Nat. Chem.*, **4**, 281–286, 2012.
- [39] Z.L. Wang and J.H. Song, Piezoelectric nanogenerators based on zinc oxide nanowire arrays, *Science*, **312**, 242–246, 2006.
- [40] S. Lee, J.-I. Hong, C. Xu, M. Lee, D. Kim, L. Lin, W. Hwang, and Z.L. Wang, Toward robust nanogenerators using aluminum substrate, *Adv. Mater.*, **24**, 4398–4402, 2012.
- [41] S. Lee, S.-H. Bae, L. Lin, Y. Yang, C. Park, S.-W. Kim, S.N. Cha, H. Kim, Y.J. Park, and Z.L. Wang, Super-flexible nanogenerator for energy harvesting from gentle wind and as an active deformation sensor, *Adv. Funct. Mater.*, **23**, 2445–2449, 2013.

CHAPTER SIX

CONCLUSIONS

Research Summary

Doping behavior of Ga in ZnO nanorods is studied in Chapter III. A sol-gel spin-coating technique and a hydrothermal process were used to grow the ZnO nanorods for transparent electrode applications. ZnO nanorods were doped with different Ga concentrations varying from 0.5 to 3.0 at.% and compared with an undoped sample. The incorporation of Ga into ZnO crystals resulted in remarkable changes in the structural and interfacial properties of ZnO nanorods including morphology, size, density, alignment along the *c*-axis, and wettability. Results also showed improvements in the electrical and optical properties of Ga-doped ZnO nanorods, such as lower resistivity and an increase in transparency.

Reported in Chapter IV is the low temperature growth of multiple-stack high-density ZnO nanoflower/nanorod structures on plastic substrates that were derived from the surface modification of ZnO seed layers using an atmospheric pressure plasma jet (APPJ) treatment. The plasma treatment could provide several advantages to the growth of multiple stacked ZnO nanoflower/nanorod structures: (i) the surface wettability of the seed layers changes from hydrophobic to hydrophilic, resulting in higher surface energies for the growth of high-density ZnO nanoflowers, (ii) the nucleation sites increase due to the increased surface roughness caused by the plasma etching, and (iii) there is no thermal damage to the plastic substrate from the plasma treatment due to its low temperature weakly-ionized discharge. It was also confirmed that multiple-stacks of ZnO

nanoflowers were obtained without degradation of the crystal quality or modification to the crystal shape or phase. The ZnO nanoflower/nanorod structures obtained from the plasma treatment grew by lengths of up to 4 μm , due to an increased surface roughness (10%) and surface energy (5.5 times) of the seed layers. As shown, the APPJ is a very preferable method to obtain high-density ZnO nanostructures on plastic substrates below 150 $^{\circ}\text{C}$, which is critical for flexible electronics.

High temperature processed ZnO nanorods on flexible and transparent mica substrates are reported in Chapter V. The coupled use of polyethylenimine and ammonium hydroxide provided a direct method for growing vertically well-aligned ZnO nanorods with a high aspect ratio. Using mica as a substrate material enabled thermal annealing processes at higher temperatures that precluded the use of plastic substrates, which improved the structural and optical properties of ZnO nanorods with uniform surface coverage and excellent adhesion, increased transmittance of indium tin oxide (ITO)/mica (52%), and decreased sheet resistance of ITO/mica (80%). ZnO nanorod-based dye-sensitized solar cells (DSSCs) and piezoelectric nanogenerators (NGs) were fabricated, and annealing effects on device performance were investigated. Specifically, thermal treatment at 500 $^{\circ}\text{C}$ for 30 min increased the energy conversion efficiencies of DSSCs by 53%. Furthermore, a three-fold increase in the NG's output voltage and output current density was observed through this thermal annealing process.

Future Work

Based on the results obtained from the experiments presented in this dissertation, there is some room for improvement in this work. First, the Ga-doped ZnO nanorods in

this work should exhibit higher optical transmittance and electrical conductance to be used for transparent electrodes. It is expected that the coupled use of polyethylenimine and ammonium hydroxide in the growth of Ga-doped ZnO nanorods would promote the growth direction along the *c*-axis, enhancing optical transmittance. Post-growth annealing could also significantly improve crystal quality and electrical characteristics of Ga-doped ZnO nanorods based on the fact that thermal annealing generally results in an enlargement of grain size and an activation of Ga dopants. It is necessary to determine the optimal thermal annealing temperature and time for the Ga-doped ZnO nanorods with favorable optical and electrical characteristics for transparent electrodes.

Nanoflower is a very desirable nanostructure in a variety of applications such as solar cells, sensors, and photodetectors due to its high surface area to volume ratio. Multiple stacked ZnO nanoflowers were successfully grown on plastic using the APPJ treatment of the ZnO seed layers. However, the processing temperature was limited up to 150 °C because of the use of polyethylene naphthalate substrates. If multiple stacked ZnO nanoflowers/nanorods structure derived from APPJ is grown on mica substrates, we can conduct thermal annealing treatments at higher temperature, which would enable high-performance flexible and transparent electronic devices.